Controlling Shrinkage and Crack Widths in RC Structures Using Sustainable Construction Materials

A thesis submitted for the degree of
Doctor of Philosophy

By
Zahran Saif Al-Kamyani
(BSc, MSc)

Department of Civil and Structural Engineering
The University of Sheffield

Sheffield
June 2018

To my wife who dissipated my stresses,

To my son who healed my cracks,

To my parents who reinforced my concrete,

To my siblings who enriched my sustainable resources.

Abstract

Durability and sustainability of reinforced concrete (RC) infrastructure depends on the materials and techniques used and the extent to which the inevitable cracking is controlled. Serviceability limit state design (SLS) is currently being used to control crack widths to achieve the desired life span of the structure. Crack control is achieved by using relatively large amounts of steel reinforcement near the surface. Alternative cementitious materials and fibres, from more sustainable sources, can also be used to control crack widths. In large structures, restrained shrinkage can increase tensile strain and amplify crack widths and to address that additional amounts of reinforcement and cover are needed. Recent studies also show that shrinkage is non-uniform through the section, possibly due to uneven aggregate distribution. Thus, the correct determination of strains induced by shrinkage are necessary for the accurate prediction of structural deformations.

The aim of this study is to contribute to the understanding of how shrinkage and fibres impact short- and long-term crack widths determination in RC structures so as to lead to better predictions that can enhance the durability and sustainability of urban infrastructure. Experimental work is used to study: a) the development of non-uniform shrinkage strains in specimens made with different sizes and configurations of reinforcement, as well as the impact of shrinkage and fibres on the development of crack widths and deflections of elements tested in flexure and b) the effect of steel fibre blends in controlling shrinkage cracks in restrained elements, internally or externally, and propagation of crack widths under pure bending tests.

It was found that non-uniform shrinkage strains develop through sections due to non-uniform distribution of aggregates and a model to predict the stiffness centroid of sections and shrinkage induced strains is developed. This is used to modify crack widths predictive equations using an effective strain approach. A refined design equation, based on a modification of the *fib* Model Code 2010, is proposed.

Replacement of ordinary Portland cement (OPC) with 50% granulated ground blast-furnace slag (GGBS) was found to reduce shrinkage on average by about 35%, but the steel fibres do not affect free shrinkage strains. However, fibre blends of manufactured and recycled steel fibres can successfully control cracks in restrained and RC elements. For typical RC elements with about 1% of longitudinal bars, the addition of about 1% of steel fibres can reduce crack widths by more than 30%.

Acknowledgements

I would like to acknowledge my supervisors, Prof. Kypros Pilakoutas and Dr. Maurizio Guadagnini for their support and guidance to accomplish the work presented in this thesis and gained cognition over the past four years.

Great thanks and appreciations to the technicians in concrete and heavy structures laboratories, for their help and understanding, and to all members in Concrete and Earthquake Engineering (CEE) group for their technical and numerical support.

I appreciate the financial support provided by the Omani government "His Majesty Grants", Ministry of Higher Education and the EC collaborative FP7-ENV-2013 project "ANAGENNISI — Innovative Reuse of All Tyre Components in Concrete" under grant number 603722.

Finally, infinite thanks to all members of my family for their encouragement, patience and hope over my entire life.

Table of Content

List of Figures

List of Tables

List of Symbols and Abbreviations

Symbol	**Unit**	**Latin Capital Letters**
A_c	mm^2	Area of concrete
$A_{c,eff}$	mm^2	Effective area of concrete under tension
A_s	mm^2	Area of steel reinforcement
B	-	Bottom of section or amount of binder
Bb	-	Bottom of section at rebar level
C	kg/m^3	Amount of coarse aggregates
CMOD	mm	Crack mouth opening displacement
CR	-	Control room
CS	-	Column section
D	mm	Maximum size of coarse aggregates
DEMEC	-	Demountable mechanical
E_c	MPa	Elastic modulus of concrete
$E_{c,eff}$	MPa	Effective elastic modulus of concrete
E_s	MPa	Elastic modulus of steel
F	kg/m^3	Amount of fine aggregates
FEA	-	Finite element analysis
FRC	-	Fibre reinforced concrete
G_c	mm	Geometrical centroid of plain concrete
G_{eff}	mm	Effective geometrical centroid of plain concrete
G_h	mm	Homogenized geometrical centroid of reinforced concrete
G_s	mm	Geometrical centroid of steel reinforcement
GGBS	-	Granulated ground blast-furnace slag

Symbol	Unit	Latin Capital Letters
I_c	mm^4	Second of area for concrete section
I_g	mm^4	Second of area for gross reinforced concrete section
M_{cr}	kN.m	Moment at cracking load
M_{cs}	kN.m	Shrinkage induced moment
MC	-	*fib* Model Code 2010
MR	-	Mist room
MUSF	-	Manufactured undulated steel fibre
OPC	-	Ordinary Portland cement
R/FRC	-	Reinforced concrete with rebars and fibres
RC	-	Reinforced concrete
RCC	-	Roller-compacted concrete
RF	-	Restrained factor
RS	-	Restrained shrinkage
RTSF	-	Recycled tyre steel fibre
S	mm	Concrete slump or first moment of area of reinforcing bars
S_{max}	mm	Maximum crack spacing
SCC	-	Self-compacted concrete
SFRC	-	Steel fibre reinforced concrete
SHS	-	Square hollow section
SLS	-	Serviceability limit state
T	-	Top of section
Tb	-	Top of section at rebar level
ULS	-	Ultimate limit state

Symbol	Unit	Latin Small Letters
b	mm	Width of concrete section
c	mm	Clear concrete cover
d	mm	Effective concrete depth
e_c	mm	Eccentricity of plain concrete
e_h	mm	Eccentricity of homogenized reinforced concrete
f_{cm}	MPa	Concrete mean compressive strength
f_{ctm}	MPa	Concrete mean tensile strength
f_{LOP}	MPa	Concrete flexural strength at limit of proportionality
f_{Lk}	MPa	Concrete characteristic flexural strength at limit of proportionality
f_{Rj}	MPa	Concrete flexural strength at i^{th} CMOD
f_{Rjk}	MPa	Concrete characteristic flexural strength at i^{th} CMOD
h	mm	Height of concrete section
h_b	mm	Height of concrete beam
h_o	mm	Constant height of concrete section, 100 mm
k	-	Constant factor
k_{cs}	1/km	Shrinkage induced curvature
k_{fl}	-	Coefficient to estimate axial tensile strength from flexural strength
t	day	Time at concerned age
t_o	day	Time at drying commencement
w_{cr}	mm	Crack width
y_i	mm	Distance of i^{th} layer from the beam base
y_{RC}	mm	Distance of geometrical centroid of reinforced concrete from the base
y_{si}	mm	Distance of i^{th} layer of steel reinforcement from the beam base

Symbol	**Unit**	**Greek Small Letters**
α_e	-	Effective modular ratio
α_{fl}	-	Coefficient depends on the characteristic length
β	-	Empirical coefficient to assess tension stiffening
ε_{cm}	-	Mean strain in concrete
ε_{cs}	-	Concrete shrinkage in plain and free element
$\varepsilon_{cs,RC}$	-	Concrete shrinkage in reinforced concrete element
ε_{sm}	-	Mean strain in reinforcement
η_r	-	Coefficient for considering the shrinkage contribution
ρ	kg/m^3	Density of concrete
ρ_s	-	Ratio of steel reinforcement
$\rho_{s,eff}$	-	Effective ratio of steel reinforcement
τ_b	MPa	Mean bond strength between concrete and steel
φ	-	Coefficient of creep
χ	-	Aging factor
ϕ_s	mm	Diameter of reinforcing bars

Chapter 1: Introduction

This chapter presents the motivation behind this work, some literature for a better understanding for the problem, aim and objectives, research methodology and thesis presentation.

1.1 Motivation

Durability of reinforced concrete (RC) infrastructure is an important aspect of urban sustainability. Photos shown in Figure 1.1 (a and b) show deterioration of RC culvert boxes due to poor concrete cover while Figure 1.2 (a and b) shows evidence of corrosion in a water tank retaining structure (about 10 years old) reinforced with epoxy coated bars. Although these structures were built to high standards, deterioration still occurred due to chemical attack and due to passivation of the protective alkaline layer of steel. Both of these mechanisms are accelerated by cracks, which allow the chemicals to reach the reinforcement faster. Cracking of concrete is inevitable and can happen at many different stages during the structure's life. Cracking may take place during the construction period due to plastic shrinkage or as an action of restrained drying shrinkage. It may also take place during the service life of the structure as a result of environmental exposure and stresses from service loading. Excessive cracking can shorten the service life of structures and the use of larger amounts of virgin materials (e.g. larger concrete cover, higher amount of reinforcement) would be required to control cracking, thus increasing cost and environmental impact. To achieve sustainable urban construction there is a need not only to ensure durability but also to minimise the use of virgin materials and construction waste, and if possible utilise waste materials with appropriate properties.

There are many solutions, made from virgin materials, to control shrinkage cracking, corrosion and other types of concrete deteriorations used by the construction industry and at the same time, materials with similar properties are disposed in landfills. Recently, the University of Sheffield led the EU project Anagennisi, which dealt with the recycling of all tyre components in concrete. In terms of steel fibres, there is experimental work done on slabs on grade, sprayed concrete and screeds (Hu, et al., 2018; Bartolac, et al., 2016;

Baricevic, et al., 2017; Pérez, et al., 2017). The results are promising and can offer engineering and environmental solutions for RC construction. Therefore, to control shrinkage cracks and address the issue of urban sustainability at the same time, the recycling of by-products and waste materials are considered in this study. The study will use Ground Granulated Blast-furnace Slag (GGBS) to reduce the amount and rate of shrinkage strain and manufactured and recycled tyre steel fibres (RTSF) to control crack widths.

Figure 1.1 Deterioration of culvert boxes (Bahla/Oman-2014).

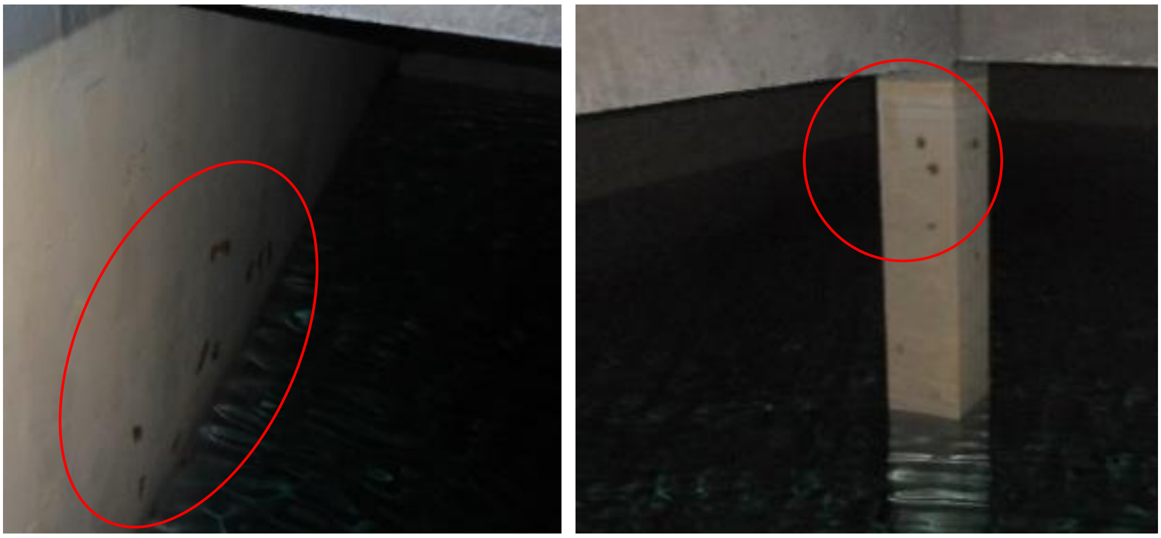

Figure 1.2 Corrosion spots on a water tank retaining structure (Ibri/Oman-2014).

1.2 Background

1.2.1 Shrinkage cracking

Concrete shrinkage is the time-dependent reduction in concrete volume due to the chemical reaction of the cement paste (autogenous shrinkage) and capillary water loss to the environment (drying shrinkage) (Gilbert, 2001). Concrete continues to lose moisture through its exposed surfaces until it reaches hygral equilibrium with the environment (Bazant & Baweja, 2001). Concrete shrinkage can be mitigated by reducing paste/aggregate ratio, minimising C_3S content in cement and supplementary cementitious materials (SCM), by using expansive additives, shrinkage reducing chemical admixtures and internal curing materials (ACI-231R, 2010). As one of the sustainable solutions, GGBS was found to reduce total shrinkage (Jianyong & Yan, 2001; Aly & Sanjayan, 2008; Mitchell & Arya, 2015) as its fineness seems to seal the concrete pores that allow water to escape from the substrate (Castel, et al., 2016). The sustainability benefits of GGBS include: a) increasing the durability of concrete by reducing shrinkage and cracking; b) reducing the CO_2 emission by decreasing the amount of cement in the concrete; c) recycling a waste product.

Shrinkage cracking can be controlled by providing dense skin reinforcement, increasing of concrete strength and/or providing movement joints every few meters (Lin, et al., 2012), but these solutions are not environmentally friendly since they consume additional virgin materials. Furthermore, the use of relatively high amounts of reinforcement can lead to bar congestion and inadequate concrete cover (see Figure 1.3), which may eventually be the cause of cracking and corrosion by themselves.

Reinforcement corrosion can be prevented by using stainless steel, epoxy coated bars, zinc coated bars, migration corrosion inhibitors (MCIs), cathodic protection, etc. On the other hand, the concrete surface can also be protected by coating the surface with epoxy resin, neoprene, etc. However, each one of these solutions has cost and environmental impact implications. Therefore, alternative sustainable solutions are needed.

Figure 1.3 Non-adequate concrete cover in concrete slab (left) and congestion of reinforcement in a junction of a T-wall (right) reinforced with epoxy coated bars (Al-Amerat/Oman-2013).

1.2.2 Cracking reinforcement

In addition to skin reinforcement, randomly distributed steel fibres can help in controlling surface cracking by distributing the strain in the concrete cover and enabling more but smaller cracks (Younis, 2014). In addition, fibres can reduce the stress in the main bars and enable the construction of longer spans (Groli & Caldentey, 2017; Groli, et al., 2014). However, steel fibres are randomly distributed in all directions and are not as effective structurally as continuous bars, thus making them expensive as structural reinforcement for large planar elements. Nonetheless, the combination of bars and fibres could offer an economical solution for surface crack control, in particular for flat elements of bridges or water retaining structures. The use of different types and ratios of steel fibres in crack width control has been studied by several researchers (Tan, et al., 1995; Gribniak, et al., 2012; Vandewalle, 2000; Vasanelli, et al., 2013; Groli & Caldentey, 2017) and is considered by the *fib* Model Code 2010 (fib, 2013) as shown in Equation (1.1).

$$w_d = 2\left(kc + \frac{(f_{ctm} - f_{Ftsm})}{4\tau_b}\frac{\emptyset_s}{\rho_{s,eff}}\right)\left(\varepsilon_{sm} + \eta_r\varepsilon_{cs} - \frac{\beta(f_{ctm} - f_{Ftsm})}{\rho_{s,eff}E_s}\left(1 + \alpha_e\rho_{s,eff}\right)\right) \quad (1.1)$$

where:

w_d is the maximum crack width at the level of reinforcement;

k is an empirical parameter to take the influence of the concrete cover into consideration;

c is the concrete cover;

f_{ctm} is the concrete mean tensile strength;

f_{Ftsm} is the average value of the residual strength of FRC;

τ_{bm} is the mean bond strength between steel and concrete;

$\emptyset_s$ is the steel bar diameter;

$\rho_{s,eff}$ is the effective steel ratio;

ε_{sm} is the mean tensile strain in the reinforcing bars;

η_r is a coefficient for considering the shrinkage contribution;

ε_{cs} is the shrinkage strain;

β is an empirical coefficient of 0.6 for short-term loading and 0.4 for long-term and repeated loading;

α_e is the effective modular ratio;

The addition of fibres to RC is expected to reduce the crack depth and transfer length (l_{cs}) compared to conventional reinforced concrete as shown in Figure 1.4. This is because fibres will reduce the tensile stress on the longitudinal bars at the cracked section through their capabilities of bridging the cracked faces of concrete. Therefore, to maintain equilibrium of forces between the cracked section and the no-slip section, the transfer length is reduced.

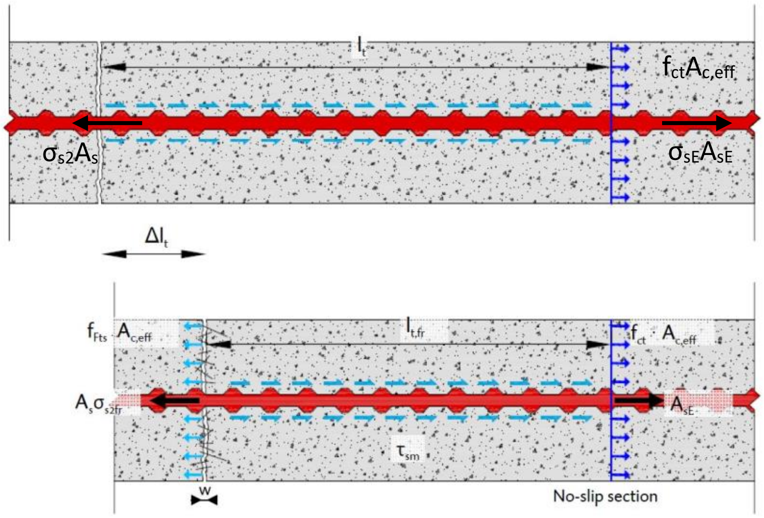

Figure 1.4 Effect of fibres in reducing transfer length, after Groli (2014).

Manufactured fibres have been successfully used along with conventional bars for crack control (Tan, et al., 1995; Gribniak, et al., 2012; Vandewalle, 2000; Vasanelli, et al., 2013; Groli & Caldentey, 2017) and RTSF are expected to perform well as an alternative. Work done over the past two decades has demonstrated that RTSF can be used in various concrete applications including tunnel lining, water retaining walls and slabs-on-grade (Groli & Caldentey, 2017; Groli, et al., 2014). For a given dosage, RTSF perform better than manufactured fibres in preventing micro-crack propagation due to their large number, as they are thinner and shorter, while manufactured steel fibres are better in controlling larger cracks (Younis, 2014; Martinelli, et al., 2015). Recently, some analytical and experimental work has been done on crack width control in RC elements using self-compacted concrete (SCC) and RTSF (Groli, et al., 2014). SCC is not always desired for technical and economic reasons and additional work on conventional concrete is required. In addition, all previous work (Angelakopoulos, et al., 2015; Graeff, 2011; Groli, et al., 2014; Jafarifar, 2012; Younis, 2014; Martinelli, et al., 2015) compared RTSF with different types of manufactured steel fibres. However, the use of a combination of both types of steel fibres by using different fibre blends would exploit the dual benefit of controlling both micro-cracking and macro-cracking and it will be investigated in this research project.

1.2.3 Internal cracking

It is generally assumed that at the no-slip section, i.e. between cracks (see Figure 1.4), the strain in the reinforcement is equal to the strain in the concrete. However, this fails to explain experimental evidence that shows that the tensile strain in the reinforcement can be much higher than the tensile cracking strain of the concrete (Goto, 1971; Beeby & Scott, 2005). This phenomenon may be attributed to the presence of numerous internal cracks that accommodate the difference in strain between reinforcement and cracked concrete along the length of the bar between primary cracks (Beeby & Scott, 2005). Figure 1.5 shows a schematic representation of a cracked section in tension by Goto (1971) and the mechanism of resistance provided by the ribs through compression struts, which develop due to perpendicular tensile stress that result in internal tensile cracking and local slip behind the ribs (Goto, 1971). With increasing strain, these cracks propagate from the ribs toward the outer concrete surface, but not all internal cracks appear on the surface. Consequently, wider cracks develop at the outer surface of the concrete compared to the bar surface (Micallef, 2015; Groli, 2014; Beeby & Scott, 2005; Goto, 1971). However, in elements subjected to bending, it is expected that the crack width varies linearly from the bottom tensile fibre to the neutral axis (NA) in accordance with plane sections remain plane assumption. But, due to presence of internal cracks, major cracks tend to close slightly at the level of reinforcement, as shown in Figure 1.6 (Deng & Matsumoto, 2017; Nazmul & Matsumoto, 2008b; Nazmul & Matsumoto, 2008a). Although primary crack widths at level A are wider than that at level B, the average strain in the concrete within the crack spacing (S) at level A being lower than that at level B (Groli, 2014).

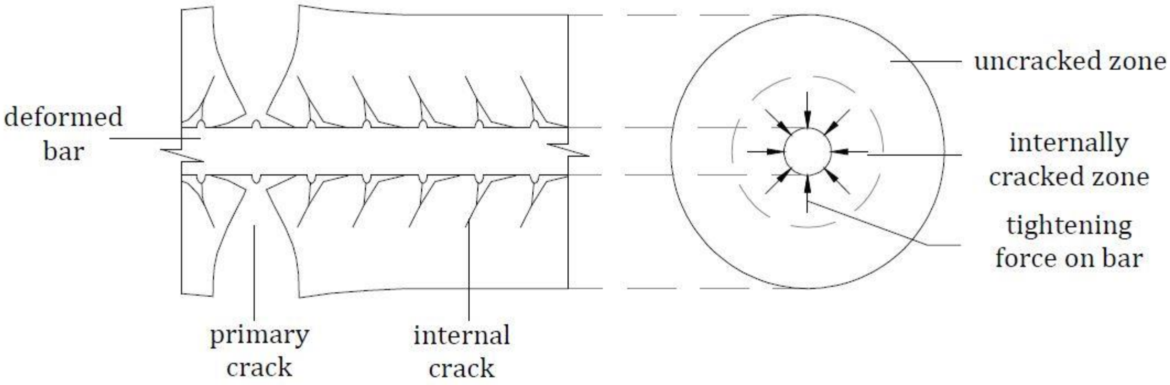

Figure 1.5 Internal cracking around the ribs of reinforcement in reinforced concrete section, Goto (1971).

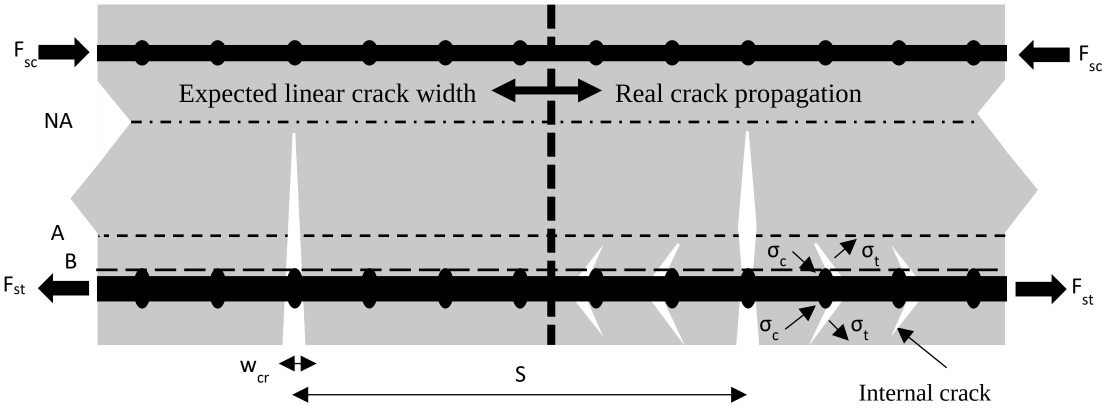

Figure 1.6 Crack closing at reinforcement level due to internal cracking.

1.2.4 Excessive deflections

Excessive deflections have been reported in many structures, especially bridges (Pan, et al., 2011; Maekawa, et al., 2011; Bažant, et al., 2012; Bažant, et al., 2012b; Huang, et al., 2017; Tanimura, et al., 2007). Most of these deflections are attributed to underestimated shrinkage and creep effects. Shrinkage can lead to the development of uneven strains through the height of the section due to asymmetric distribution of reinforcement and uneven moisture loss due to drying, especially through the height of complex sections in large structures with varying section thicknesses. The effect of moisture loss can be accounted for by using models available in design codes and literature. Additional deflections may also result from non-uniform distribution of internal and external restraints to concrete shrinkage, but there is little work done to quantify this effect.

1.3 Scientific Challenges

1.3.1 Non-uniform shrinkage

All current design guidelines still assume that there is no curvature in symmetrically reinforced sections as long as they are not cracked. This is of concern in elements that are designed not to crack like pre-stressed RC elements. However, several studies have shown that shrinkage induced curvatures can occur in rectangular plain concrete sections due to the variance in concrete stiffness (Hobbs, 1974; Hoshino, 1989; Younis, 2014; Jeong, et al., 2015). Concrete stiffness was reported to vary through the sectional height and can lead to differential strains. Such differential strains are caused by water bleeding, higher moisture loss through the casting face (top surface), concrete vibration and distribution of concrete constituents (more coarse aggregate at the bottom while more paste at the top as shown in Figure 1.7). Hence, there is a need to investigate and quantify the parameters causing such differential strains. Also, to understand how these non-uniform shrinkage strains will impact the prediction of curvatures of reinforced concrete sections.

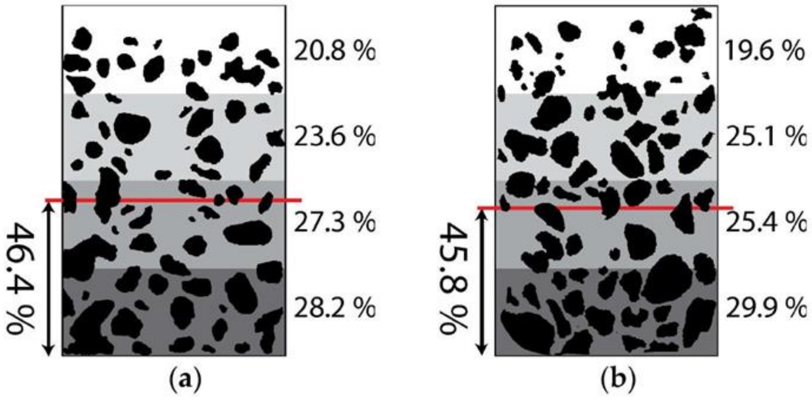

Figure 1.7 Distribution of coarse aggregates through cross section height, Jeong et al (2015).

1.3.2 Impact of shrinkage on crack width prediction

Uniform shrinkage strains (ε_{cs}) are considered in crack width calculations by *fib* MC 2010 (see Equation (1.1)) only for long-term calculations, once the crack stabilisation stage is reached; η_r is only equal to one at the long-term (refer to Table 7.6-2: *fib* MC 2010). It should be noted that most RC structures are designed for the long-term and beyond crack stabilization stage (Carino & Clifton, 1995; Micallef, et al., 2017). However, this is not true for short-term laboratory testing, which is used to calibrate design equations. In laboratory testing, shrinkage strain normally takes place before testing and causes compression strain on the reinforcement and thus, can lead to negative tension stiffening. Hence, there is a need to account for the effect of shrinkage on both short- and long-term crack width prediction (Bischoff, 2011; Zanuy, et al., 2010; Gilbert, 2001; Groli, 2014).

The *fib* MC 2010 approach calculates the maximum crack width (w_{max}) at the bottom soffit of a section by multiplying the crack width (w_d obtained from Equation 1.1) with the ratio (h-x)/(d-x). On the other hand, to determine (w_{max}), Groli (2014) calculated the stiffness eccentricity in the section by trying to homogenise the stiffness of reinforcement and concrete (by assuming uniform shrinkage through the section) to determine sectional curvature as shown in Figure 1.8. However, this approach still assumes zero curvature in non-cracked symmetrically reinforced sections. Hence, in order to quantify the impact of non-uniform shrinkage on crack widths of RC sections, a new method is needed to account for non-uniform section shrinkage that develops before and after cracking of RC elements.

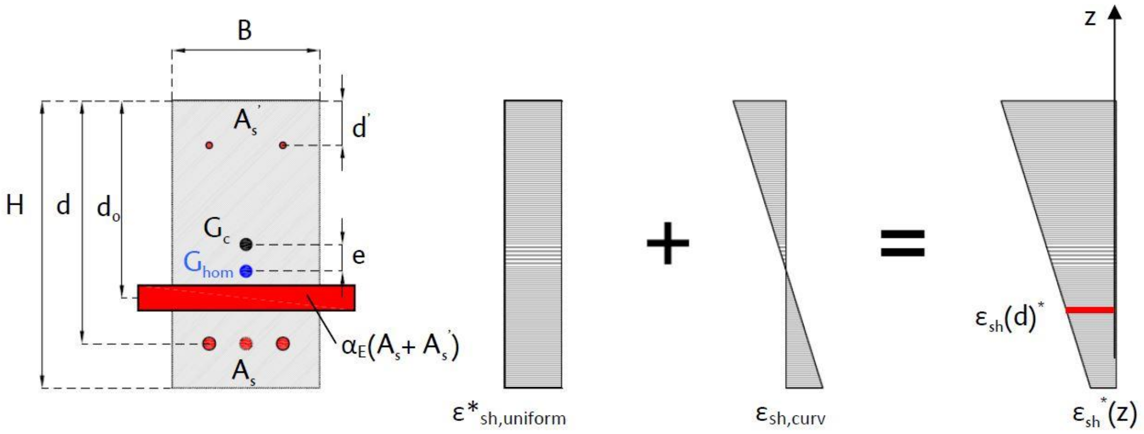

Figure 1.8 Section homogenization and contribution of shrinkage induced curvature, Groli (2014).

1.4 Aim and Objectives

The aim of this study is to contribute to the understanding of how shrinkage and fibres impact short- and long-term deflections and crack widths in RC structures so as to lead to better predictions that can enhance the durability and sustainability of urban infrastructure. This aim will be achieved through the following objectives:

1. Examine non-uniform shrinkage for free and restrained concrete elements reinforced with different blends of manufactured and recycled tyre steel fibre.
2. Examine the contribution of steel fibre blends in crack control of restrained elements.
3. Quantify the effect of aggregate distribution and other concrete constituents on the development of non-uniform shrinkage strains and its associated curvatures.
4. Examine the non-uniform shrinkage of concrete beams reinforced with longitudinal bars and blends of fibres (R/FRC), before and after loading.
5. Examine the effect of reinforcement and steel fibre blends on crack spacing and width.
6. Examine the effect of non-uniform shrinkage on deflections and crack widths predictions.
7. Develop models to account for non-uniform shrinkage in calculations of curvatures of non-cracked reinforced sections and crack widths of RC elements.

8. Support the development of infrastructure applications that utilise by-products and waste materials such as RTSF and GGBS.

1.5 Research Methodology

To address the above objectives, two experimental programmes were developed. The first was designed to examine objectives 1-3 by testing different SFRC blends made with manufactured and recycled fibres, exposed to free and restrained conditions. This involved casting SFRC prisms with three different dosages of manufactured undulated steel fibres (MUSF) and blends of partial and full replacement of MUSF with RTSF. The specimens were examined for free and restrained shrinkage for a period of ten months and then tested in three-point bending to examine their post-cracking behaviour.

The second experimental study was designed to examine objectives 3-6. It involved monitoring the development of non-uniform shrinkage strains in specimens made with different sizes and configurations of reinforcement, as well as the impact of shrinkage and fibres on the development of crack widths and deflections of elements tested in flexure. Shrinkage strain development was monitored for a period of four months in plain concrete, SFRC and asymmetrically RC prisms as well as symmetrically reinforced medium scale beams. Prisms were tested in three-point bending, whilst RC beams (with and without fibres) were tested in four-point bending. Aggregate distribution profiles of three prisms per mix was studied to understand the relationship between the distribution of coarse aggregates and the development of non-uniform shrinkage strains through the section height.

Based on the results obtained from aggregate distribution, an analytical model was derived to predict the development of non-uniform shrinkage. The model was also used to account for non-uniform shrinkage in calculations of crack widths and deflections (Objective 7).

1.6 Thesis Presentation

This thesis comprises five chapters and three appendices. The introductory and concluding chapters are written in normal thesis format while chapters 2 to 4 are written in journal paper format. The three journal papers are described briefly as follows:

Chapter Two entitled "Shrinkage and Flexural Behaviour of Free and Restrained Hybrid Steel Fibre Reinforced Concrete" is based on Al-Kamyani et al. (2018a), *published in Construction and Building Materials*, and addresses objectives 1-3 and 8. It comprises the work done in the first experimental study that examined the effect of different blends of manufactured and recycled tyre steel fibres in free and restrained shrinkage. Shrinkage strain development, assessed on both free and restrained specimens, was found to be non-uniform and not much affected by fibre type and amount. The chapter describes the behaviour of these mixes, subjected to different drying conditions, under flexural testing and compares their residual flexural tensile stresses. The post peak performance was checked according to the recommendations of *fib* MC 2010 and these blends were found to be suitable to replace parts of the longitudinal reinforcement. This study led to the use of different blends of fibres in a second experimental study to examine the development of non-uniform shrinkage strains in RC specimens and as additional reinforcement to control crack widths and deflections in medium scale RC beams, as discussed in the next two chapters.

Chapter Three entitled "Predicting Shrinkage Induced Curvature in Plain and Reinforced Concrete" is based on Al-Kamyani et al. (2018b), *accepted for publication in Engineering Structures*, and addresses objectives 3-4 and 7-8. It presents parts of the work done in the second experimental study that deals with the development of non-uniform drying shrinkage through the height of the plain, SFRC and reinforced (symmetrically and asymmetrically) concrete sections. The study examined the effect of concrete constituents on shrinkage induced curvature of plain and SFRC prisms. It compares the experimental curvatures, obtained from this study and other studies, with predicted curvatures using current principles. Finally, the chapter concludes by proposing a new approach to calculate shrinkage induced curvature including that caused in plain concrete. This model is then used for the better prediction of crack widths and deflections of RC beams, as discussed in the Chapter Four.

Chapter Four entitled “Impact of Shrinkage on Crack Width and Deflections of Reinforced Concrete Beams with and without Steel Fibres” is based on Al-Kamyani et al. (2018c), *submitted to Engineering Structures (with reviewers)*, and addresses objectives 4-8. It discusses mainly the contribution of non-uniform shrinkage and steel fibres in the prediction of crack widths and deflections. The study compares the experimental crack spacing and width with that predicted by MC-10. Finally, the chapter shows the importance of the shrinkage strains and accordingly proposes amendments to the MC-10 approach to consider shrinkage and curvatures in the calculations for the mean strain.

Chapter Five comprises concluding remarks and recommendations for future work based on Chapters 2-4. Additional comments on enhancement of infrastructure life span as to ensure durable and sustainable construction are also provided.

References

ACI-231R, 2010. *Report on Early-Age Cracking: Causes, Measurement, and Mitigation,* Farmington Hills: American Concrete Institute.

Al-Kamyani, Z. et al., 2018a. Shrinkage and Flexural Behaviour of Free and Restrained Hybrid Steel Fibre Reinforced Concrete. *Construction and Building Materials,* Volume 189C, pp. 1007-1018.

Al-Kamyani, Z., Gaudagnini, M. & Pilakoutas, K., 2018b. Predicting Shrinkage Induced Curvature in Plain and Reinforced Concrete. *Engineering Structures,* Volume Accepted for publication.

Al-Kamyani, Z., Guadagnini, M. & Pilakoutas, K., 2018c. Impact of Shrinkage on Crack Width and Deflections of Reinforced Concrete Beams with and without Steel Fibres. *Engineering Structures,* Volume Submitted with reviewers.

Aly, T. & Sanjayan, J. G., 2008. Shrinkage cracking properties of slag concretes with one-day curing. *Magazine of Concrete Research,* 1(60), pp. 41-48.

Angelakopoulos, H., Papastergiou, P. & Pilakoutas, K., 2015. Fibrous roller-compacted concrete with recycled materials – feasibility study. *Magazine of Concrete Research,* pp. 1-11.

Baricevic, A., Bjegovic, D. & Skazlic, M., 2017. Hybrid Fiber–Reinforced Concrete with Unsorted Recycled-Tire Steel Fibers. *Journal of Materials in Civil Engineering,* 29(6), pp. 1-10.

Bartolac, M. et al., 2016. *Punching of slabs reinforced with recycled steel fibres from used tyres.* Dundee, University of Dundee – Concrete Technology Unit.

Bazant, Z. P. & Baweja, S., 2001. *Creep and Shrinkage Prediction Model for Analysis and Design of Concrete Structures: Model B3,* Michigan: ACI.

Bažant, Z. P., Yu, Q. & Li, G.-H., 2012b. Excessive Long-Time Deflections of Prestressed Box Girders. II: Numerical Analysis and Lessons Learned. *Journal of Structural Engineering,* 138(6), pp. 687-696.

Bažant, Z. P., Yu, Q. & Li, G.-H., 2012. Excessive Long-Time Deflections of Prestressed Box Girders. I: Record-Span Bridge in Palau and Other Paradigms. *Journal of Structural Engineering,* 138(6), pp. 676-686.

Beeby, A. W. & Scott, R. H., 2005. Cracking and deformation of axially reinforced members subjected to pure tension. *Magazine of Concrete Research,* 57(10), p. 611–621.

Bischoff, P. H., 2011. Effects of shrinkage on tension stiffening and cracking in reinforced concrete. *Can. J. Civ. Eng.,* 28(3), p. 363–374.

Carino, N. J. & Clifton, J. R., 1995. *Prediction of Cracking in Reinforced Concrete Structures,* Gaithersburg: National Institute of Standards and Technology, U.S. Department of Commerce.

Castel, A. et al., 2016. Creep and drying shrinkage of a blended slag and low calcium fly ash geopolymer Concrete. *Materials and Structures,* 49(5), p. 1619–1628.

Deng, P. & Matsumoto, T., 2017. Estimation of the Rebar Force in RC Members from the Analysis of the Crack Mouth Opening Displacement Based on Fracture Mechanics. *Advanced Concrete Technology,* Volume 15, pp. 81-93.

fib, 2013. *fib Model Code for Concrete Structures 2010,* Berlin, Germany: Wilhelm Ernst & Sohn.

Gilbert, R. I., 2001. Shrinkage, Cracking and Deflection the Serviceability of Concrete Structures. *Electronic Journal of Structural Engineering,* Volume 1, pp. 15-37.

Goto, Y., 1971. Cracks Formed in Concrete Around Deformed Tension Bars. *ACI Journal,* 68(4), pp. 244-251.

Graeff, A., 2011. *Long-term performance of recycled steel fibre reinforced concrete for pavement applications,* Sheffield: The University of Sheffield.

Gribniak, V. et al., 2012. Deriving stress–strain relationships for steel fibre concrete in tension from tests of beams with ordinary reinforcement. *Engineering Structures,* Volume 42, p. 387–395.

Groli, G., 2014. *Crack width control in RC elements with recycled steel fibres and applications to integral structures: theoritical and experimental study,* Madrid: Polytechnic University of Madrid.

Groli, G. & Caldentey, A. P., 2017. Improving cracking behaviour with recycled steel fibres targeting specific applications – analysis according to fib Model Code 2010. *fib Structural Concrete,* Volume 18, pp. 29-39.

Groli, G., Caldentey, A. P. & Soto, A. G., 2014. Cracking performance of SCC reinforced with recycled fibres – an experimental study. *fib Structural Concrete,* 15(2), pp. 136-153.

Hobbs, D. W., 1974. Influence of Aggregate Restraint on the Shrinkage of Concrete. *ACI Journal,* pp. 445-450.

Hoshino, M., 1989. Relation Between Bleeding, Coarse Aggregate, and Specimen Height of Concrete. *ACI Materials Journal,* 86(2), pp. 185-190.

Huang, H., Garcia, R., Guadagnini, M. & Pilakoutas, K., 2017. Effect of section geometry on development of shrinkage-induced deformations in box girder bridges. *Materials and Structures,* 50(222), pp. 1-14.

Hu, H. et al., 2018. Mechanical properties of SFRC Using blended manufactured and recycled tyre steel fibres. *Construction and Building Materials,* Issue 163, pp. 376-389.

Jafarifar, N., 2012. *Shrinkage Behaviour of Steel Fibre Reinforced Concrete Pavements,* Sheffield: The University of Sheffield.

Jeong, J.-H., Park, Y.-S. & Lee, Y.-H., 2015. Variation of Shrinkage Strain within the Depth of Concrete Beams. *Materials,* pp. 7780-7794.

Jianyong, L. & Yan, Y., 2001. A study on creep and drying shrinkage of high performance concrete. *Cement and Concrete Research,* Issue 31, pp. 1203-1206.

Lin, F. et al., 2012. Cracking analysis of massive concrete walls with cracking control techniques. *Construction and Building Materials,* Issue 31, pp. 12-21.

Maekawa, K., Chijiwa, N. & Ishida, T., 2011. Long-term deformational simulation of PC bridges based on the thermo-hygro model of micro-pores in cementitious composites. *Cement and Concrete Research,* Issue 41, p. 1310–1319.

Martinelli, E., Caggiano, A. & Xargay, H., 2015. An experimental study on the post-cracking behaviour of Hybrid Industrial/Recycled Steel Fibre-Reinforced Concrete. *Construction and Building Materials,* Volume 94, pp. 290-298.

Micallef, M., 2015. *Crack control in base-restrained reinforced concrete walls,* London: Imperial College London.

Micallef, M., Vollum, R. L. & Izzuddin, B. A., 2017. Crack development in transverse loaded base-restrained reinforced concrete walls. *Engineering Structures,* Volume 143, pp. 522-539.

Mitchell, W. & Arya, C., 2015. *The effect of combining shrinkage-reducing-admixture with ground, granulated, blast-furnace slag on the drying shrinkage of concrete,* London: UCL Department of Civil, Environmental and Geomatic Engineering.

Nazmul, I. & Matsumoto, T., 2008a. High resolution COD image analysis for health monitoring of reinforced concrete structures through inverse analysis. *International Journal of Solids and Structures,* 45(1), p. 159–174.

Nazmul, I. M. & Matsumoto, T., 2008b. Regularization of inverse problems in reinforced concrete fracture. *Journal of Engineering Mechanics,* 134(10), pp. 811-819.

Pan, Z., Fu, C. C. & Jiang, Y., 2011. Uncertainty Analysis of Creep and Shrinkage Effects in Long-Span Continuous Rigid Frame of Sutong Bridge. *Journal of Bridge Engineering,* 16(2), pp. 248-258.

Pérez, C. A., Mestre, G. C. & Mendoza, C. J., 2017. *A new way to sustainability designing more slender building structures by using recycled steel fibres.* Zadar, s.n.

Tanimura, M., Sato, R. & Hiramatsu, Y., 2007. Serviceability Performance Evaluation of RC Flexural Members Improved by Using Low-Shrinkage High-Strength Concrete. *Journal of Advanced Concrete Technology,* 5(2), pp. 149-160.

Tan, K.-H., Paramasivam, P. & Tan, K.-C., 1995. Cracking Characteristics of Reinforced Steel Fiber Concrete Beams under Short- and Long-Term Loadings. *Advanced Cement Based Materials,* Issue 2, pp. 127-137.

Vandewalle, L., 2000. Cracking behaviour of concrete beams reinforced with a combination of ordinary reinforcement and steel fibers. *Materials and Structures,* Volume 33, pp. 164-170.

Vasanelli, E., Micelli, F., Aiello, M. A. & Plizzari, G., 2013. *Analytical prediction of of crack width of FRC/RC beams under short and long term bending condition.* Toledo, International Center for Numerical Methods in Engineering.

Younis, K. H., 2014. *Restrained shrinkage behaviour of concrete with recycled materials,* Sheffield: The University of Sheffield.

Zanuy, C., Fuente, P. d. l. & Albajar, L., 2010. Estimation of parameters defining negative tension stiffening. *Engineering Structures*, Volume 32, pp. 3355-3362.

Chapter 2: Shrinkage and Flexural Behaviour of Free and Restrained Hybrid Steel Fibre Reinforced Concrete

Al-Kamyani*, *Z., *Figueiredo, F. P., Hu, H., Guadagnini, M., Pilakoutas, K., 2018a. Shrinkage and Flexural Behaviour of Free and Restrained Hybrid Steel Fibre Reinforced Concrete. Construction and Building Materials, Volume 189C, pp. 1007-1018.*

Abstract

The effect of restrained shrinkage on the mechanical performance of concrete and steel fibre reinforced concrete (SFRC) requires more investigation, especially when using recycled tyre steel fibre (RTSF). This paper examines the free and restrained shrinkage strains and the mechanical performance of seven SFRC mixes. Results show that both free and restrained average shrinkage strains are very similar in all blends of fibres and they exhibited non-uniform shrinkage through the height of the section. All examined blends meet strength requirements by MC-2010 for fibres to replace part of the conventional reinforcement in RC structures.

This chapter consists of a "stand alone" journal paper and includes a relevant bibliography at the end of the chapter. Additional information and further test results are presented in Appendix A.

2.1 Introduction

In water retaining structures or bridge elements, serviceability limit state (SLS) design aims to control crack widths to achieve a target life span by providing relatively large amounts of surface steel reinforcement. In such structures, the additional reinforcement is required to control cracks induced by restrained shrinkage, which creates further constructability challenges. To reduce the amount of additional surface reinforcement, shrinkage can be mitigated by reducing paste/aggregate ratio, minimising C_3S content in cement, using expansive or shrinkage reducing additives, and internal curing materials (ACI-231R, 2010). However, these solutions are not universally accepted, tend to be expensive and can increase the environmental impact of concrete.

Shrinkage cracking can also be controlled by adding randomly distributed steel fibres as successfully utilised by the construction industry in pavements and tunnels (Buratti, et al., 2013; Banthia, et al., 1996; Younis, 2014). Steel fibres can enhance the performance of concrete in flexure, shear and punching whilst at the same time help control shrinkage cracking and reduce spalling (Zamanzadeh, et al., 2015; Yoo, et al., 2015; Bartolac, et al., 2016), depending on the amount and characteristics of the steel fibres, such as type, shape and aspect ratio (Kaïkea, et al., 2014; Martinelli, et al., 2015; Yazıcı, et al., 2007; Chanvillard & A'itcin, 1996). Recycled tyre steel fibres (RTSF) are also available and due to their nature (less than 0.4 mm diameter) were found to be better in controlling micro-cracks whilst manufactured steel fibres are thicker (0.5-1.0 mm in diameter) and longer (up 65 mm) and in general excel after micro-cracks have developed (Younis & Pilakoutas, 2016; Kaïkea, et al., 2014). In flexure, RTSF can improve the toughness and post cracking performance and can successfully substitute manufactured fibres partially or fully in some applications (Martinelli, et al., 2015; Centonze, et al., 2012).

In most published research on RTSF (Younis, 2014; Graeff, 2011; Jafarifar, 2012), a single type of fibre is used as reinforcement. Recently, some studies investigated blends of manufactured and recycled steel fibres with different shapes and aspect ratios (Martinelli, et al., 2015; Akcay & Tasdemir, 2012), but the recycled fibres used were not classified raising reliability and repeatability concerns. The cleaning process of RTSF has been improved significantly recently and improved classified fibres have become available (Hu, et al., 2017; Caggiano, et al., 2015; Sengul, 2016). Hence, there is a need to investigate the effect of hybrid steel fibres (both manufactured and classified RTSF) on concrete exposed to free and restrained shrinkage.

The impact of steel fibres on free shrinkage of concrete is not clearly understood, with some researchers reporting an increase due to the increase in air voids, whilst others reporting either a decrease due to the internal restraint provided by the fibres or insignificant changes due to the cancelling effect of the two actions (Graeff, 2011; Zhang, et al., 2015; Younis, 2014; Jafarifar, 2012). Nonetheless, the effect of steel fibres on free shrinkage is known to vary depending on water-to-binder ratio, volume and type of admixtures, method of concrete laying (conventional, self-compacted concrete (SCC) or roller compacted concrete (RCC)), time of vibration, etc. (Zdanowicz & Marx, 2018).

In concrete structures, shrinkage of concrete is restrained by different actions internally and externally. External restraint can arise due to friction or reaction against the ground, concrete supporting elements or adjacent rigid structures, whilst internal restraint is provided by aggregates and reinforcement (Hobbs, 1974; Gilbert, 2001). It is also known that aggregates tend to settle and concentrate at the bottom of the mould whilst water and air rise due to vibration and surface tamping. These phenomena can cause differences in compressive strength and elastic modulus at the top and bottom of the element (Hoshino, 1989; Jeong, et al., 2015). As more paste and water are found near the top surface, this can cause much higher shrinkage strains in that region. Non-uniform distribution of aggregates and water can create non-uniform shrinkage through a section and lead to additional curvature in concrete elements (Younis, 2014). RILEM TC 107-CSP (1998) determines shrinkage from the change in the distance between the centres of the two ends of a cylinder, which means that its approach is unable to capture the effect of aggregate sedimentation. To the knowledge of the authors, none of the design codes or standards deal with curvature due to the non-uniform shrinkage and this can lead to underestimate of long-term deflections and crack widths.

Free shrinkage tests on small elements are not normally able to develop enough internal tensile stresses to crack the concrete, hence, restrained shrinkage tests are needed to understand the cracking behaviour of restrained concrete (Younis & Pilakoutas, 2016). Restraint causes tensile stresses in the concrete, which theoretically could increase with time due to concrete maturity, but creep is expected to relieve some of these stresses and reduce the probability of cracking (Gilbert, 2001; Castel, et al., 2016; Neville, 2004). Normally, it is difficult to quantify the degree of restraint imposed on an element, as it depends on the type of application, the location of the member in the structure and environmental conditions (Banthia, et al., 1996; Gilbert, 2016). However, there are several tests to assess the restrained shrinkage of concrete (ACI-231R, 2010), with the most used being the ring test (Grzybowski & Shah, 1990; Choi, et al., 2015). Though simple and popular, this test can only be used for comparison purposes, as it only detects the stress and time of the first crack. Another disadvantage of this approach is that the sectional size needs to be kept relatively small (to enable cracking at a reasonable time frame) and this enhances boundary effects and makes the concrete section less representative of sections in practice.

Active systems with larger specimens (Bloom & Bentur, 1995; Paillere, et al., 1989; Altoubat & Lange, 2001) can be used to restrain concrete shrinkage by fixing one end of a linear element whilst the other end is attached to an actuator which keeps the total length constant. In active systems, cracks tend to occur when the strain is being adjusted and this can affect the time at which cracking takes place (Aly & Sanjayan, 2008). Furthermore, full and active restrain is rarely found in practice, where restrain depends on the relative stiffness of the restraining structure and is mitigated by creep. For these reasons, and for simplicity, passive systems (Leemann, et al., 2011; Loser & Leemann, 2009) can be used by restraining concrete specimens through fixing bolts onto rigid structural elements. Younis (2014) proposed the use of a passive restraining frame able to hold three prisms at the same time. The use of linear elements also enables shrinkage measurements to be taken at different levels through the section and examine shrinkage curvature.

The aim of this work is to examine the effect of restrain on shrinkage and mechanical performance of hybrid SFRC mixes. The performance of SFRC prisms comprising different fibre blends and subjected to a combination of restraining, curing and drying conditions are studied and compared. Ground granulated blast-furnace slag (GGBS) and RTSF are used, along with manufactured fibres, to control the amount of shrinkage strains and limit the propagation of concrete cracking under restrained conditions.

This paper comprises three main sections along with an introduction and conclusions. The first section presents the experimental programme including the examined parameters, the physical and mechanical characteristics of the examined materials and testing methodology. This is followed by a discussion on the results obtained from free and restrained shrinkage tests of hybrid SFRC prisms. The level of restrain imposed by restraining frames is assessed through a finite element numerical analysis and used to gain additional insight into the effect of restraint level on overall behaviour. Finally, in the third section the paper discusses the effect of restrained shrinkage and different drying conditions on the flexural performance of the examined concrete mixes.

2.2 Experimental Programme

2.2.1 Parameters

The experimental programme examined seven SFRC mixes in addition to a control mix made of plain concrete, as shown in Table 2.1. Each mix was used to manufacture twelve control cubes (100 mm), six prisms (100x100x500mm) for free shrinkage measurement and three prisms, which were cast in a restraining steel frame as shown in Figure 2.1a (Younis, 2014). All specimens were demoulded one day after casting. Three prisms (out of the six) were stored in a mist room (MR) to monitor autogenous shrinkage. The other three specimens were stored under controlled environmental (CR) conditions (temp: 23±2 °C and RH: 40±5%) to quantify drying shrinkage. The restrained specimens (RS) were stored under the same conditions as the CR specimens.

Table 2.1 Steel fibre types and contents.

Mix	MUSF L (mm)	MUSF Ø (mm)	MUSF Dose (kg/m^3)	RTSF Dose (kg/m^3)	RTPF Dose (kg/m^3)	Batch number
P	-	-	-	-	-	1, 2, 3
M30	55	0.8	30	-	-	1
M20R10	55	0.8	20	10	-	2
M20R10P1	55	0.8	20	10	1	3
R30	-	-	-	30	-	3
M35	60	1.0	35	-	-	1
M45	60	1.0	45	-	-	1
M35R10	60	1.0	35	10	-	2

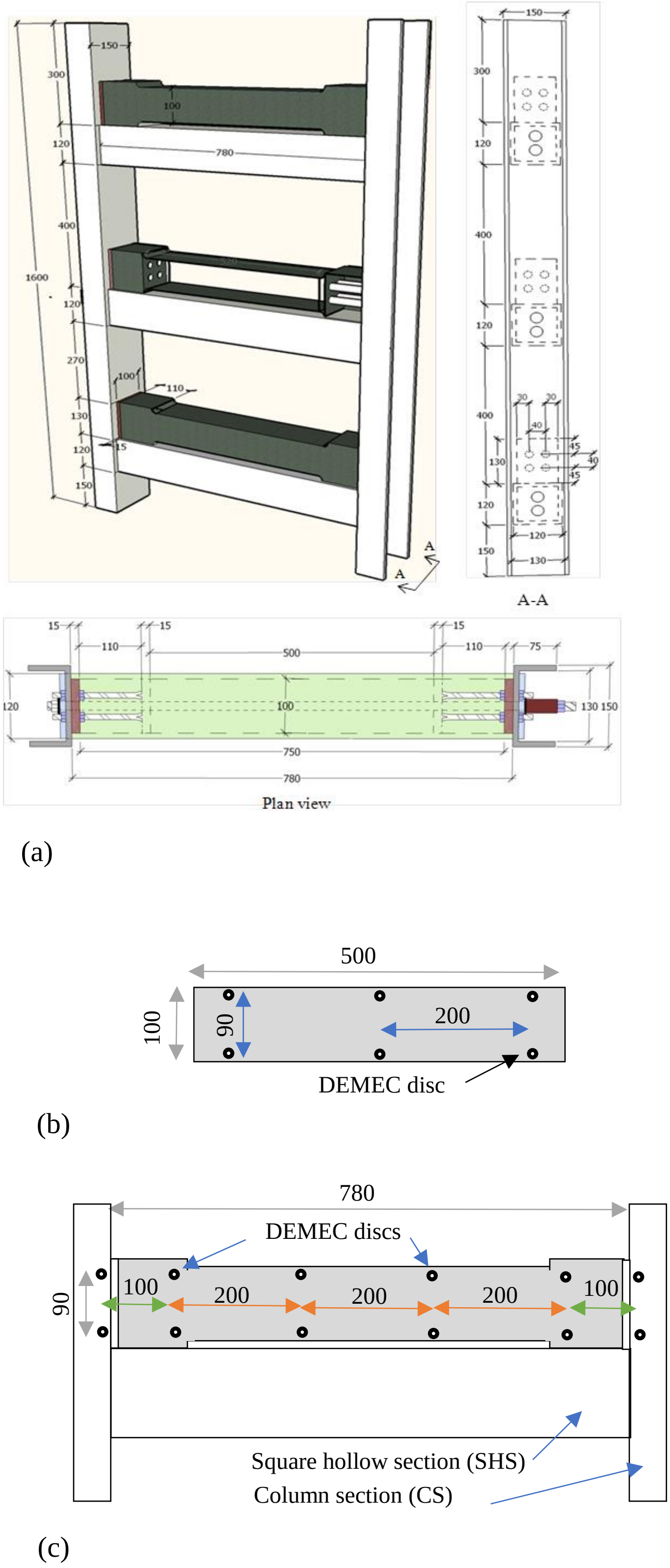

*All dimensions are in mm
*Sketch is not to scale

Figure 2.1 Restraining frame used to restrain concrete prisms (a) and layout of shrinkage DEMEC distribution in free (b) and restrained prisms (c).

2.2.2 Measurements

Shrinkage measurements were taken using a 200-mm demountable mechanical "DEMEC" strain gauge at the top and bottom of both sides of all prisms for 300 days. Figure 2.1 (b and c) shows the measurement layout for free and restrained shrinkage, respectively. It should be noted that a 100 mm "DEMEC" strain gauge was used to measure the deformation at the boundaries between concrete and restraining frame.

At the end of the shrinkage measurement period, CR prisms were dried in an oven until constant weight was observed. This was always achieved after 3 cycles at 50℃ and 3 cycles at 100℃, each cycle lasting 24 hours. After that and prior to flexural testing, all prisms were notched (on one of the sides as cast) at the centre to 1/6 of the sectional depth. They were then tested in three-point flexure by controlling the crack mouth opening displacement (CMOD) according to BS EN 14561:2005 (EN-14651, 2005). The exact dimensions of the prisms were taken to the nearest 0.5 mm to account for casting imperfections. Each prism was then split into two pieces and each portion tested for compressive strength according to BS 1881-119 (BSI-12, 1998). Concrete compressive strength was also obtained from cube test at 7 days, 28 days and 14 months.

2.2.3 Materials

Two types of steel fibres were used in this programme: manufactured undulated fibres (MUSF) with a nominal strength of 1450 MPa (two types of undulated length/diameter (L/Ø) 55/0.8 and 60/1) and recycled tyre steel fibres (RTSF) with strength greater than 2000 MPa (Hu, et al., 2018). The average diameter of RTSF was about 0.2 mm, whilst the average length, determined using a special optical device, at 50% cumulative mass, was about 20 mm as shown in Figure 2.2. Both single and blended steel fibres were used to reinforce the concrete in three amounts of 30 kg/m^3, 35 kg/m^3 or 45 kg/m^3. Mix M20R10P1 also contained 1 kg/m^3 of recycled tyre polymer fibres (RTPF) to examine the effect of polymer fibres in controlling shrinkage cracking.

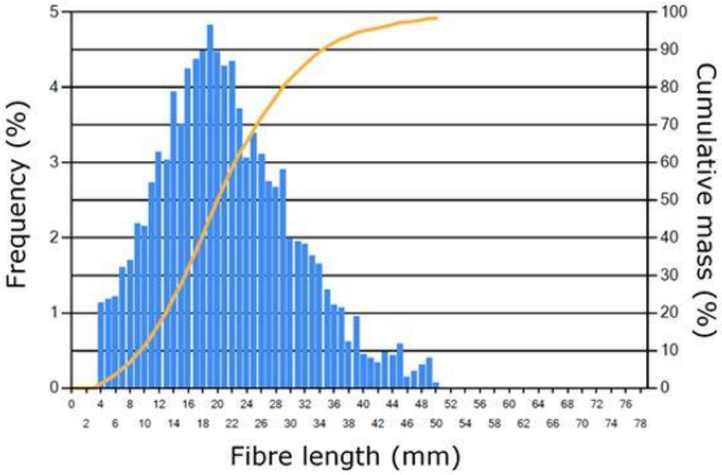

Figure 2.2 Length distribution of classified RTSF.

Three batches of ready mix concrete were used to manufacture the test specimens (see Table 2.2). The mix design is based on a design used in Europe for slabs-on-grade. The binder consisted of 50% CEM 1 and 50% GGBS.

Table 2.2 Nominal mix composition.

Composition	**Quantity (kg/m^3)**
Cement 52.5N CEM1	150
GGBS (BS EN 15167-1:2006)	150
4/20 River aggregates	1097
0/4 River sand	804
Water/binder ratio	0.55
SP (Master Polyheed 410)	1.5 L

2.3 Results and Discussion on Shrinkage Strains

2.3.1 Free shrinkage strains

2.3.1.1 Drying shrinkage

The free shrinkage strains versus time at the top and bottom of the specimen (T for top and B for bottom) are shown in Figure 2.3 (a and b), respectively. The small fluctuations in the curves are a result of small temperature and relative humidity changes in the control room. Shrinkage strain predictions of Eurocode (CEN, 2008) and *fib* Model Code (fib, 2013), shown in dotted lines, are higher than the experimental strains, possibly due to the high amount of GGBS and differences in first measurement time. The EC and *fib* models consider conventional cements and do not consider other cementitious materials in their predictions. GGBS was found by some authors to reduce the rate and ultimate value of both autogenous and drying shrinkage (Aly & Sanjayan, 2008; Jianyong & Yan, 2001; Mitchell & Arya, 2015) as the fineness of GGBS can close the concrete pores and prevent water from escaping the substrate (Castel, et al., 2016). Codes recommend taking the first shrinkage measurements within 3 minutes after demoulding, but due to the high amount of DEMEC discs used in this study, the first shrinkage measurement was taken after 6 hours.

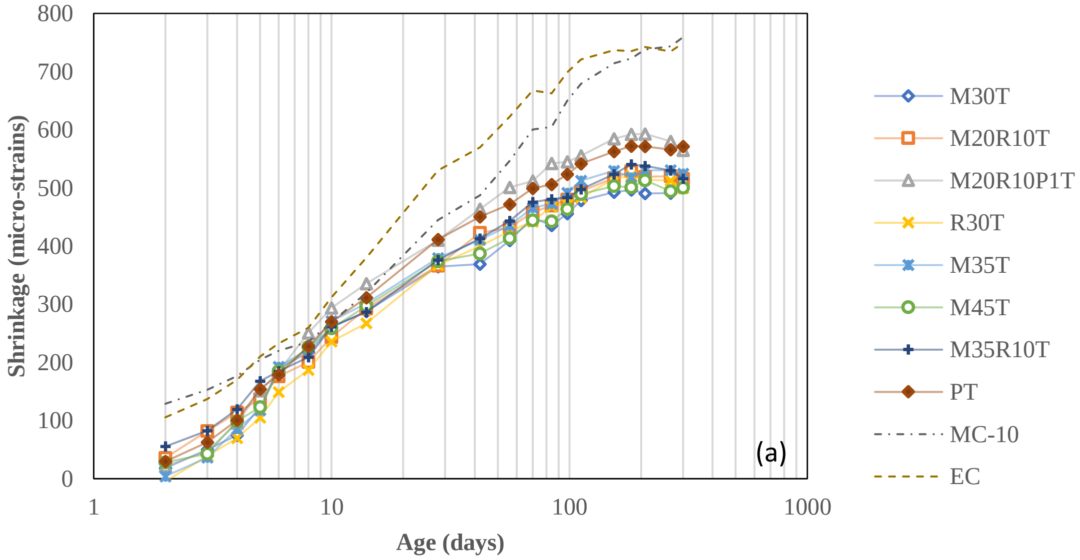

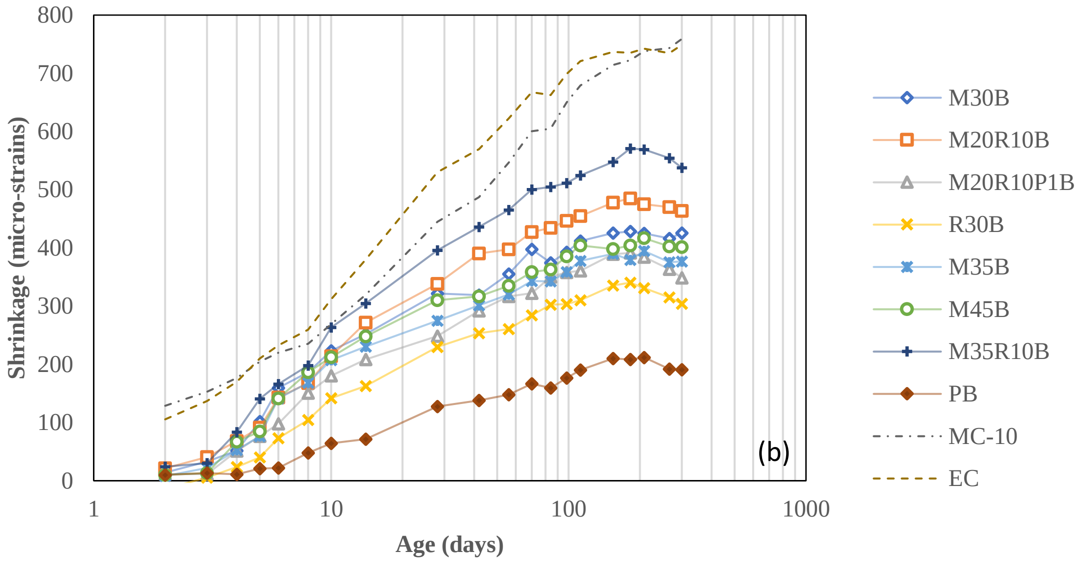

Figure 2.3 Free shrinkage strains at top (a) and bottom (b).

It is difficult to determine, from the results, the precise effect of steel fibre type/dosage on free shrinkage. However, it is evident that shrinkage strains at the top are overall higher than at the bottom. Plain concrete shows higher shrinkage strains at the top than SFRC mixes, whilst showing the lowest strain at the bottom. This may be due to the fact that superplasticiser was added to the plain concrete (to maintain the workability of concrete after the addition of steel fibres) and this may have led to more bleeding than in the other mixes. Shrinkage strains of SFRC were between 500 and 600 micro-strains at the top and between 300 and 500 micro-strains at the bottom. The scatter of the bottom measurements was higher than that of the top measurements possibly due to the fact that the presence of steel fibres prevented some of the coarse aggregates from settling to the bottom of the mould (Al-Kamyani, et al., 2017). The varying amounts of coarse aggregates at the bottom of the section resulted in varying degrees of restrain and thus a higher scatter in shrinkage resistance. Non-uniform shrinkage strains in these rectangular sections can only be the result of non-uniform distribution of the coarse aggregates across the depth of concrete section, which also creates curvature that will contribute to the global deformation of the members (Jeong, et al., 2015; Al-Kamyani, et al., 2017).

2.3.1.2 Drying shrinkage and mass loss relationship

The relationship between total free shrinkage and mass loss of the CR specimens is shown in Figure 2.4. Though the water content in the original mix was the same for all mixes, workability decreased after introducing steel fibres as some of the free water was adsorbed in wetting the surface of the fibres. Hence, it appears that, as a result, the plain concrete mix lost more free water than the SFRC mixes during the first few days of drying.

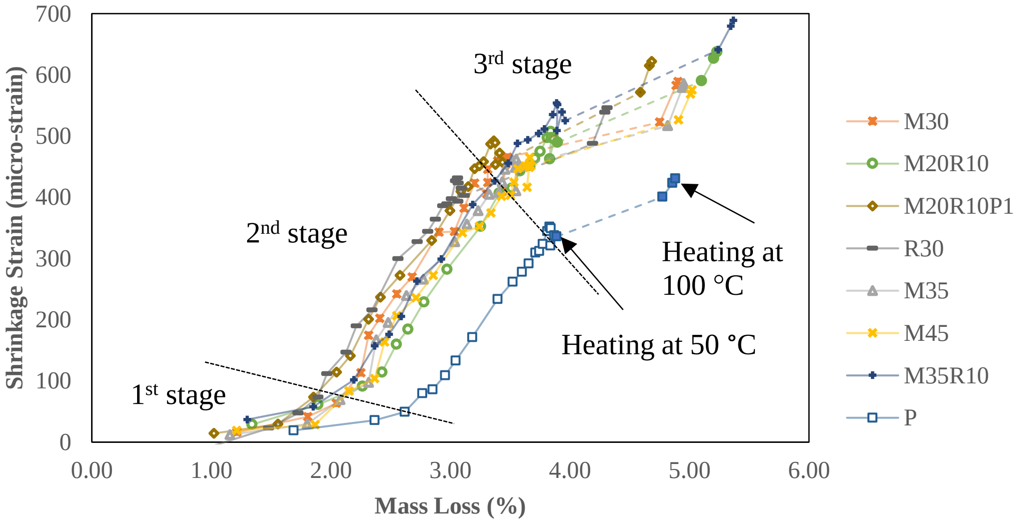

Figure 2.4 Free shrinkage and mass loss relationship.

The behaviour of each mix shows three stages: 1) the first five days of rapid drying, 2) normal drying and 3) accelerated drying in the oven. The first stage indicates rapid mass loss possibly due to the evaporation of the free water (Filho, et al., 2005). The second stage tends to show a linear trend in mass loss with free shrinkage until mass loss stabilises and the moisture inside the samples become approximately equal to the relative humidity of the atmosphere (Leemann, et al., 2011). The third stage was created artificially due to accelerated drying of the prisms in the oven initially at 50 °C and then at 100 °C. During the first three cycles at 50 °C, there was little change in mass loss and shrinkage. However, once the temperature was elevated to 100 °C, there was a noticeable increase in mass loss and drying shrinkage.

The purpose of completely drying the samples was to assess if it is possible to predict the ultimate drying shrinkage strains from mass loss by assuming that the relationship between shrinkage and mass loss is linear. However, during accelerated drying, there was more mass loss (on average 14%) or less shrinkage (on average 19%) than expected under normal drying conditions (second stage). This phenomenon may be attributed partly to micro diffusion of water from gel pores to capillary pores, which helps to free larger amounts of water (Bazant & Baweja, 2001), or due to the micro cracking due to differential temperature at the surface of the concrete during cooling. This was evident in the plain concrete that showed the highest number of micro-cracks on the surface. Therefore, heating the samples at 100 °C appears to have altered the mechanism of drying due to micro diffusion of water or micro-cracking, which was not intended by the experiment. However, the ultimate mass loss could be obtained at lower temperatures, e.g. at about 80 °C without causing damage in the concrete micro-structure, and could be used to predict the long-term evolution of drying shrinkage strain and its impact on the health of the structure.

2.3.1.3 Humid concrete shrinkage strains

Figure 2.5 shows the evolution of shrinkage strain in specimens conditioned in a mist room. Negative strain values mean that the samples are swelling. The non-uniformity in the curves between age of 50 and 70 days was due to unexpected fluctuations in moisture inside the mist room (due to some mechanical problems). The initial swelling in the samples can be attributed to swelling in GGBS grains, which can absorb water and lead to disjointing pressure (Craeye, et al., 2010; Leemann & Lura, 2014), as they get fully saturated during the hydration process. As a result, swelling continues until the relative humidity in the matrix becomes less than the relative humidity in the pores of the grains (Snoeck, et al., 2015). However, the plain concrete specimens swelled less compared to those reinforced with fibres, possibly due to their lower permeability (Beddar, 2005).

Swelling continued for the entire 11-month period of measurements, which indicates that swelling due to absorption of moisture is higher than any autogenous shrinkage strains. Model B3 (Bazant & Baweja, 2001) and *fib* MC-2010 (fib, 2013) predict expansion in any concrete stored under relative humidity of about 100%. Predictions by model B3 and *fib* MC-2010 are shown in dashed lines in Figure 2.5 (indicated as B3 and MC, respectively). B3 is found to be in agreement with the initial experimental results while MC is close to the plain concrete throughout the measuring period. It should be noted that this analysis was carried out using CEM I as a cementitious material in both models as there is no provision for GGBS in the current formulations. *fib* MC-2010 was found to predict expansion strains up to two times greater than those induced by autogenous shrinkage strains.

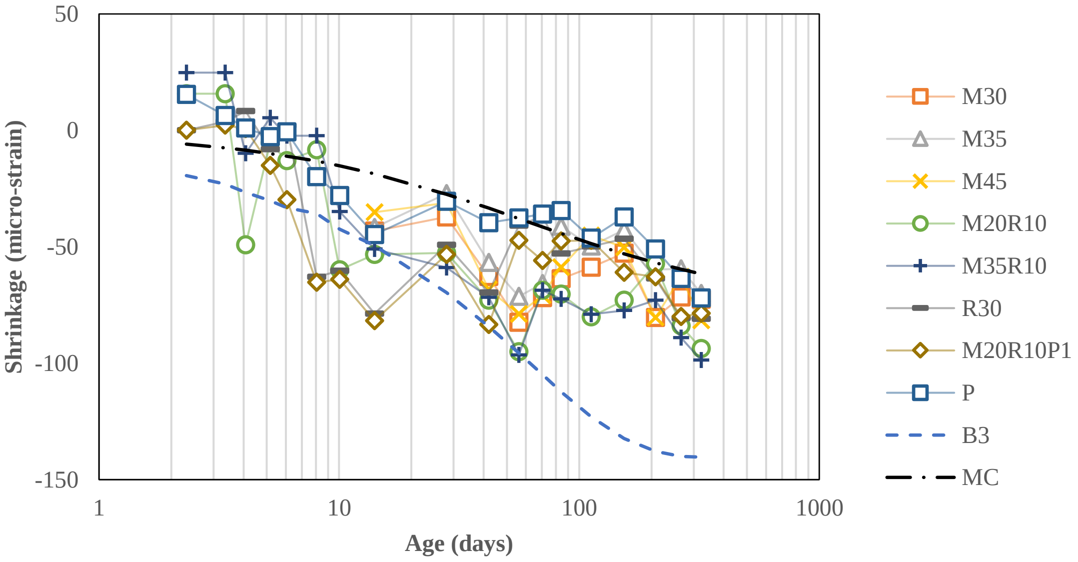

Figure 2.5 Humid concrete strain results.

2.3.2 Restrained shrinkage strains

Figure 2.6 (a and b) shows the restrained shrinkage strains of all tested prism at the top (T) and bottom (B), respectively. In general, prisms made with different mixes exhibited similar restrained shrinkage strain development, apart from those made with mixes M35 and R30, which started deviating from the rest between the age of 14 and 28 days. No significant development in shrinkage took place in mix M35, possibly due to early age micro-cracking near the anchors, whilst there was a remarkable increase in mix R30, possibly due to slip at the interface between concrete and anchors.

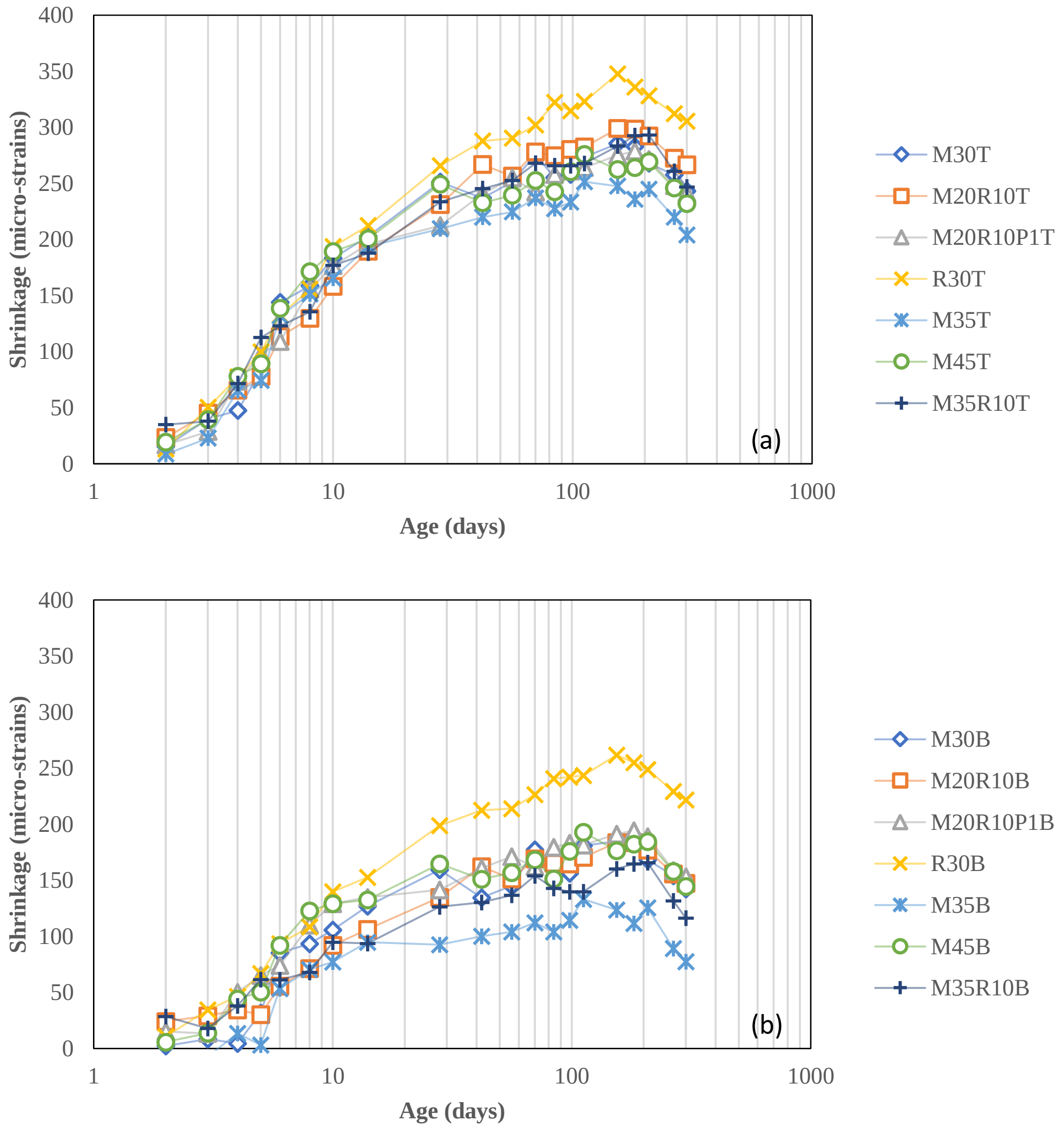

Figure 2.6 Restrained shrinkage strains at top (a) and bottom (b).

Shrinkage strains varied between 250 and 300 micro-strains at the top and between 160 and 180 micro-strains at the bottom at the age of 180 days. These strains decreased after 200 days, possibly as a result of creep and the development of micro-cracks inside the concrete. The similarity in the shrinkage strain levels exhibited by all specimens indicates that the effect of steel fibre type and dosage is insignificant with respect to restrained shrinkage, as was also observed in free shrinkage prisms. The scatter in restrained shrinkage curves is less than that seen in Figure 2.3b possibly as the effect of end restraint is more dominant than the effect of coarse aggregate distribution. It should be noted that some of the curvature induced in the specimens can be attributed to restraint loss at the external boundaries between the concrete and steel anchors and/or differential aggregate distribution.

2.3.3 Performance of the restraining frame

To understand the degree of restraint provided by the frame, the "restraining factor" (RF) needs to be determined. RF is defined as the difference in strain between the free and restrained elements (see Equation (2.1)). The RF values for the passive restraining frame used varied between 0.5 and 0.6. The theoretical values using simple elastic calculations is higher at 0.73 (Younis & Pilakoutas, 2016).

$$RF = \frac{\varepsilon_{sh,free} - \varepsilon_{sh,restrained}}{\varepsilon_{sh,free}} \qquad (2.1)$$

Drying shrinkage induces shortening of the concrete specimens, which are restrained by the frame through the anchors. Figure 2.7 shows that there is some additional deformation at the boundaries between concrete and the restraining frame over a gauge length of 100 mm (see Figure 2.1c) for a typical mix (M20R10P1) at the top (T) and bottom (B) of each specimen (1 - top, 2 - middle and 3 - bottom prism in the restraining frame). The deformations are higher at the top of prisms 2 and 3 whilst they are similar for all prisms at the bottom level. Most of the deformation takes place during the first 50 days. This deformation is the result of: a) elastic deformation of the concrete, b) anchor elongation, c) slip at the interface between concrete and anchors and d) local deformation of the frame. These additional deformations b), c) and d) contribute to the differences between the actual and theoretical RF.

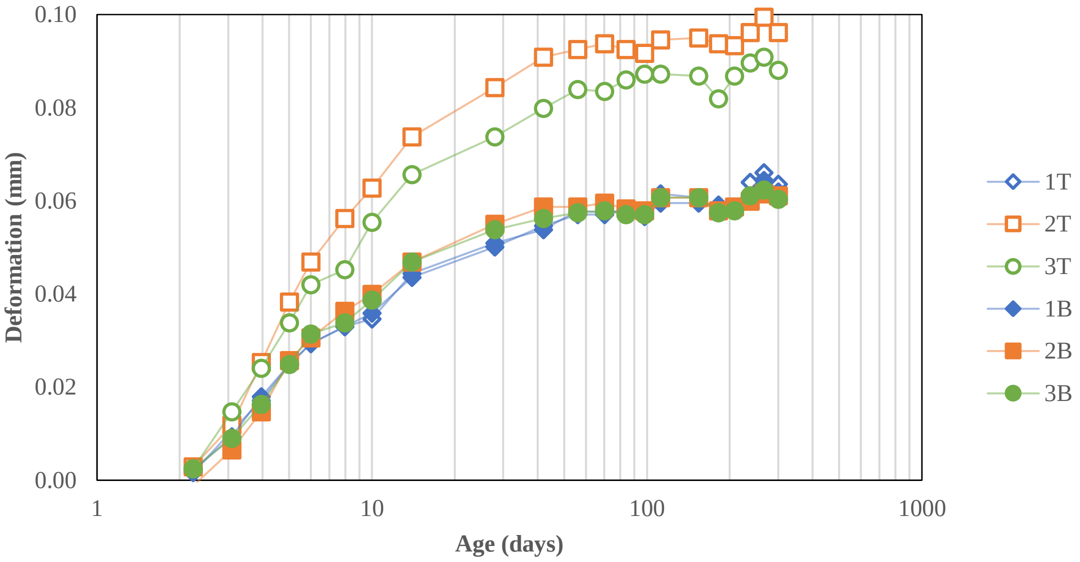

Figure 2.7 Deformation at the boundary between restraining frame and concrete specimens, mix M20R10P1.

A numerical investigation was conducted by Younis (2014) using 3D linear FEA models in ABAQUS (ABAQUS, 2014) to estimate the induced deformations by concrete drying shrinkage on the restraining frame. Solid (continuum) elements with 8 integration points (CD8R) were used. The approximate global mesh size was 20 mm, but a finer mesh was adopted close to the connections. The model was run without the presence of concrete elements and pre-stressing forces on the rods inside the square hollow sections (SHS). This study adopted this model, but modified the boundary conditions, modelling of concrete prisms and pre-stressed forces as follows; the right column (CS) was fixed (welded) to the SHSs and to the base of the frame whilst the left CS was pinned by pre-stressed forces of

56.25 kN (the result of a torque of 180 N.m on the bolts) applied to rods inside the SHS. The anticipated induced force due to drying shrinkage ($\varepsilon_{sh}E_cA_c$), at the age of 300 days, was applied uniformly on the anchors. More detailed calculations are presented in Appendix A.

Figure 2.8 shows the exaggerated global and local deformations of the restraining frame obtained by FEA. Concrete shrinkage caused relative translation of the CS and bending in both CS and SHS. The relative translation between the columns at the level of prism 1, 2 and 3 is 0.127, 0.075 and 0.087 mm, respectively, corresponding to RF of 0.64, 0.79 and 0.75. The bending deformation of the SHS restraining prism 1 is higher than that at prisms 2 and 3 due to the free end effect. Prism 2 experienced the lowest deformations due to the restraint contribution of both top and bottom SHSs. Figure 2.8b shows the local deformation of the CS at the level of prism 2 and the relative deformation between web and flanges. This highlights the additional contribution to the boundary zone deformation due to local deformations of the frame, which can actually account for some of the deformation shown in Figure 2.7. Much of this local deformation can be avoided if the CS is locally stiffened to prevent the flange rotation. The average apparent measured RF at 300 days was 0.57 whilst the theoretical and numerical RFs are very similar at 0.73.

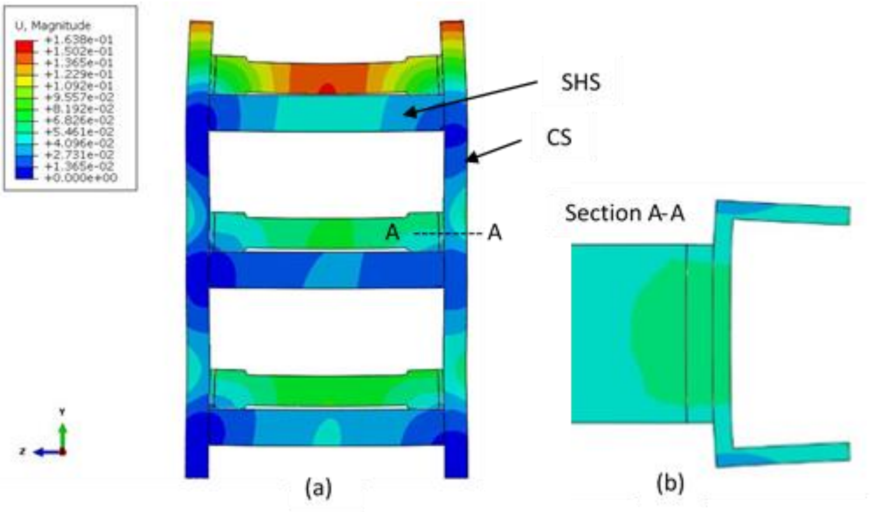

Figure 2.8 Exaggerated global and local deformation in the restraining frame (a) and supporting column (b).

2.4 Results and Discussion on Mechanical Characteristics

2.4.1 Compressive strength

Table 2.3 shows the average results of density and compressive strength for the plain concrete mixes, for both air and water cured cubes (standard deviations are shown in parenthesis). For air cured cubes, there was only a slight increase in the compressive strength between 7 and 28 days whereas for water cured specimens, there was a dramatic change in compressive strength due to the activation of the GGBS in the presence of water. The GGBS is also responsible for the lower early strength of the water cured samples at 7 days (Aly & Sanjayan, 2008; Clear, 2011). At 14 months, the compressive strength for the samples stored in air is similar to that measured at 28 days, while there was an increase from 40 MPa to 56 MPa for the water cured samples.

Table 2.3 Plain concrete density and compressive strength results (standard deviation).

Curing method	**Density (kg/m^3)**			**Compressive Strength (MPa)**		
	7 days	**28 days**	**14 months**	**7 days**	**28 days**	**14 months**
Air cured	2310 (34)	2285 (11)	2284 (42)	20.7 (0.2)	24.5 (1.6)	24.1 (0.3)
Water Cured	2387 (11)	2415 (16)	2405 (29)	22.6 (0.6)	40.1 (0.2)	56.0 (1.2)

Figure 2.9 shows the mean compressive strength values, obtained from three cubes (150 mm) per mix at 35 and 105 days (moisture cured in the laboratory) as well as from six samples for each curing condition (MR, CR, RS) obtained from the broken prisms in flexure at the age of 14 months. At age of 14 months, SFRC obtained from broken prisms shows higher compressive strength compared to plain concrete at the same curing condition. However, in all cases, the dose of the steel fibres appears to have no clear effect on compressive strength.

As expected, prisms stored in the mist room (MR) show much higher compressive strength compared to the ones air cured in the control room (CR and RS). CR and RS samples, resulted in similar compressive strengths despite the fact that RS samples were restrained for ten months and experienced drying shrinkage micro-cracks. This may be because CR samples were fully dried in an oven (to determine mass loss) which may have caused micro-cracks and weakened its structure.

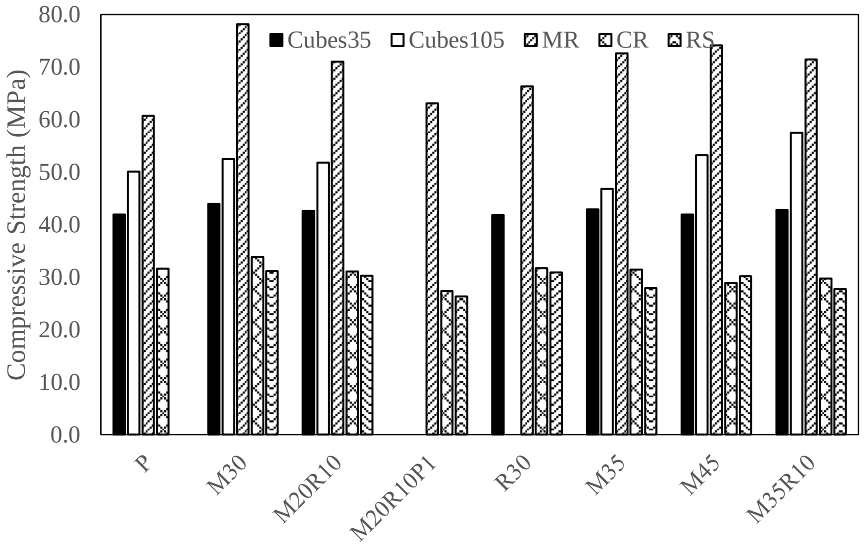

Figure 2.9 Compressive strength obtained from cubes at 35 and 105 days and broken prisms in flexure at 14 months.

2.4.2 Flexural Performance

Figure 2.10 (a-f) shows the stress-CMOD results (average of three prisms) for specimens conditioned in MR, CR and RS environments. The initial elastic behaviour of all specimens, shown in the graphs up to CMOD of 0.2 mm, is very similar. This confirms that the test arrangement and measuring method is accurate and reliable and that the fibre content does not influence much the elastic modulus. The plain concrete mix (P) shows the lowest strength and least overall toughness. The fibre content seems to have some influences on strength with some mixes (e.g. CR M35) showing up to 100% increase in strength and clear strain hardening characteristics, which was most likely a result of fibre alignment. The initiation of cracking in the plain concrete appears to take place just before the peak load at a CMOD of 0.02 mm. The same applies to all other specimens and, as expected, fibres get mobilised and control the crack development. In several cases, there is some initial drop in stress after the opening of the crack at around 0.03 mm until the fibres are mobilised sufficiently and contribute to stiffening the cracked concrete. Sudden drops in stress are also seen in the post-peak range, due to fibre fracture or slip.

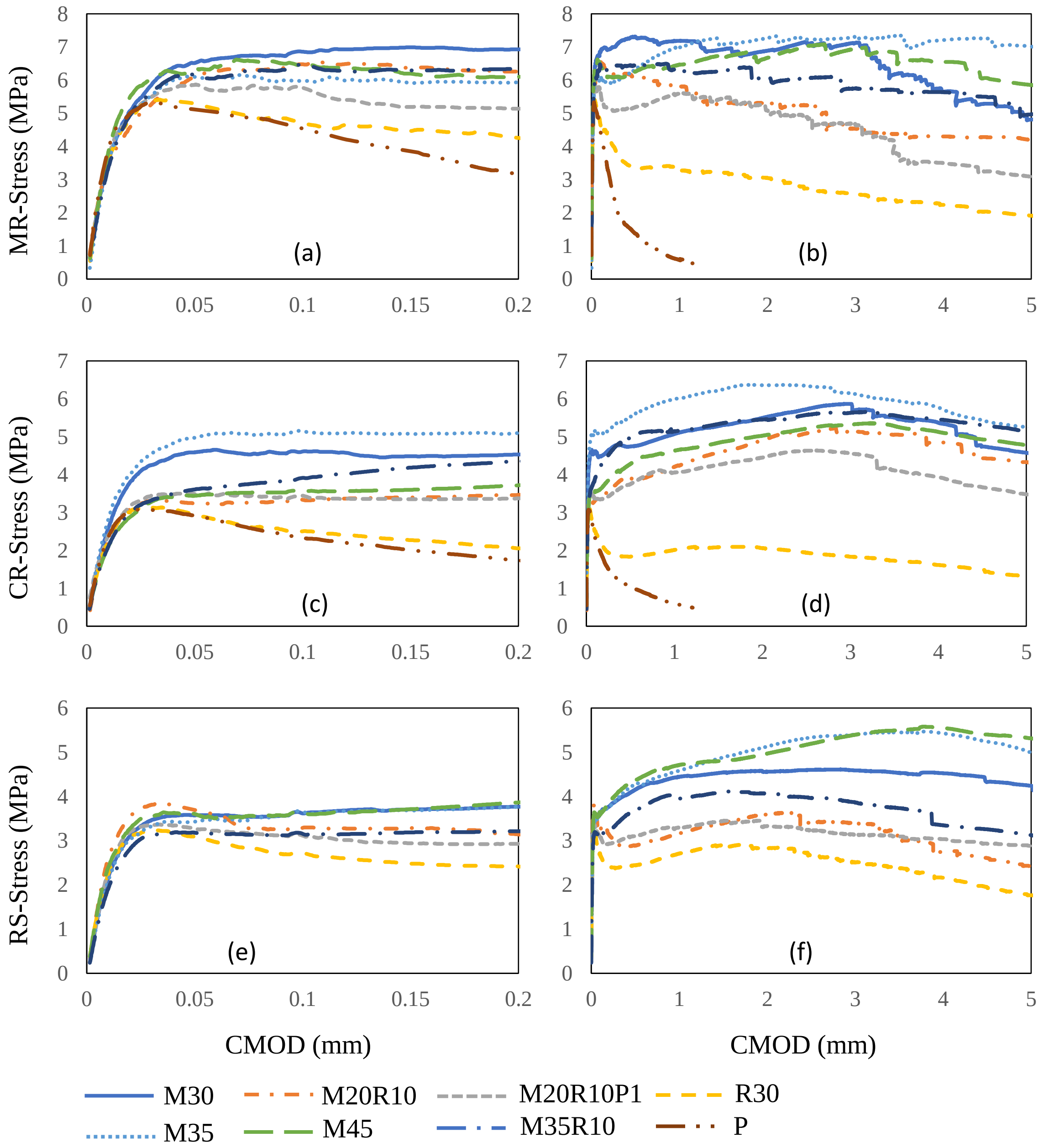

Figure 2.10 Stress-CMOD curves a) MR-0.2 mm, b) MR, c) CR-0.2 mm, d) CR e) RS-0.2 mm, f) RS.

All prisms conditioned in the mist room (MR) show higher strength and toughness than the CR specimens. This highlights the importance of curing in strength development as well as the dominance of concrete strength on the flexural strength of SFRC. Higher concrete strength also results in higher bond strength between the concrete and fibres, which contributes to higher toughness. However, this also leads to more fibres fracturing during the post-peak stage than slipping, as indicated by the fracturing sounds during the test. In the case of the MR conditioned specimens (see Figure 2.10b), the higher concrete strength leads to a high flexural strength when the first crack develops, but due to high bond, more fibres break, leading to mainly flat post-cracking behaviour. On the other hand, CR and RS conditioned specimens, which have a lower concrete strength, show a lower flexural strength at first crack, but mobilize more fibres due to slippage, which leads to smoother curves with hardening behaviour (Fantilli, et al., 2009; Wille, et al., 2014).

2.4.3 Residual flexural tensile strength

This sub-section examines the effect of fibre type and dosage, curing and restrain condition on the flexural strength at the limit of proportionality (f_{LOP}) and residual flexural tensile strength values (f_{R1}, f_{R2}, f_{R3}, f_{R4}) at different CMODs (0.5 mm, 1.5 mm, 2.5 mm and 3.5 mm). In accordance to EN 14651:2005, f_{LOP} is taken as the maximum stress value up to CMOD of 0.05 mm.

2.4.3.1 Effect of curing

Figure 2.11 (a and b) shows the change in flexural strength and residual values for the specimens subjected to different conditions (MR and RS) relative to the CR condition. Figure 2.11a shows that mist curing increases f_{LOP} by up to 90% (on average 60%), but this increase decreases at larger CMODs. This confirms that curing has a significant effect on concrete strength development as reflected by the increase in f_{LOP}. However, as the effect on f_R values reduces with increasing CMOD, curing condition has less impact on the bridging capacity of fibres which, at large CMOD, depends more on frictional stresses, geometrical characteristics and less on bond strength. At ultimate CMOD, the increase in f_{R4} values was only by 10% on average, which indicates that the stress is mostly dependent on fibre characteristics.

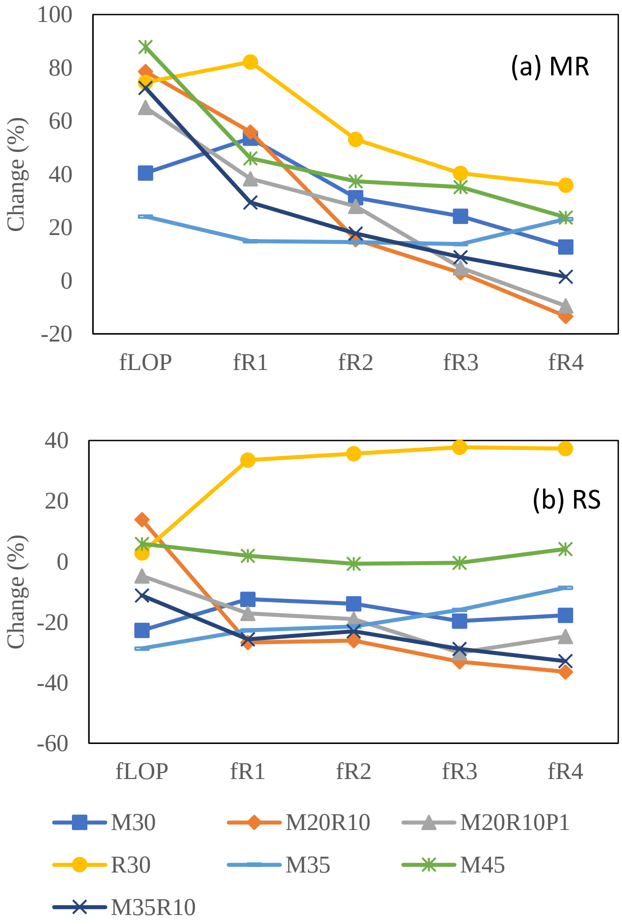

Figure 2.11 Change in flexural and residual flexural tensile strength relative to CR in a) MR and b) RS.

2.4.3.2 Effect of restraint

Figure 2.11b shows the relative change in flexural strength due to restraint. The figure shows an overall loss of f_{LOP} on average of 10% due to restraint, despite the fact that no cracks were visible on the RS specimens. However, as tensile strain and stress developed in the RS specimens, micro-cracking must have taken place and caused some damage to the concrete. The effect of the damage and micro-cracks appears to overall increase marginally as the CMOD increases. Specimens manufactured with mix R30 show better performance partly because they were not well restrained, thus they could suffer less damage.

2.4.3.3 *Effect of fibres*

Figure 2.12 (a-c) shows the change in flexural strength and residual flexural tensile stresses due to the substitution of MUSF with RTSF for a total fibre content of 30 kg/m^3 under MR, CR and RS conditions, respectively. The changes are shown relative to M30 for each respective condition. In Figure 2.12a, the effect of substituting MUSF with 10 kg/m^3 of RTSF results in about 25% reduction in both f_{LOP} and residual flexural tensile stresses, as this substitution did not affect much the concrete tensile strength and concrete-fibre interface bond strength. In larger specimens (150 mm prisms and slabs), the blends with 10 kg/m^3 RTSF showed a positive change in f_{LOP} and f_R values (Hu, et al., 2018). This can be attributed to the fact that fibre alignment is more critical in cast elements with small cross section due to boundary effect, thus a small reduction in the amount of MUSF (which is longer) can affect significantly the post cracking behaviour. The highest strength reduction at bigger CMODs was observed in specimens made with mix R30, partly due to fibre slippage as RTSF have shorter and thinner geometries compared to MUSF and partly due to their more random distribution. The reduction in f_{LOP} for specimens conditioned in CR (Figure 2.12b) is higher than that found in MR samples by about 20%, but this may have more to do with the high f_{LOP} values of M30 than the effect of fibres, as the f_R values changes are similar to those observed for MR samples (Figure 2.12a). The difference in f_R values of mixes M20R10P1 and M20R10 possibly not related to the addition of 1 kg/m^3 of RTPF, but most likely as they were cast from different batches.

When the concrete is restrained (see Figure 2.12c), even though there is an overall drop in f_{LOP} of 10%, the fibres do not appear to influence f_{LOP}. However, there is a drop of about 30% in the f_R values of the blended mixes and of about 40% for the R30 mix.

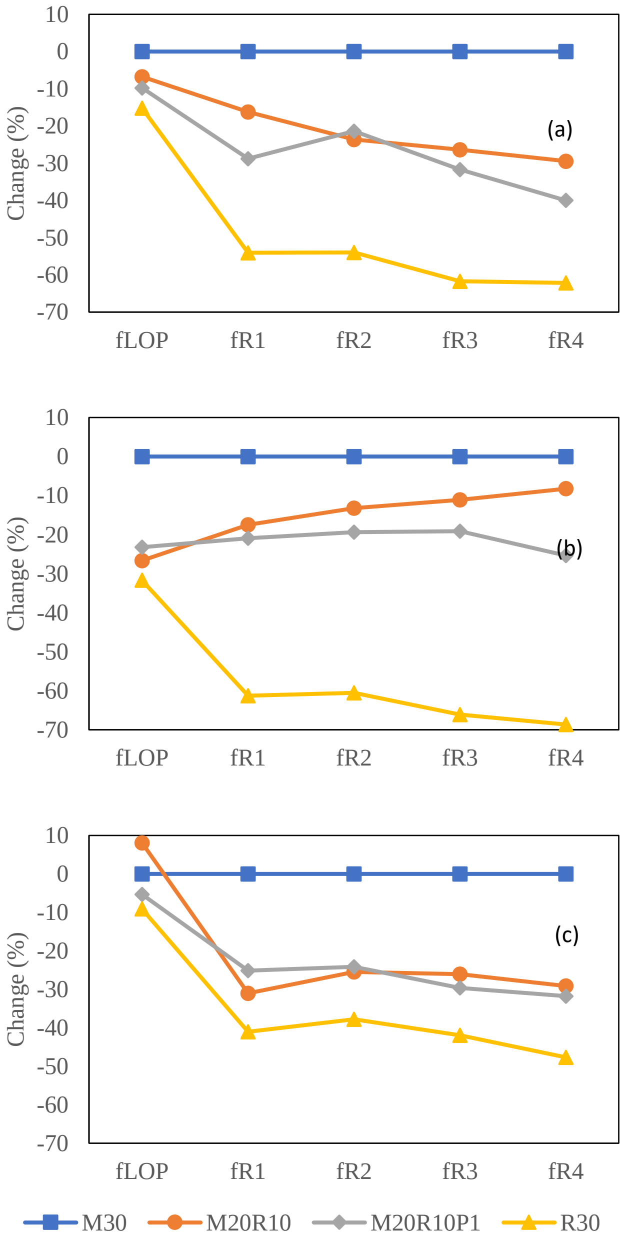

Figure 2.12 Change in residual flexural tensile strength due to substitution of MUSF with RTSF conditioned in a) MR, b) CR and c) RS.

2.4.4 Characteristic residual flexural tensile strength ratios

In order to replace parts of conventional reinforcement with fibres in concrete structures, *fib* MC-2010 imposes that the minimum values of characteristic residual flexural tensile strength ratios at serviceability (f_{R1k}/f_{Lk}) and ultimate limit state (f_{R3k}/f_{R1k}) conditions, be 0.4 and 0.5, respectively (f_{Lk}, f_{R1k} and f_{R3k} are the characteristic values at f_{LOP}, f_{R1} and f_{R3}, respectively). These characteristic values are calculated using RILEM TC 162-TDF (2003) and depend on the number of specimens tested per parameter.

Figure 2.13 shows the serviceability characteristic residual flexural tensile strength ratios (f_{R1k}/f_{Lk}) for all mixes in MR, CR and RS conditions. Mixes with a total of 30 kg/m^3 of steel fibres show ratios less than one, while mixes with a total of 45 kg/m^3 show ratios mostly greater than one. Mixes with 45 kg/m^3 contain considerably more longer manufactured fibres which have a larger diameter and can resist tension more effectively even at larger CMOD. CR and RS specimens with a total fibre content more than 35 kg/m^3 have higher ratios than MR specimens, due to their lower f_{LOP}.

Figure 2.14 shows the ultimate characteristic residual flexural tensile strength ratios (f_{R3k}/f_{R1k}) for all specimens subjected to MR, CR and RS conditions. Most of f_{R3k}/f_{R1k} ratios for the CR and RS specimens are greater than those for MR samples. This can again be attributed to the higher f_{LOP} achieved in the MR samples as a result of better curing. Overall, all blends satisfied the required ratios of *fib* MC-2010 for serviceability and ultimate limit states. Hence, blends of MUSF and RTSF can be used to replace part of conventional reinforcement in RC structures.

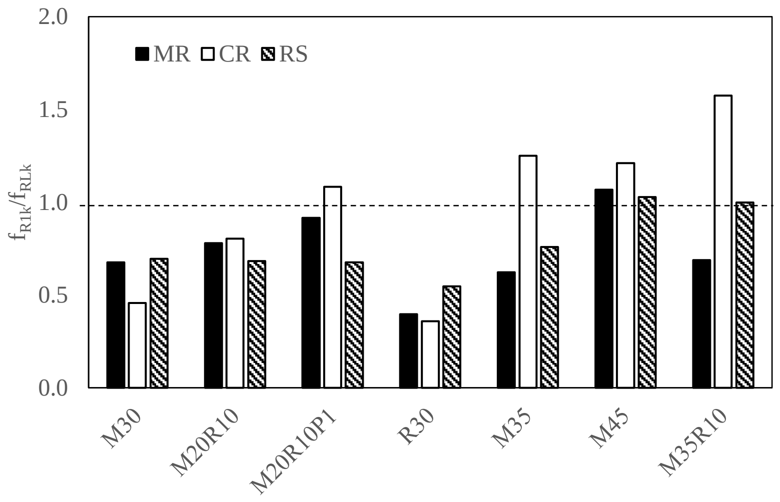

Figure 2.13 Ratio of characteristic strength, f_{R1k}/f_{Lk}.

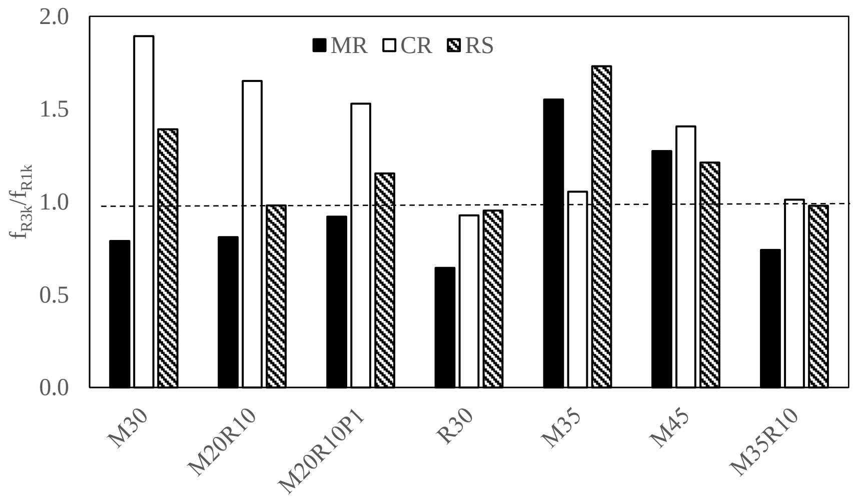

Figure 2.14 Ratio of residual characteristic strength, f_{R3k}/f_{R1k}.

2.5 Conclusions

This paper presented the effect of fibre type (MUSF, RTSF and various blends) on free and restrained shrinkage of FRC specimens and their associated mechanical characteristics. It has been shown that the utilisation of GGBS and RTSF in concrete mixes contributes in maintaining the long-term health of the examined specimens by reducing the shrinkage strains and mitigate cracking of restrained SFRC. Based on the experimental results the following conclusions can be drawn:

- Free shrinkage was much lower than predicted by the design codes due to the use of GGBS (35% on average), which sealed pore holes and delayed water evaporation.
- Non-uniform shrinkage strains through the height of plain and SFRC sections were observed in free and restrained elements, possibly due to uneven distribution of coarse aggregates.
- Average shrinkage strains in SFRC were higher than in plain concrete (by about 38% on average), possibly due to an increase in air voids.
- Drying and end restraint caused the development of micro-cracking in the concrete which resulted in lower compressive strength (by about 56% on average) and residual flexural tensile strength (up to 40%).
- Curing has a significant effect on concrete strength development (56% on average), but less impact on the bridging capacity of fibres which depends more on frictional stresses.
- The high residual flexural tensile strength of SFRC (cured in MR) and the high frictional stresses between the concrete and the fibres caused the used small dosages of fibres to break, due to the highly applied tensile stress on fibres.
- Based on the results of tests on small scale specimens presented in this study, the decay in the stress-CMOD curves show that the hybrid mixes of MUSF and RTSF satisfy the ratios imposed by the *fib* MC-2010 and can reduce the required amount of conventional reinforcement in concrete structures.

References

ABAQUS, 2014. *Software Documentation, Version 6.14 SIMULIA,* RI, USA: Dassault Systèmes.

ACI-231R, 2010. *Report on Early-Age Cracking: Causes, Measurement, and Mitigation,* Farmington Hills: American Concrete Institute.

Akcay, B. & Tasdemir, M. A., 2012. Mechanical behaviour and fibre dispersion of hybrid steel fibre reinforced self-compacting concrete. *Construction and Building Materials,* Volume 28, p. 287–293.

Al-Kamyani, Z., Guadagnini, M. & Pilakoutas, K., 2017. *Non-uniform drying shrinkage of RC elements with steel fibres.* Muscat, Whittles Publishing.

Altoubat, S. & Lange, D., 2001. Creep, shrinkage and cracking of restrained concrete at early age. *ACI Materials Journal,* 98(4), pp. 323-331.

Aly, T. & Sanjayan, J. G., 2008. Shrinkage cracking properties of slag concretes with one-day curing. *Magazine of Concrete Research,* 1(60), pp. 41-48.

Banthia, N., Yan, C. & Mindess, S., 1996. Restrained Shrinkage Cracking in Fiber Reinforced Concrete: A Novel Test Technique. *Cement and Concrete Research,* 26(1), pp. 9-14.

Bartolac, M. et al., 2016. *Punching of slabs reinforced with recycled steel fibres from used tyres.* Dundee, University of Dundee – Concrete Technology Unit.

Bazant, Z. P. & Baweja, S., 2001. *Creep and Shrinkage Prediction Model for Analysis and Design of Concrete Structures: Model B3,* Michigan: ACI.

Beddar, M., 2005. *An experimental study of porosity and premeability characteristics of steel fibre reinforced concrete.* Dundee, Institute of Civil Engineers.

Bloom, R. & Bentur, A., 1995. Free and Restrained Shrinkage of Normal and High-Strength Concretes. *ACI Materials Journal,* 92(2), pp. 211-217.

BSI-12, 1998. *Testing concrete - BS 1881 Part 119: Method for determination of compressive strength using portions of beams broken in flexure (equivalent cube method),* London: Board of BSI.

Buratti, N., Ferracuti, B. & Savoia, M., 2013. Concrete crack reduction in tunnel linings by steel fibre-reinforced concretes. *Construction and Building Materials,* Volume 44, p. 249–259.

Caggiano, A., Xargay, H., Folino, P. & Martinelli, E., 2015. Experimental and numerical characterization of the bond behavior of steel fibers recovered from waste tires embedded in cementitious matrices. *Cement & Concrete Composites,* Volume 62, p. 146–155.

Castel, A. et al., 2016. Creep and drying shrinkage of a blended slag and low calcium fly ash geopolymer Concrete. *Materials and Structures,* 49(5), p. 1619–1628.

CEN, 2008. *Eurocode 2: Design of concrete structures, Part 1-1: General rules and rules for Structures 2004,* Brussels: European Committee for Standardization.

Centonze, G., Leone, M. & Aiello, M., 2012. Steel fibers from waste tires as reinforcement in concrete: A mechanical characterization. *Construction and Building Materials,* Volume 36, pp. 46-57.

Chanvillard, G. & A'itcin, P.-C., 1996. Pull-Out Behavior of Corrugated Steel Fibres. *Advn Cem Bas Mat,* Volume 4, pp. 28-41.

Choi, H. et al., 2015. Restrained shrinkage behavior of expansive mortar at early ages. *Construction and Building Materials,* Volume 84, p. 468–476.

Clear, C. A., 2011. *Cement type/early age properties,* s.l.: Concrete Today.

Craeye, B. et al., 2010. Effect of mineral filler type on autogenous shrinkage of self-compacting concrete. *Cement and Concrete Research,* Issue 40, p. 908–913.

EN-14651, 2005. *Test methods for metallic fibred concrete - Measuring the flexural tensile strength (limit of proportionality (LOP), residual),* Brussels: European Committee for Standardization.

Fantilli, A. P., Mihashi, H. & Vallini, P., 2009. Multiple cracking and strain hardening in fiber-reinforced concrete under uniaxial tension. *Cement and Concrete Research,* Volume 39, p. 1217–1229.

fib, 2013. *fib Model Code for Concrete Structures 2010,* Berlin, Germany: Wilhelm Ernst & Sohn.

Filho, R. D. T., Ghavami, K., Sanjua´n, M. A. & England, G. L., 2005. Free, restrained and drying shrinkage of cement mortar composites reinforced with vegetable fibres. *Cement & Concrete Composites,* 27(5), pp. 537-546.

Gilbert, I., 2016. *Concrol of cracking caused by restraint to early-age deformation.* Dundee, Concrete Technology Unit, University of Dundee.

Gilbert, R. I., 2001. Shrinkage, Cracking and Deflection the Serviceability of Concrete Structures. *Electronic Journal of Structural Engineering,* Volume 1, pp. 15-37.

Graeff, Â. G., 2011. *Long-term performance of recycled steel fibre reinforced concrete for pavement applications,* Sheffield: The University of Sheffield.

Grzybowski, M. & Shah, S. P., 1990. Shrinkage Cracking of Fiber Reinforced Concrete. *ACI Materials Journal,* 87(2), pp. 138-148.

Hobbs, D. W., 1974. Influence of Aggregate Restraint on the Shrinkage of Concrete. *ACI Journal*, pp. 445-450.

Hoshino, M., 1989. Relation Between Bleeding, Coarse Aggregate, and Specimen Height of Concrete. *ACI Materials Journal,* 86(2), pp. 185-190.

Hu, H. et al., 2017. *Flexural performance of steel fibre reinforced concrete with manufactured and recycled steel fibres.* Zadar, University of Zagreb, Faculty of Civil Engineering.

Hu, H. et al., 2018. Mechanical properties of SFRC Using blended manufactured and recycled tyre steel fibres. *Construction and Building Materials,* Issue 163, pp. 376-389.

Jafarifar, N., 2012. *Shrinkage Behaviour of Steel Fibre Reinforced Concrete Pavements,* Sheffield: The University of Sheffield.

Jeong, J.-H., Park, Y.-S. & Lee, Y.-H., 2015. Variation of Shrinkage Strain within the Depth of Concrete Beams. *Materials,* pp. 7780-7794.

Jianyong, L. & Yan, Y., 2001. A study on creep and drying shrinkage of high performance concrete. *Cement and Concrete Research,* Issue 31, pp. 1203-1206.

Kaïkea, A., Achoura, D., Duplan, F. & Rizzuti, L., 2014. Effect of mineral admixtures and steel fiber volume contents on the behavior of high performance fiber reinforced concrete. *Materials and Design,* Volume 63, p. 493–499.

Leemann, A. & Lura, P., 2014. Creep and Shrinkage of SCC. In: K. Khayat & G. (. De Schutter, eds. *Mechanical Properties of Self-Compacting Concrete.* s.l.:Springer International Publishing, pp. 73-94.

Leemann, A., Lura, P. & Loser, R., 2011. Shrinkage and creep of SCC – The influence of paste volume and binder composition. *Construction and Building Materials,* 25(5), pp. 2283-2289.

Loser, R. & Leemann, A., 2009. Shrinkage and restrained shrinkage cracking of self-compacting concrete compared to conventionally vibrated concrete. *Materials and Structures,* Issue 42, pp. 71-82.

Martinelli, E., Caggiano, A. & Xargay, H., 2015. An experimental study on the post-cracking behaviour of Hybrid Industrial/Recycled Steel Fibre-Reinforced Concrete. *Construction and Building Materials,* Volume 94, p. 290–298.

Mitchell, W. & Arya, C., 2015. *The effect of combining shrinkage-reducing-admixture with ground, granulated, blast-furnace slag on the drying shrinkage of concrete,* London: UCL Department of Civil, Environmental and Geomatic Engineering.

Neville, A. M., 2004. *Properties of Concrete.* Fourth ed. London: Pearson Education Limited.

Paillere, A. M., Buil, M. & Serrano, J. J., 1989. Effect of Fiber Addition on the Autogenous Shrinkage of Silica Fume Concrete. *ACI Materials Journal,* 86(2), pp. 139-144.

RILEM-TC-107-CSP, 1998. RILEM TC 107-CSP: Creep and shrinkage prediction models: principles of their formation. *Materials and structures,* Volume 31, pp. 507-512.

RILEM-TC-162-TDF, 2003. RILEM TC 162-TDF: Test and design methods for steel fibre reinforced concrete. *Materials and Structures,* Volume 36, pp. 560-567.

Sengul, O., 2016. Mechanical behavior of concretes containing waste steel fibers recovered from scrap tires. *Construction and Building Materials,* Volume 122, pp. 649-658.

Snoeck, D., Jensen, O. & Belie, N. D., 2015. The influence of superabsorbent polymers on the autogenous shrinkage properties of cement pastes with supplementary cementitious materials. *Cement and Concrete Research,* Issue 74, pp. 59-67.

Wille, K., El-Tawil, S. & Naaman, A., 2014. Properties of strain hardening ultra high performance fiber reinforced concrete (UHP-FRC) under direct tensile loading. *Cement & Concrete Composites,* Volume 48, pp. 53-55.

Yazıcı, S., Inan, G. & Tabak, V., 2007. Effect of aspect ratio and volume fraction of steel fiber on the mechanical properties of SFRC. *Construction and Building Materials,* Volume 21, p. 1250–1253.

Yoo, D.-Y., Yoon, Y.-S. & Banthia, N., 2015. Predicting the post-cracking behavior of normal- and high-strength steel-fiber-reinforced concrete beams. *Construction and Building Materials,* Volume 93, p. 477–485.

Younis, K. H., 2014. *Restrained shrinkage behaviour of concrete with recycled materials,* Sheffield: The University of Sheffield.

Younis, K. H. & Pilakoutas, K., 2016. Assessment of Post-Restrained Shrinkage Mechanical Properties of Concrete. *ACI MATERIALS JOURNAL,* 113(3), pp. 267-276.

Zamanzadeh, Z., Lourenço, L. & Barros, J., 2015. Recycled Steel Fibre Reinforced Concrete failing in bending and in shear. *Construction and Building Materials,* Volume 85, p. 195–207.

Zdanowicz, K. & Marx, S., 2018. *Shrinkage and Expansion Strains in Self-compacting Concrete Comparison of Methods of Measurements.* Maastricht, Springer International Publishing.

Zhang, W., Hama, Y. & Na, S. H., 2015. Drying shrinkage and microstructure characteristics of mortar incorporating ground granulated blast furnace slag and shrinkage reducing admixture. *Construction and Building Materials,* Issue 93, pp. 267-277.

Chapter 3: Predicting Shrinkage Induced Curvature in Plain and Reinforced Concrete

***Al-Kamyani**, **Z.,** Guadagnini, M., Pilakoutas, K., 2018b. Predicting Shrinkage Induced Curvature in Plain and Reinforced Concrete. Engineering Structures, **Accepted for Publication**.*

Abstract

Shrinkage induced curvatures in reinforced concrete elements are thought to be affected only by section geometry and distribution/ratio of reinforcement. The variation in the level of internal restraint caused by the non-uniform distribution of concrete constituents within the section, however, can also lead to additional shrinkage induced deformations, and potentially to larger than expected deformations in critical structural elements, even under service conditions. This study examines experimentally the development of non-uniform shrinkage strains in unreinforced as well as symmetrically and asymmetrically reinforced concrete elements. Results confirm that shrinkage is non-uniform due to the variations in internal restrains (coarse aggregates and reinforcement). The addition of steel fibres mitigates this effect and reduces overall shrinkage curvature. A prediction model for shrinkage induced curvature of plain and reinforced concrete is proposed, taking into account the non-uniform distribution of concrete constituents. The proposed model yields results in good agreement with experimentally observed values of shrinkage curvature and can be used to improve the predictions of design guidelines.

This chapter consists of a "stand alone" journal paper and includes a relevant bibliography at the end of the chapter. Additional information and further test results are presented in Appendix B.

3.1 Introduction

Unaccounted deflections of reinforced concrete elements can lead to larger crack widths and vibrations, accelerate the rate of deterioration and reduce the expected life span of infrastructure (Pan, et al., 2011; Maekawa, et al., 2011). In recent years, for example, many bridges have been found to suffer from excessive deflections (Huang, et al., 2017; Tanimura, et al., 2007; Bažant, et al., 2012; Bažant, et al., 2012b). These additional deflections can be partly attributed to phenomena that are not adequately accounted for in current design equations, including: a) curvature induced by non-uniform autogenous shrinkage at early ages; b) non-uniform drying shrinkage and drying creep through the section height due to differences in sectional shape; and c) uneven quality and distribution of mix constituents.

Design codes (Eurocode 2: Part-1 2004 and *fib* Model Code 2010) provide equations to estimate global deflections through section curvature and include long-term deformations due to creep and shrinkage. Other equations predicting shrinkage curvature (Ghali & Favre, 1994; Kong & Evans, 1987; Gilbert, 2001; Groli, 2014; Forth, et al., 2014) are also based on sectional analysis and the use of an age-adjusted effective modulus. In all these equations, if the section is not cracked, the eccentricity of reinforcement from the geometrical centroid is the main source for camber (Gribniak, et al., 2007; Gilbert, 2001) and thus, no shrinkage curvature is predicted for plain concrete and symmetrically reinforced rectangular sections that do not crack.

Younis (2014) and Jeong et al. (2015) report that shrinkage strains vary through the height of plain rectangular sections, and the ratio between top and bottom shrinkage strains can be higher than two. Younis (2014) attributed strain differences to concrete bleeding and porosity, while Jeong et al. (2015) linked it to uncertainty of concrete properties and non-uniform distribution of coarse aggregates, having found that more aggregates settled in the bottom half (55%) compared to 45% in the top half of the section.

Shrinkage of cement paste in concrete is initially restrained by the adsorbed free water in the capillary pores and then by solid particles such as un-hydrated cement particles, calcium hydroxide crystals and aggregates as well as reinforcement (Hobbs, 1974; Brown, et al., 2001; Neville, 2004). However, several factors can lead to uneven evolution of shrinkage through the section height: 1) available amount of water, which is higher towards the top of the section due to bleeding and surface tamping; 2) level of restraint provided by solid particles, which is higher towards the bottom where more particles settle (Jeong, et al., 2015); 3) differential loss of water particles from the cement matrix into the surrounding environment, due to variable porosity and permeability which is normally higher at the top (Beddar, 2005); 4) variation of concrete mechanical properties through the depth of the section (Hoshino, 1989), such as compressive strength, density and elastic modulus, which are affected by water-to-binder ratio, vibration and tamping of fresh concrete.

Restrained shrinkage strains can lead to cracking in large structures, hence, special/ additional reinforcement is normally provided near the surface of a section to control cracks. In some applications (e.g. dams, tunnels, and slabs-on-grade), steel fibres are used on their own or with conventional reinforcement for crack control. Recently, recycled tyre steel fibres (RTSF) have also been examined and are being used in construction (Groli & Caldentey, 2017; Martinelli, et al., 2015; Bartolac, et al., 2016). The addition of fibres in concrete requires the use of a more workable concrete, which is normally achieved by using higher water-to-binder ratios or additional admixtures. This often leads to an increase in the amount of entrained air by two means: the admixture itself, which acts as an air entraining agent (Zdanowicz & Marx, 2018), and the large surface area of the fibres, which can trap air along the cement-fibre interface. Some researchers report increased shrinkage strains in steel fibre reinforced concrete (SFRC) compared to that of plain concrete due to the increase in air voids (Younis, 2014; Graeff, 2011), whilst others report a decrease due to the stiffness provided by the fibres, or insignificant effects (Brown, et al., 2001; Zhang, et al., 2015; Gribniak, et al., 2013). These inconsistencies point to the conclusion that the effect of steel fibres on drying shrinkage strains depends on type/dose of admixture and fibres as well as the mixing and vibration procedures. Shrinkage of concrete including RTSF has been investigated previously by Al-Kamyani et al (2018) and the contribution of RTSF to shrinkage evolution was found to be similar to that of manufactured fibres. However, a variation in shrinkage evolution at top and bottom of the section in SFRC with different types (including RTSF) and dosages of fibres has been reported by Younis (2014), who observed lower curvatures than in plain concrete.

This paper aims to investigate experimentally the effect of non-uniform drying shrinkage on sectional curvatures and additional deflections by examining the behaviour of plain concrete and SFRC elements with and without steel reinforcement. The experimental results are discussed in detail and used to develop an analytical model capable of predicting shrinkage curvatures induced by the non-uniform distribution of concrete constituents and reinforcement. The application of this model may remain limited to the elements that are designed not to crack (e.g. prestressed concrete).

3.2 Programme and Strain Measurements

The testing programme was designed to examine the effect of location and ratio of reinforcement on the distribution of shrinkage strain. Plain and steel fibre reinforced concrete elements (Figure 3.1 a-d) with symmetric and asymmetric reinforcement configurations were studied. The reinforcement bars had a diameter of 10 or 16 mm and steel fibre dosages of 20 or 30 kg/m^3 were used. The testing programme comprised eight reinforced concrete beams (150*250*2500 mm) and 36 prisms (150*150*550 mm) and the investigated parameters are summarized in Table 3.1. Six, 150 mm cubes and two cylinders with diameter of 100 mm and height of 200 mm were cast for each concrete mix to characterize their mechanical and physical properties. The specimen ID shown in Table 3.1 indicates: the type of specimen (“B” for beams with 20 mm concrete cover, “C” for beams with 40 mm concrete cover or “P” for prisms with 40 mm concrete cover); the amount of steel fibres in kg/m^3 (first two digits); and the diameter of the bars (last two digits). For example, C3010 refers to a beam with a cover to the main reinforcement of 40 mm, 30 kg/m^3 of fibres and four 10 mm bars.

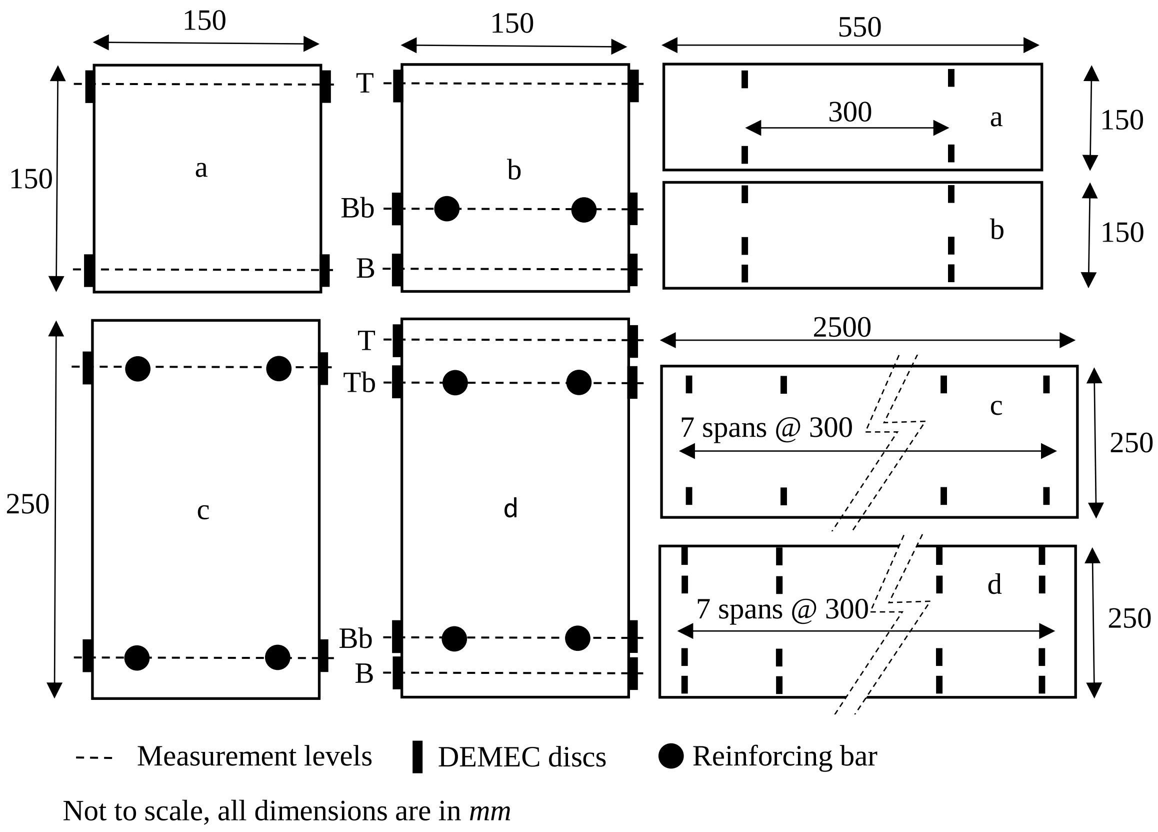

Figure 3.1 Cross section, geometry, reinforcement layout and shrinkage measurement levels of plain prism (a), RC prism (b), RC beams with concrete cover of 20 mm (c) and 40 mm (d).

All samples were covered for 7 days with saturated hessian fabric, and then kept under laboratory conditions (23±3 ˚C). To ensure equal drying from all faces, all specimens were spaced out on racks with at least 150 mm gap between them. During the 120 days of drying, temperature and relative humidity (RH) were recorded every hour and were found to be 24±4 ˚C and 54±7%, respectively. Shrinkage strains were measured at different levels of the section height and on both sides (see Figure 3.1), using a digital demountable mechanical (DEMEC) strain gauge of 300 mm span length. Shrinkage strains were measured along the central span of each prism and the entire length of each beam (over 7 spans).

Table 3.1 Test matrix and examined parameters.

Beams	**Steel fibres (kg/m^3)**	**Bar diameter (mm)**	**Concrete cover (mm)**	**Prisms**	**Steel fibres (kg/m^3)**	**Bar diameter (mm)**	**Concrete cover (mm)**
-				**P0000**	-	-	-
B0010	-	10	20	**P0010**	-	10	40
B0016	-	16	20	**P0016**	-	16	40
-				**P2000**	20	-	-
B2010	20	10	20	**P2010**	20	10	40
B2016	20	16	20	**P2016**	20	16	40
-				**P3000**	30	-	-
B3010	30	10	20	**P3010**	30	10	40
B3016	30	16	20	**P3016**	30	16	40
C3010	30	10	40	**-**			
C3016	30	16	40	**-**			

Steel fibre: total amount of added fibre including MUSF and RTSF with 50% each type.

3.3 Material Characterization

3.3.1 Concrete and reinforcement

The ready-mix concrete composition (provided by a third-party ready-mix supplier) is shown in Table 3.2. The mixes are from the same batch and are shown in the order of casting. A retarder (Rheomix 500R) was used to extend the workable life of the concrete and allow time for the integration of the steel fibres. Superplasticiser (MasterPolyheed 410) was added to the concrete to maintain a slump of around 100 mm in all mixes. The beams were vibrated using a poker vibrator, while the prisms were vibrated on a shaking table for about 20 seconds.

Table 3.2 Concrete mix composition.

Composition	**Unit**	**With 20 kg/m^3**	**With 30 kg/m^3**	**Without fibres**
Cem I 52.5R	kg/m^3	310	310	310
Graded Gravel 4/20	kg/m^3	947	947	947
Sand 0/4	kg/m^3	947	947	947
Retarder (Rheomix 500R)	Lt/m^3	1.2	1.2	1.2
Superplasticiser (MasterPolyheed 410)	Lt/m^3	0.5	1.5	1.5
w/c	-	0.6	0.6	0.6

Standard bars were used for flexural reinforcement. The Elastic modulus of the 10-mm bars was found from steel coupons to be 207 GPa and for the 16-mm bars 194 GPa. Two types of steel fibre (50% of each type) were used in a hybrid combination: manufactured undulated steel fibres (MUSF) with a length/diameter of 55/0.8 and nominal strength of 1450 MPa; and classified recycled steel fibres from waste tyres (RTSF) with an average length/diameter of around 20/0.15 and nominal strength of 2000 MPa.

3.3.2 Compressive strength of cubes

The average compressive strength and density were determined from tests on six cubes per mix at the age of 28 days and are summarized in Table 3.3. Mix P2000 had higher density and compressive strength than plain concrete while mix P3000 had the lowest density and compressive strength. The compressive strength was affected by the amount of fibres and relative amount of entrained air as evidenced by the loss in bulk densities.

Table 3.3 Density, porosity and compressive strength of plain and SFRC.

Mix	**Cubes**		**Cylinders**					
	Bulk Density (g/cm^3)	Strength (MPa)	Dry Density (g/cm^3)		Saturated Density (g/cm^3)		Porosity (%)	
			Top	Bottom	Top	Bottom	Top	Bottom
P0000	2.335	50.0	2.284	2.320	2.410	2.431	12.6	11.2
P2000	2.353	52.9	2.306	2.332	2.429	2.445	12.4	11.3
P3000	2.264	40.6	2.264	2.259	2.406	2.399	14.3	14.0

3.3.3 Porosity and Density

The porosity of the plain concrete and SFRC was obtained by testing two cylinders from each mix, which were cut into top and bottom halves and subsequently dried at 85 ˚C for 5 days. Following the procedure described by Graeff (2011), the specimens were soaked in deionized water in a desiccator and air was pumped out from the desiccator over a time of four hours. The samples were then left in water for an additional 20 hours. The weight of the samples was measured at three stages: dried, saturated surface dry and under water. Table 3.3 shows that the porosity increases as steel fibre dosage increases, probably due to increased air entrainment. The density, both dry and saturated, was higher for the bottom half of the specimens and the ratio between top and bottom densities increase with the amount of steel fibres. Comparing the porosity at the top and bottom of the cylinders, the measured values were higher at the top due to vibration and surface tamping, which led to sedimentation of the coarse aggregates toward the bottom half and left more fibres and cement paste near the top. Overall, porosity increased with the amount of steel fibres, but the difference between top and bottom porosities decreased. This may be attributed to the fact that the fibres prevent the coarse aggregates from settling downward.

3.4 Results and Discussion

3.4.1 Aggregate distribution

The distribution of the coarse aggregates was measured and quantified through the analysis of one cross section (at 250 mm from the edge) for three prisms per mix. Each cross-section was divided into four quarters, as shown in Figure 3.2, and the area of the course aggregates (> 4 mm) within each quarter was outlined and measured. The figure shows a summary of the average values obtained for each quarter. For the plain concrete, the quantity of coarse aggregates per quarter increases from top (35.5%) to bottom (41.6%) of the section. The aggregate distribution per quarter for mix P2000 does not show any clear trend, while for mix P3000 the lowest amount of aggregates was found in Q4. The decrease in the amount of coarse aggregates in Q4 of P3000 may be partly attributed to the presence of steel fibres, which prevented the aggregates from settling at the bottom of the specimen, and partly to the boundary effect. The total percentage of coarse aggregates (T-CA) through the entire section in the plain concrete is about 39%, but surprisingly this percentage appears to decrease with increasing fibre dosage. The overall aggregate average is about 36.3%, which is in line with the expected percentage for the mix. The aggregate content variation may represent variations of aggregate output from the mixer, with more coarse aggregate being found in the last batch.

The centroid (gravity centre) of the coarse aggregate (referred to as G-CA in Figure 3.2) was located at about 47.2% of the section height for the plain concrete and this ratio increased with increasing steel fibre dosage. Mix P3000 had G-CA higher than 50%, which means that the coarse aggregates were more concentrated in the upper half.

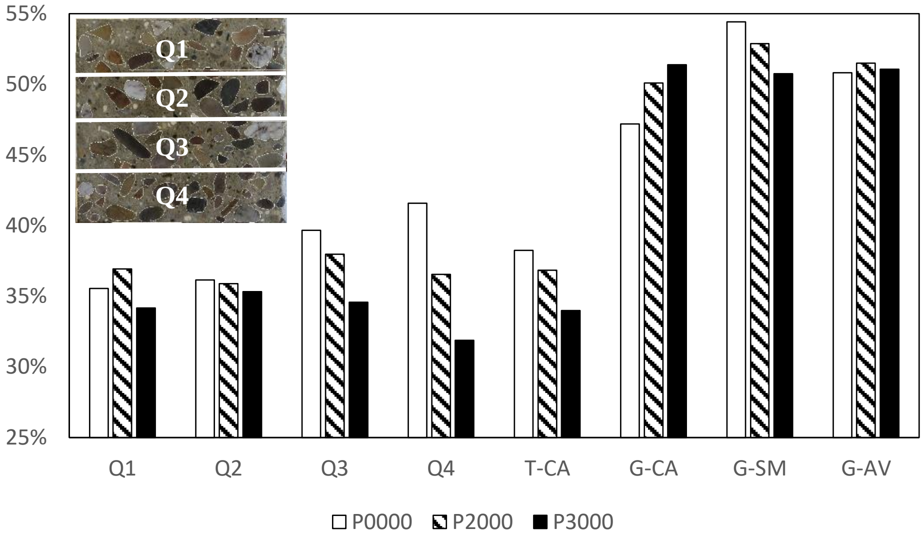

Figure 3.2 Distribution of coarse aggregates and shrinkage strains.

Coarse aggregates reduce shrinkage strain by offering more restraint due to their higher stiffness than the cement paste and, at the same time, by displacing the cement paste, which contains more water. Variations in stiffness and shrinkage potential would result in variations in shrinkage strains across the depth of the section. Hence, a higher amount of coarse aggregate in the lower half of the section causes higher restraint and thus smaller shrinkage strains.

Since shrinkage strains at the top are higher than at the bottom of the section, the resultant centroid (or shrinkage moment) of the equivalent top and bottom shrinkage strains (G-SM) is located above the geometrical centroid. Figure 3.2 shows that G-SM for plain concrete was located at about 54% of the section height and moved towards the geometrical centroid with increasing steel fibre dosage. Interestingly, the average (G-AV) of G-CA and G-SM is just above 50% with small variability between the three mixes.

It should be noted that shrinkage distribution is affected by other parameters such as permeability, volume and distribution of sand particles and crystals of hydrated cement, etc. Permeability and porosity, which are higher at the top of the section, enable storage of higher amounts of water and increase the speed of water particle migration, thus resulting in higher drying shrinkage. In this experimental study, porosity was found to be generally higher in the top half of the specimens and its values increased with increasing steel fibre dosage, due to the higher volume of entrained air.

3.4.2 Shrinkage strains

3.4.2.1 Plain concrete and SFRC

Figure 3.3 shows average shrinkage strains at the top (T) and bottom (B) of plain and SFRC, taken on both sides of three prisms per mix. Shrinkage strains at the top of the section are generally higher than at the bottom for all mixes, especially in the first 60 days, due to bleeding and un-even distribution of concrete constituents. Plain concrete experienced the highest shrinkage of all mixes at the top and the lowest at the bottom, most likely due to the higher sedimentation of aggregates, while the difference between top and bottom strains decreased by increasing the dosage of steel fibres, possibly because fibres prevented the coarse aggregates from settling. Mix P2000 experienced the lowest shrinkage strains at the top, possibly due to its higher compressive strength. Hence, shrinkage is affected by the presence of steel fibres as well as other factors such as compressive strength, w/c ratio, amount of entrained air and distribution of aggregates/paste. The average shrinkage strains for plain and SFRC are similar and are in good agreement with those predicted according to *fib* Model Code 2010 (dashed line in Figure 3.3).

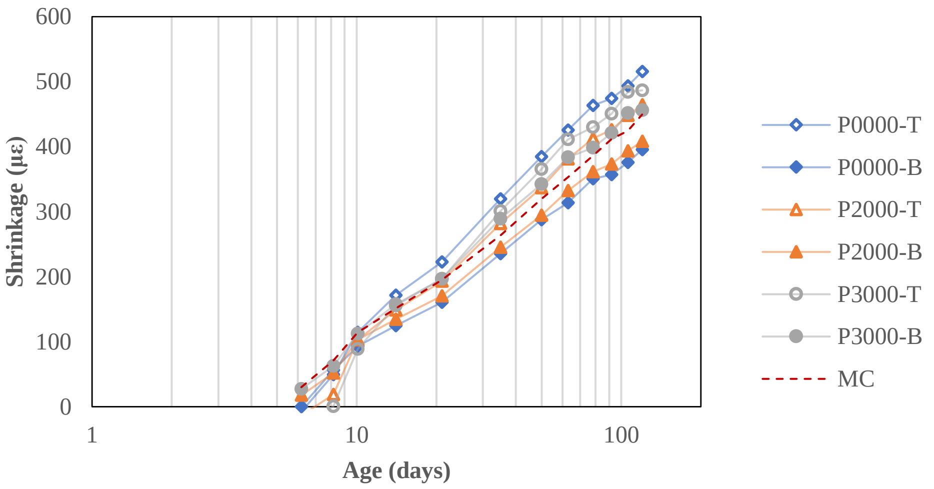

Figure 3.3 Average shrinkage strains at top and bottom of plain and SFRC prisms.

3.4.2.2 Asymmetrically reinforced prims with and without fibres

Figure 3.4 and Figure 3.5 show the average shrinkage strains measured on three RC prisms reinforced with 10-mm and 16-mm bars, respectively, at three levels: top level (T); reinforcement level (bottom-bar: Bb); and bottom level (B) (see Figure 3.2b). Shrinkage strains at the top level for all mixes with reinforcement (10-mm and 16-mm) are similar to those in plain concrete shown in Figure 3.3, whilst shrinkage strains at the bottom were controlled by the presence of reinforcement and the slightly higher amounts of coarse aggregates. The larger ratios of conventional reinforcement resulted in higher levels of restraint. However, measurements indicate that the effectiveness of the reinforcement in restraining shrinkage is limited to a certain ‘effective distance’ from the bars (or ‘effective area’). The shrinkage strains at the top of the prisms with 20 kg/m^3 of steel fibres were lower than those measured in plain concrete and prisms with 30 kg/m^3 of steel fibres, possibly due to their higher compressive strength. The average value of top and bottom shrinkage strains is approximated well by Equation (3.1), derived by considering equilibrium of forces (Gribniak, et al., 2007; Gribniak, et al., 2013; Groli, 2014).

$$\varepsilon_{cs,RC} = \frac{\varepsilon_{cs}}{1 + \alpha_e \rho_s} \qquad (3.1)$$

where ε_{cs} is the free shrinkage strain, $\varepsilon_{cs,RC}$ is the shrinkage strain in reinforced concrete, α_e is the log-term effective modular ratio and ρ_s is the ratio of reinforcement. The creep coefficient (φ) used to obtain α_e was calculated based on MC-2010 provision. At 120 days, φ was 1.78 and the aging factor (χ) was assumed to be 1.0. The analytical predictions are shown by the dashed lines in Figure 3.4 and Figure 3.5 for the prisms reinforced with 10-mm and 16-mm diameter bars, respectively.

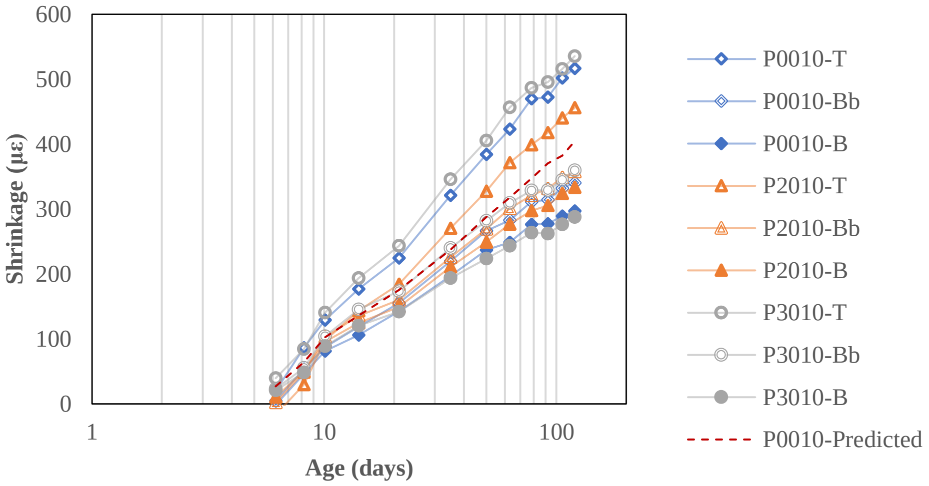

Figure 3.4 Average shrinkage strains at different levels of RC prisms with 10-mm bars with and without steel fibres.

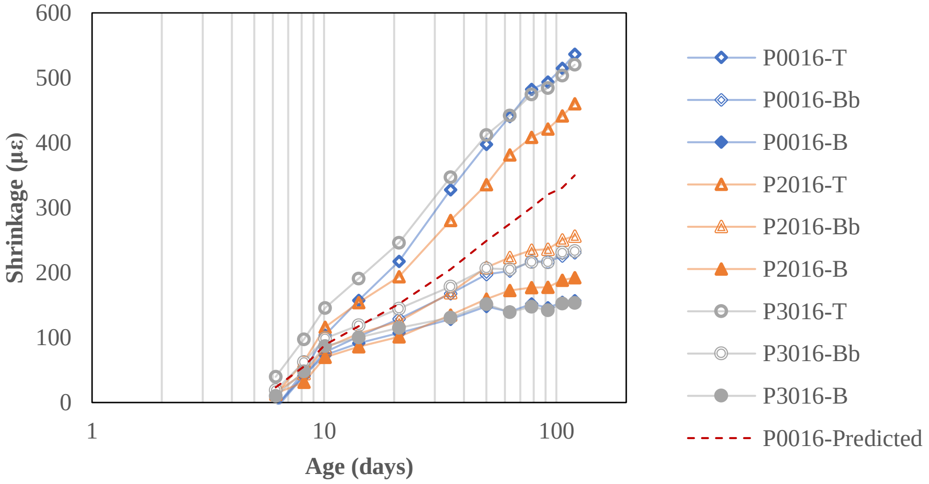

Figure 3.5 Average shrinkage strains at different levels of RC prisms with 16-mm bars with and without steel fibres.

3.4.2.3 Symmetrically reinforced beams with and without fibres

Figure 3.6 shows the average shrinkage strains at the top (Tb) and bottom (Bb) bar levels of beams reinforced with 10 mm bars. Although the beams were symmetrically reinforced, shrinkage strains were still higher at the top level for all beams. This can be mainly attributed to the non-uniform distribution of concrete constituents (see Figure 3.2). The lower shrinkage strains measured in B2010 can be the result of the higher compressive strength of mix P2000 and the presence of steel fibres. Predicted strains using Equation (3.1) are within the range of average values.

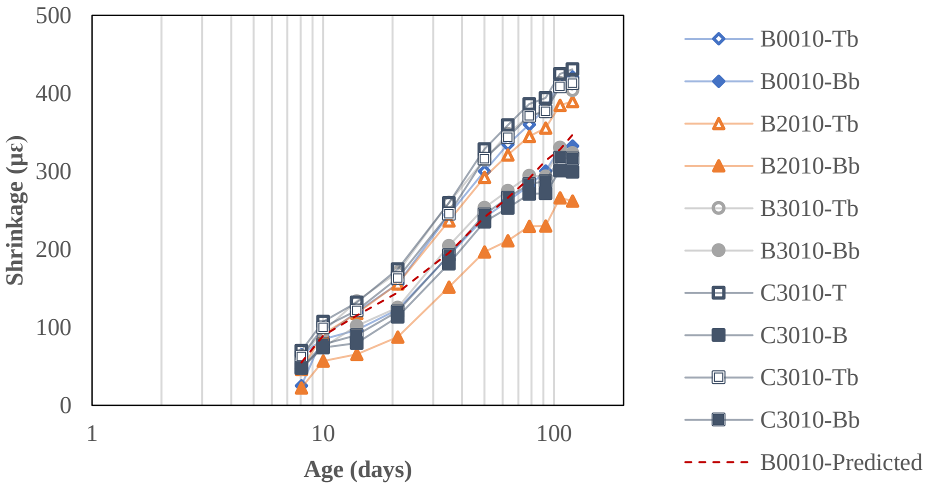

Figure 3.6 Average shrinkage strains at top and bottom of RC beams with 10-mm bars and with and without steel fibres.

Figure 3.7 shows the average shrinkage strains at the top (Tb) and bottom (Bb) levels of the beams reinforced with 16 mm bars. The higher stiffness provided by the larger steel ratios resulted in lower shrinkage strains compared to the beams reinforced with 10 mm bars. The addition of steel fibres did not seem to have a significant effect on the magnitude of shrinkage strains at both dosages of fibres. Predicted strains using Equation (3.1) are higher than average values.

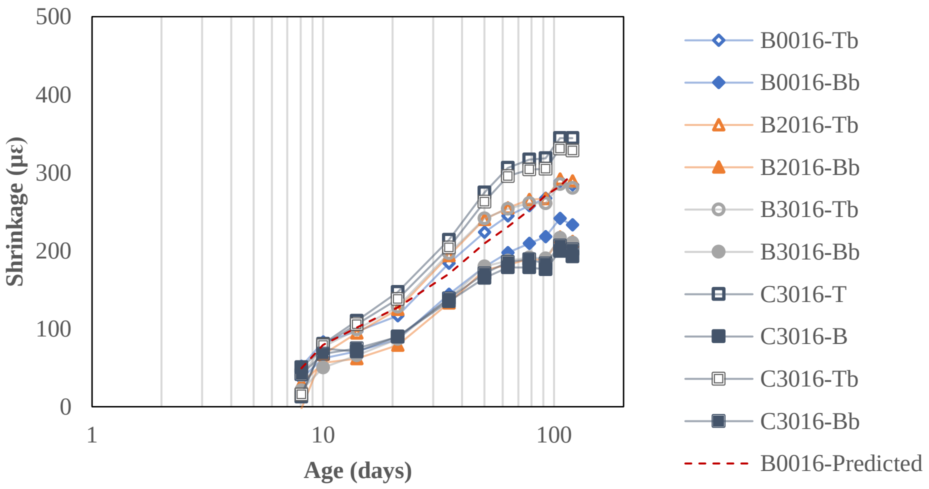

Figure 3.7 Average shrinkage strains at top and bottom of RC beams with 16-mm bars with and without steel fibres.

3.4.2.4 Reinforcement effectiveness in restraining shrinkage

Figure 3.8 shows the normalized distribution of average shrinkage strains through the cross section of prisms P3010 and P3016 and beams C3010 and C3016, as measured at the age of 120 days. It can be clearly noted that a nonlinear distribution of shrinkage strains was observed in all specimens and that the degree of nonlinearity is affected by the relative reinforcement ratio. However, the measured shrinkage strains at the top level of the prisms were similar as the effective restraint level decreased with increasing distance from the reinforcement. In addition, the shrinkage strains measured at the level of the bottom bars (Bb) in the prisms were higher than those measured in beams at the same level, possibly due to the fact that the smaller cross sections exhibited faster drying shrinkage. The strain values predicted according to Equation (3.1), shown at mid height with dashed markers in Figure 3.8, approximate well the experimental values recorded for the specimens reinforced with 10-mm bars but overestimate the strains developed in the specimens reinforced with 16-mm bars, especially beam C3016.

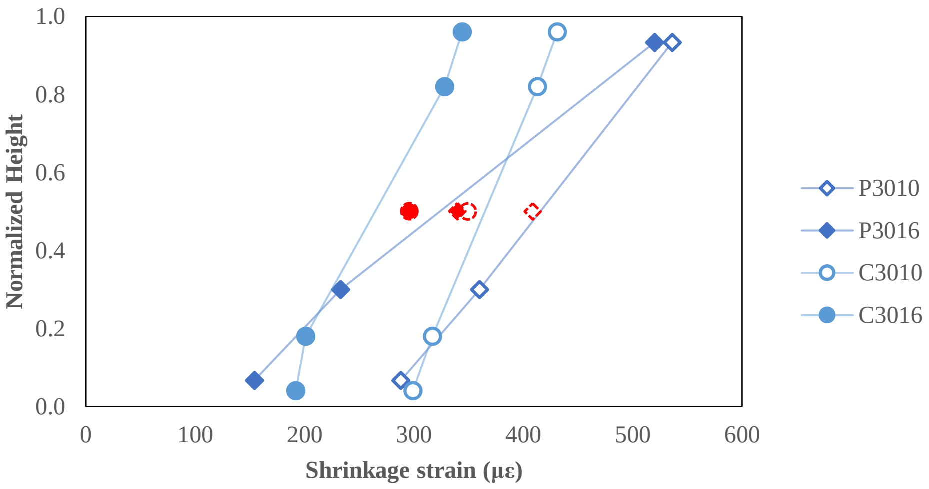

Figure 3.8 Distribution of shrinkage strains through the cross section at age of 120 days.

3.4.3 Shrinkage and mass loss

Migration of free water particles from the cement matrix is the main cause of concrete drying shrinkage and leads to a reduction in total weight and volume. The shrinkage to mass loss ratio of plain concrete has been shown to be influenced by several parameters including water-binder ratio, notional size of element, temperature and relative humidity (Younis, 2014; Aly & Sanjayan, 2008; Filho, et al., 2005). Figure 3.9 shows the relationship between the drying shrinkage and mass loss measured from the age of 7 days for the plain and SFRC elements, with and without steel bars. (It worth to mention that Figure 3.9 presents one stage of drying unlike Figure 2.4 (see Chapter 2), which has 3 stages. Figure 3.9 presents the second stage that only shows the drying shrinkage.) The relation is approximately linear for all mixes. Despite differences in porosity, mixes comprising steel fibres exhibited similar behaviour to that of plain concrete, as shrinkage is controlled mainly by permeability (Beddar, 2005). As expected, at a given mass loss, smaller shrinkage strains developed in the specimens with higher reinforcement ratio due to the higher internal restraint.

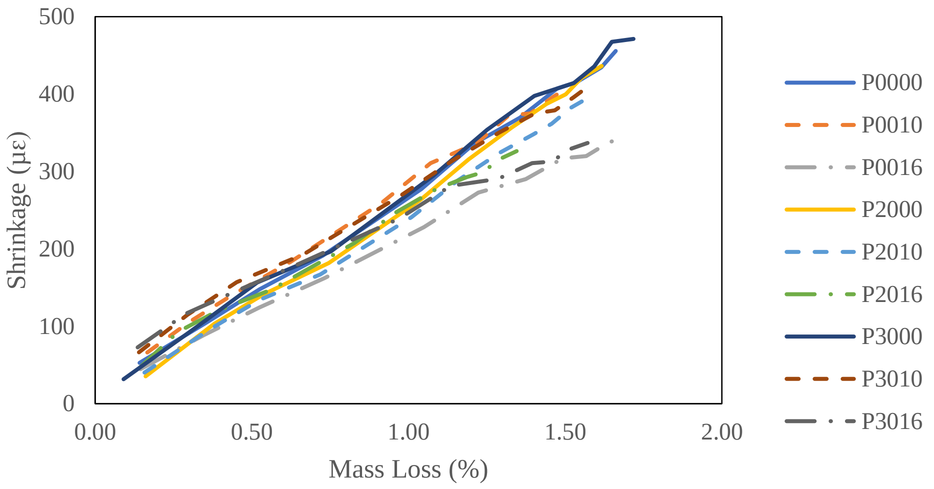

Figure 3.9 The relation between concrete drying shrinkage and mass loss.

3.4.4 Shrinkage curvature

3.4.4.1 Plain concrete and SFRC

Figure 3.10 shows curvature induced by non-uniform drying shrinkage in prisms made with plain concrete and SFRC. The experimental shrinkage curvature (k_{cs}) is calculated simply by taking the difference between the top ($\varepsilon_{cs,top}$) and bottom ($\varepsilon_{cs,bottom}$) shrinkage measurements and dividing it by the distance between them.

Plain concrete and SFRC prisms experienced some curvature induced by variations in drying and internal restraint. Specimens made of plain concrete (P0000) had higher amounts of coarse aggregates at the bottom compared to mixes P2000 and P3000 (see Figure 3.2), thus their average curvature was higher than that of specimens made of SFRC mixes. Specimens made with mix P3000 showed smaller shrinkage curvatures due to the presence of steel fibres and a more homogeneous distribution of aggregates through the section.

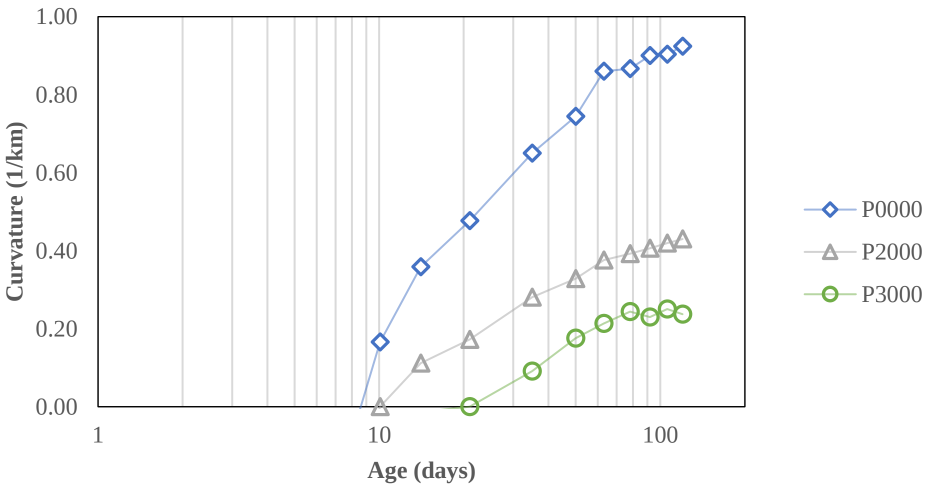

Figure 3.10 Shrinkage curvature of prisms made with plain and SFRC.

3.4.4.2 Asymmetric reinforcement distribution

Figure 3.11 shows the curvature induced by the non-uniform drying shrinkage in prisms reinforced with a single layer of bars with and without steel fibres. The prisms containing 16-mm bars exhibited the highest curvature as their larger reinforcement ratio provided higher level of restraint at the bottom of the section. The curvature of the plain concrete specimens was similar to that of specimens containing 30 kg/m^3 of steel fibre, and higher than that of specimens containing 20 kg/m^3 (P2010 and P2016) of fibres. The lower curvature experienced by the 20 kg/m^3 fibre mixes can be related to the lower shrinkage strain at the top and high compressive strength. The theoretical values of curvatures, assuming uniform shrinkage strain in the concrete section (see Equation 3.2), for prisms reinforced with 10-mm bars (P0010-Th) and 16-mm bars (P0016-Th) are also shown in Figure 3.11.

$$\frac{1}{r_{cs}} = \varepsilon_{cs}\alpha_e\left(\frac{S}{I}\right) \qquad (3.2)$$

where ε_{cs} is the concrete free drying shrinkage, α_e is the long-term effective modular ratio, S is the first moment of area of the reinforcement about the centroid and I is the second moment of the gross area. The creep efficient (φ) used to obtain α_e was calculated based on MC-2010 provision. At 120 days, φ was 1.78 and the aging factor (χ) was assumed to be 1.0.

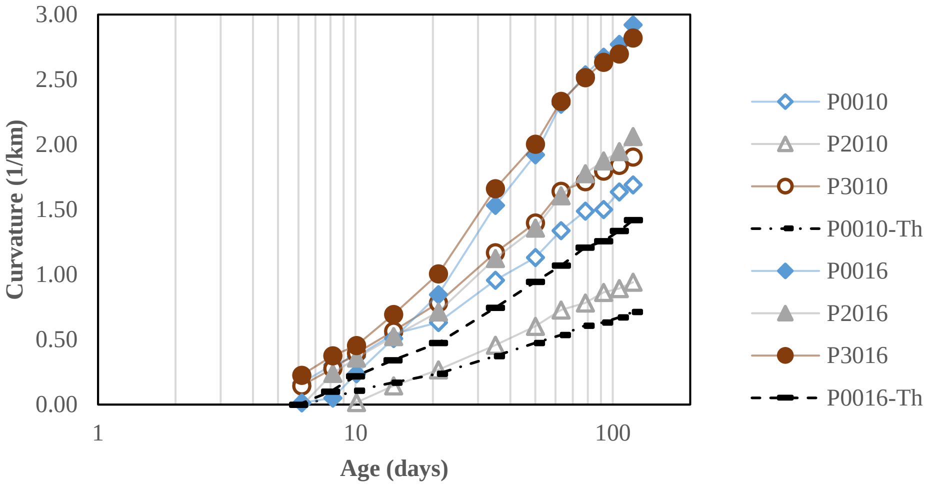

Figure 3.11 Shrinkage curvature of singly reinforced prisms with and without steel fibres.

As it can be seen, the design codes predictions are lower than the experimental values as they do not account for the presence of shrinkage induced curvature in unreinforced concrete. Given that existing codes normally assume that cracking of concrete is the main source of camber, Equation (3.2) would result in no curvature in sections made of plain concrete or symmetrically non-cracked reinforced sections.

3.4.4.3 Symmetric reinforcement distribution

Figure 3.12 shows that there is still some shrinkage curvature in symmetrically reinforced beams with and without steel fibres. In general, larger amounts of steel reinforcement provided higher levels of restraint and thus lower curvatures. The larger amount of fibre used in beams C3010 and C3016, along with the larger concrete cover (40 mm), resulted in higher overall curvatures. The development of similar curvature values for beams with different characteristics (eg. B0010, B2016, B3010) is a result of the combination of higher aggregates sedimentation in plain concrete and higher percentage of air voids in SFRC.

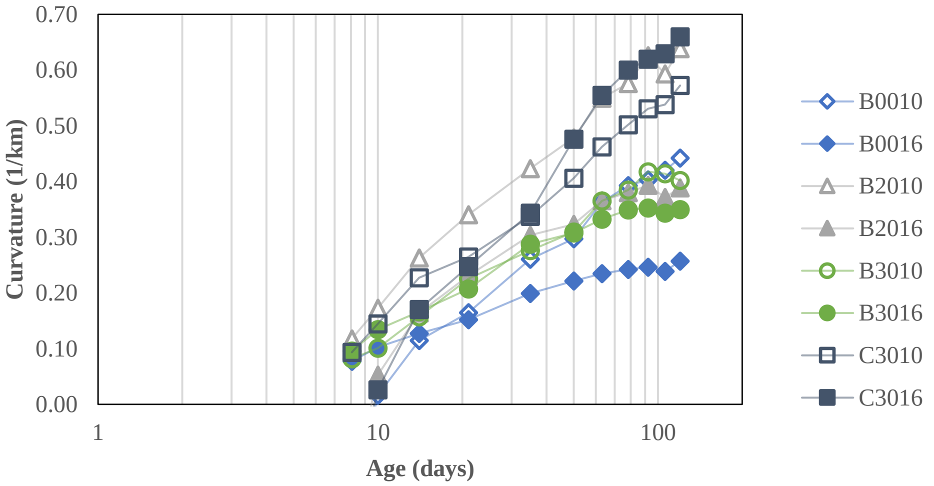

Figure 3.12 Shrinkage curvature of symmetrically reinforced beams made with and without steel fibres.

The experimental data provide evidence that significant curvature can be induced by shrinkage in both plain and symmetrically reinforced concrete specimens, mainly as a result of the non-uniform distribution of aggregates and section stiffness. Previous studies by the authors, along with the work of Younis (2014) and Jeong et al. (2015), have shown that a non-uniform distribution of shrinkage strains can develop throughout the cross section. These studies also provide evidence that the non-uniform distribution of shrinkage strain is a result of the non-uniform distribution of reinforcement, coarse aggregates and any other stiffening constituent that can offer a significant level of internal restraint. Such curvature, although relatively small, is currently neglected by design models and could lead to underestimation of deflections in larger structures such as bridge decks, slabs on-grade and concrete pavements, hence, needs to be taken into account at the design stage.

3.5 Proposed Model for Shrinkage Curvature

3.5.1 Model development

Shrinkage curvature develops when the geometrical centroid of a concrete cross section does not coincide with the centre of stiffness (i.e. asymmetric distribution of reinforcement). Equation (3.2), derived using elastic principles is widely used for the prediction of shrinkage curvature. It was initially adopted in BS 8110 (BSI, 1997) and is still used in EC-2 (CEN, 2008) and *fib* MC-2010 (fib, 2010). Using the same principles and the experimental work presented in this paper, a model is developed in the following that can account for shrinkage induced curvature due to differential concrete section stiffness.

Figure 3.13 shows a typical rectangular cross-section of a concrete beam (width: *b* and height: *h*) reinforced with asymmetrically distributed bars. The geometrical centroid of concrete (G_c) lays at mid height (*h/2*), whilst the centroid of reinforcement (G_s) can be obtained using Equation (3.3).

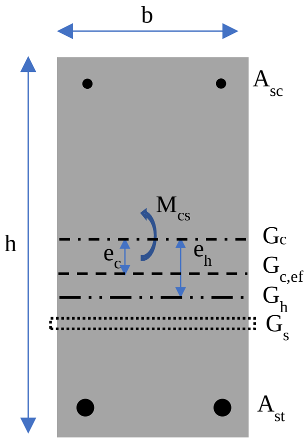

Figure 3.13 A typical cross section for a reinforced concrete element.

$$G_s = \frac{\sum A_{s,i} y_{s,i}}{\sum A_{s,i}} \qquad (3.3)$$

where $A_{s,i}$ is the area of the reinforcement of the i^{th} layer and $y_{s,i}$ is the distance from the bottom of the beam to the centre of the average diameter of the i^{th} layer of reinforcement.

As the non-uniform distribution of concrete constituents increases sectional stiffness towards the bottom (Jeong, et al., 2015; Hoshino, 1989), the effective centroid of concrete stiffness ($G_{c,ef}$) moves away from the geometrical centroid (G_c) to a distance (e_c) of about 3% to 5% of the total height. The eccentricity ($e_{c,exp}$) was calculated from experimental curvatures using elastic analysis, Equation (3.4), by assuming a fictitious moment (M_{cs}) created by the equivalent force developed due to shrinkage strain.

$$k_{cs,exp}(t) = \frac{M_{cs}}{E_{c,ef} I_c} = \frac{\varepsilon_{cs}(t) E_{c,ef} A_c e_{c,exp}}{E_{c,ef} I_c} \quad \therefore \; e_{c,exp} = \frac{k_{cs,exp} I_c}{\varepsilon_{cs}(t) A_c} \tag{3.4}$$

where $k_{cs,exp}$ is the experimental shrinkage curvature, $E_{c,ef}$ is the effective elastic modulus of concrete, I_c is the second moment of area of the concrete section, ε_{cs} is the free drying shrinkage at the desired age and A_c is the total area of concrete.

This eccentricity was found to have an approximately linear relationship with the amount of slump (S in mm) (Figure 3.14a), as well as with a factor that accounts for the amount of coarse aggregates (C in kg/m^3), specimen height (h in mm) and slump (Figure 3.14b). Slump was included in this model as a measure of workability and hence the model cannot be applied directly to self-compacting concrete (SCC) or roller-compacting concrete (RCC). It should be also noted that the distribution of concrete constituents and the position of $G_{c,ef}$ can be affected by the extent of vibration and tamping as these affect the rheology of concrete (Hu, 2005).

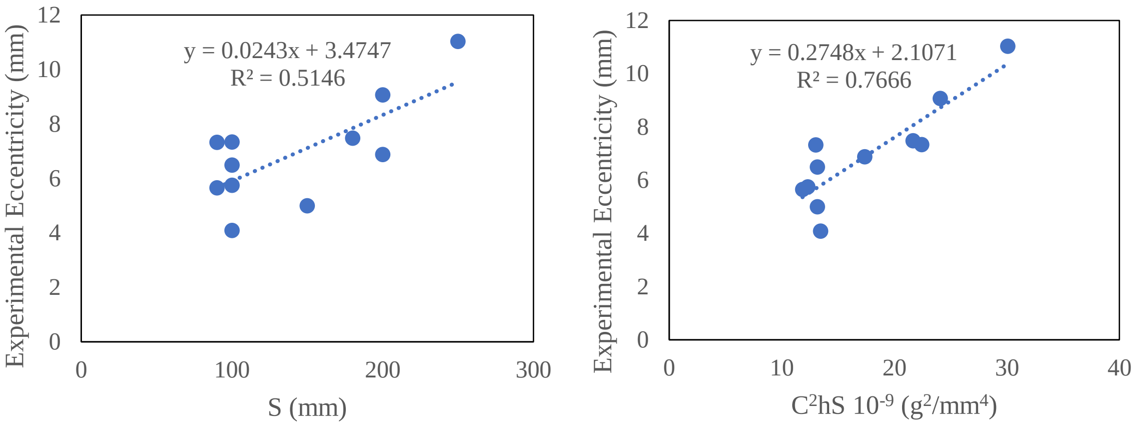

Figure 3.14 Correlation between experimental eccentricity and (a) slump, (b) coarse aggregates, height and slump.

The decrease in the amount of coarse aggregates (*C*) is normally followed by an increase in the amount of fine aggregates (*F*), which requires greater amounts of cement and water. Thus, the model considers *C/F* as an influential parameter for e_c. Well graded particles in a mix provide good packing and less air content, leading to higher density (ρ) and viscosity (Hu, 2005). This results in lower segregation and bleeding, thus providing a more uniform distribution of the concrete constituents. A higher amount of binder (*B*) normally requires higher amounts of water and superplasticisers (added as a percentage of binder), which contribute to limiting the agglomeration of matrix and yield higher slump values (Flatt, 2004). Larger coarse aggregates (*D*) normally require less amount of free water and, consequently, smaller amounts of binder and fine aggregates (Hu, 2005). The above parameters are included in the proposed model based on their expected effect on concrete constituent distribution to determine the value of eccentricity as shown in Equation (3.5). The constant (*k*) is a calibration factor, which was found to be equal to 0.11 for the mixes examined in this study.

$$G_{c,ef} = G_c - e_c = G_c - k \cdot \frac{C^2 B}{\rho^2 F} \cdot \frac{hS}{D} \qquad (3.5)$$

where all weights are in kg/m^3, and all dimensions are in *mm*.

The homogenized centroid (G_h) can be calculated by using the centre of concrete stiffness and centre of homogenized reinforcement as shown in Equation (3.6).

$$G_h = \frac{A_c G_{c,ef} + \alpha_e \sum A_{si} y_{si}}{A_c + \alpha_e \sum A_{si}} \qquad (3.6)$$

where A_c is the total area of concrete and α_e is the effective modular ratio.

Equation (3.7) (Bažant, 1972) provides the effective modular ratio by accounting for aging and creep. Aging factor (χ) can vary from 0.5 to 1.0 (Bažant, 1972) and the creep coefficient can be obtained from design codes.

$$\alpha_e(t) = \frac{E_s}{E_c}\left(1 + \chi(t, t_o) \cdot \varphi(t, t_o)\right) \qquad (3.7)$$

where E_s and E_c are the elastic moduli for steel and concrete, respectively, $\chi(t,t_o)$ is the aging factor and $\varphi(t,t_o)$ is the creep coefficient.

Assuming a uniform distribution of shrinkage strains, as in current guidelines, which will induce a fictitious force acting over the geometrical centroid of the section that will induce a fictitious moment (M_{cs}) due to an eccentricity in the homogenised section, shrinkage induced curvature in a non-cracked section can be calculated by taking the moment about the geometrical centroid as shown in Equation (3.8).

$$k_{cs} = \frac{M_{cs}}{E_{c,ef} I_g} = \frac{\varepsilon_{cs} E_{c,ef} A_c (G_c - G_h)}{E_{c,ef} I_g} = \frac{\varepsilon_{cs} A_c e_h}{I_g} \qquad (3.8)$$

where ε_{cs} is the free drying shrinkage (average strain obtained from design guidelines) at the desired age, e_h is the homogenized centroid, $E_{c,ef}$ is the effective elastic modulus of concrete and I_g is second moment of area about G_h, Equation (3.9).

$$I_g = \frac{1}{12}bh^3 + (\alpha_e - 1)A_s(G_h - G_s)^2 \qquad (3.9)$$

If M_{cs} is taken as the sum of two fictitious moments induced by eccentricities in reinforcement ($M_{cs,bar}$) and concrete ($M_{cs,con}$), Equation (3.8) can be rewritten as Equation (3.10).

$$k_{cs} = \frac{M_{cs,bar} + M_{cs,con}}{E_{c,ef}I_g} = \frac{\varepsilon_{cs}E_sA_s(G_h - G_s) + \varepsilon_{cs}E_{c,ef}A_c\left(G_c - G_{c,ef}\right)}{E_{c,ef}I_g} \qquad (3.10)$$

3.5.2 Validation of the proposed model

3.5.2.1 Plain concrete

Figure 3.15 compares the experimental shrinkage curvatures of plain concrete sections with a height of 150 mm to the model predictions (Equation (3.9)). The experimental data represent averages of at least three specimens per mix and were obtained from this study (P0000-Exp) and from Jeong et al. (2015) (A and C). Mixes A and C were similar and differed mainly in slump (200 mm and 150 mm, respectively). Such difference in slump affected shrinkage curvature by about 1.0 m^{-3} and this was accurately predicted by the proposed model. The concrete used for specimens P0000 had higher compressive strength than that of mixes A and C and resulted in higher rates of shrinkage curvature during the first 28 days, possibly induced by autogenous shrinkage, whilst a lower shrinkage curvature is seen after 28 days, possibly due to its higher stiffness and lower overall shrinkage strains. Despite the many differences between the three groups of specimens in terms of size, concrete constituents, slump, stiffness and development of shrinkage strains, the values predicted by the proposed model are found to be in good agreement with the experimental results.

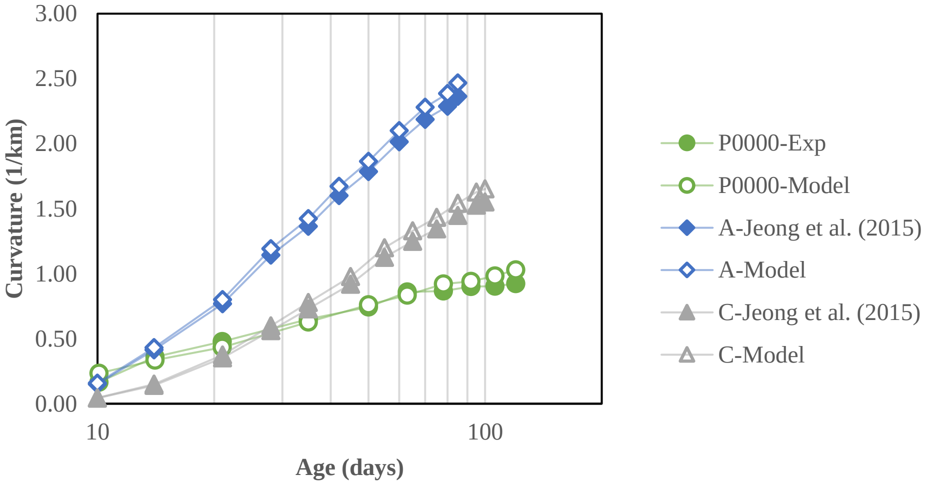

Figure 3.15 Predicted and experimental shrinkage curvature of plain concrete specimens, 150 mm thick.

Figure 3.16 shows the shrinkage curvature of three plain concrete specimens with depth of 100 mm examined by the authors in a previous study (Al-Kamyani, et al., 2018). Each data set represents the average of three prisms. The three mixes differed only in the amount of water and resulting workability. The fast development of shrinkage curvature during the first few days in specimens made with mix P13 was due to the higher migration of water particles as a result of higher water-to-cement (w/c) content. P20 specimens experienced the lowest shrinkage curvature as well as the lowest workability during casting. Again, the model predicts very well the impact of w/c content on shrinkage curvature.

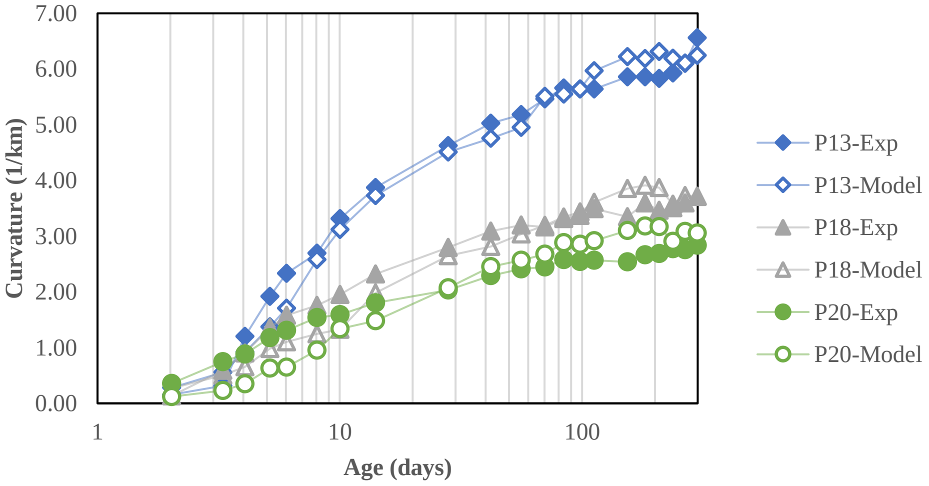

Figure 3.16 Predicted and experimental (Al-Kamyani, et al., 2018) shrinkage curvature of plain concrete specimens, 100 mm thick.

Figure 3.17 shows the shrinkage curvature of specimens made with four different mixes (three specimens per mix) as reported by Younis (2014). The four concrete mixes differed mainly in w/c ratios and the relative amount of the other mix constituents, which was adjusted to achieve similar workability. The mix ID shows the w/c used for each mix, eg. NA30 is a mix made with natural aggregates and w/c 0.3. Since the slump was designed to be in the same range for all mixes, a lower w/c ratio would demand the use of a higher amount of coarse aggregates and this would result in a higher shrinkage restraint at the bottom of the section. NA30 resulted in higher shrinkage curvature than NA40 due to its higher amount of coarse aggregates and lower amount of fine aggregates. Despite the higher w/c ratio, the lower amount of coarse aggregates used in NA50 resulted in higher shrinkage strains at the bottom of the specimens, due to the lower restraint, and similar curvature as those observed in NA40. As evidenced by these experimental results, changing concrete constituents and keeping the slump in the same range altered the height wise distribution of the constituents and changed the evolution of shrinkage curvatures. The proposed model agrees well with the experimental results and can simulate well the effect of all of the investigated parameters.

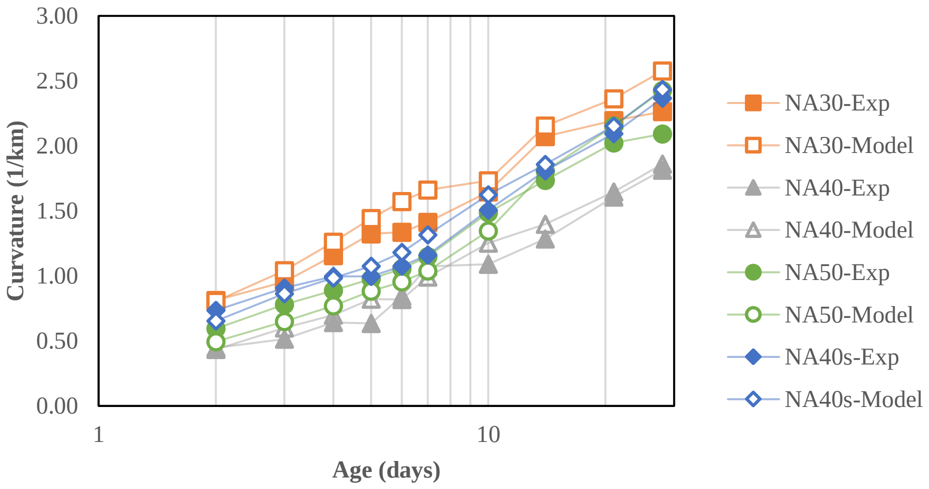

Figure 3.17 Predicted and experimental (Younis, 2014) shrinkage curvature of plain concrete specimens, 100 mm thick.

3.5.2.2 Asymmetrically reinforced elements

Figure 3.18 compares the experimental (-Exp) shrinkage curvature values of asymmetrically reinforced concrete prisms (150 mm high) to the theoretical (-Th) values obtained according to elastic principles (Equation (3.2)) and the proposed model (Equation (3.9)). The average experimental shrinkage curvature values were obtained from three singly reinforced concrete elements per mix (see Figure 3.2b). It is clear that Equation (3.2) underestimates overall curvatures as it ignores the unreinforced concrete curvature. The proposed model approximates very well the behaviour of prisms reinforced with 10 mm bars but tends to underestimate shrinkage curvatures of the prisms reinforced with 16 mm bars. Although the raw data are reliable, with standard deviation of 0.2 m^{-3}, and they are the result of the average from three specimens, it is still difficult to justify this underestimation.

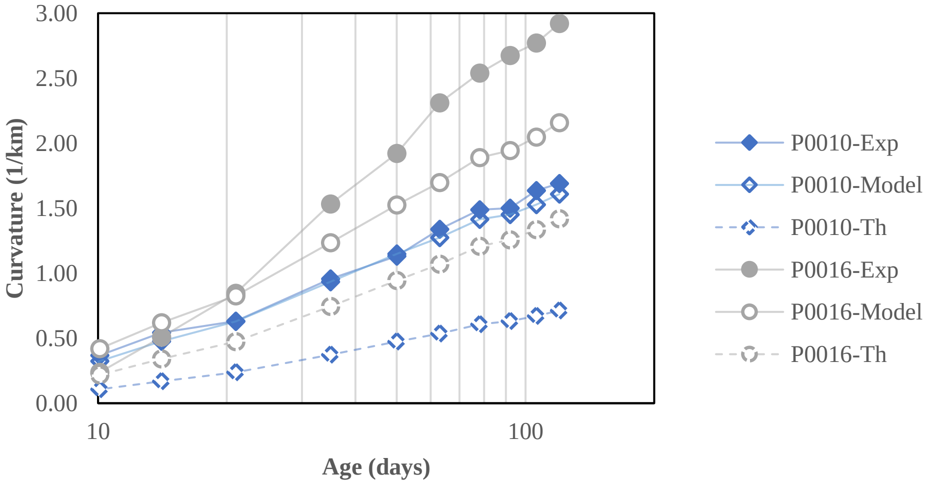

Figure 3.18 Predicted and experimental shrinkage curvature of asymmetric reinforced concrete prisms, 150 mm thick.

3.5.2.3 Symmetrically reinforced elements

Figure 3.19 compares the experimental shrinkage curvatures of symmetrically reinforced beams (250 mm high) reinforced with 10 mm or 16 mm bars with the analytical values obtained using Equation (3.9). As expected, B0010 has higher shrinkage curvature compared to beam B0016 due to the lower degree of internal restraint. At 120 days, shrinkage curvature was about 0.4 m^{-3} for the beam reinforced with 10 mm bars and about 0.3 m^{-3} for the beam reinforced with 16 mm bars, despite all current models predicting a curvature equal to zero. The proposed model, which considers the non-uniform distribution of concrete constituents, is shown to provide a good estimate of curvatures for both ratios of reinforcement. It can be shown from section analysis that shrinkage curvature induced by the non-uniform distribution of concrete constituents can be equivalent to about half of the curvature at cracking (M_{cr}) and therefore, should be accounted for in order to obtain more accurate predictions of long-term curvatures, crack widths and deflection in structural elements.

It should be noted that there is limited experimental work reported in this field, hence more work is needed to validate the proposed model, in particular for large structural elements.

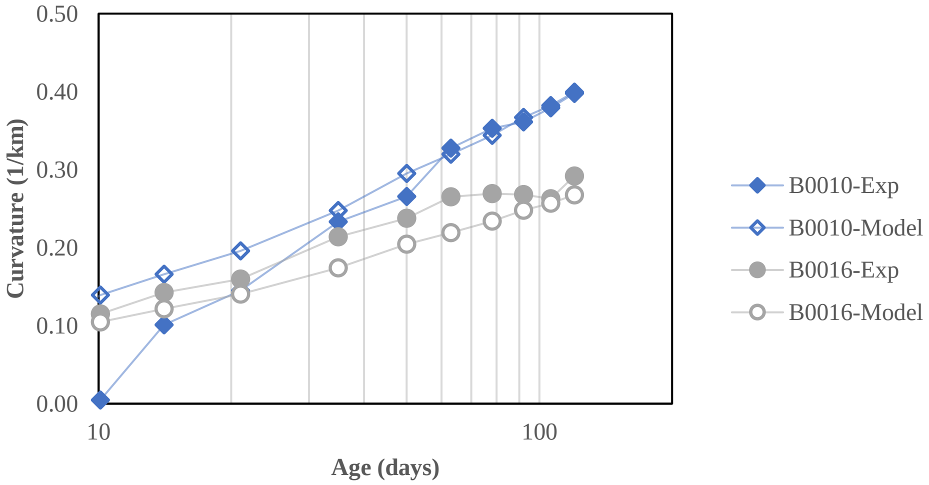

Figure 3.19 Predicted and experimental shrinkage curvature of symmetric reinforced concrete beams, 250 mm thick.

3.6 Conclusions

Shrinkage curvature of non-cracked sections is thought to be caused only by the asymmetric distribution of reinforcement about the geometrical centroid of the section, as concrete components are normally assumed to be distributed uniformly throughout the section. This research investigated non-uniform drying shrinkage in both plain and reinforced concrete elements and examined the effect of aggregate distribution in plain concrete and SFRC. A prediction model for shrinkage induced curvature is proposed on the basis of the experimental insights gained into the effect of fresh properties and distribution of concrete constituents on the distribution of shrinkage strain throughout the cross-section of structural elements of varying depth. Based on the experimental findings of this study and previous available data, the following conclusions can be drawn:

1. Coarse aggregates tend to settle towards the bottom of the section (casting from top) due to their relative high density and vibration of fresh concrete by about 3% to 5% of the total height; the uneven distribution of aggregate decreases with increased dosage of steel fibres.
2. The non-uniform distribution of concrete constituents leads to non-uniform shrinkage through the section depth and can induce a section curvature equivalent to about half the curvature at cracking moment. Thus, such deformations that occur before loading should be accounted for in order to obtain more accurate predictions of curvatures and deflection in structural elements.
3. Shrinkage curvatures observed in SFRC specimens were always lower than those recorded in plain concrete, mostly due to the presence of steel fibres, which worked as a mesh and prevented some coarse aggregates from settling to the bottom of the section.
4. The proposed model is capable to account for the change in the centre of resistance of the non-cracked section due to the uneven distribution of stiffness and yields very good predictions for a variety of different configurations and concrete mix designs.

The proposed model was validated on limited data obtained from non-cracked sections and additional work is needed to extend its applicability to cracked sections. Since the model is able to predict the shrinkage at any level of the section, predicted shrinkage strain at the extreme fibres of a cracked section will differ from that predicted by uniform models. This will have some implications on calculations of neutral axis and thus, the calculations of the corresponding stresses in the reinforcement and the concrete block. Also, additional work is needed to understand the effect of fibres on the distribution of concrete constituents and on other key parameters such as reinforcement distribution and element size.

References

Al-Kamyani, Z., Pilakoutas, K., Guadagnini, M. & Papastergiou, P., 2018. *Free and Restrained Shrinkage of Hybrid Steel Fibres Reinforced Concrete.* Cham, Springer International Publishing.

Aly, T. & Sanjayan, J. G., 2008. Shrinkage cracking properties of slag concretes with one-day curing. *Magazine of Concrete Research,* 1(60), pp. 41-48.

Bartolac, M. et al., 2016. *Punching of slabs reinforced with recycled steel fibres from used tyres.* Dundee, University of Dundee – Concrete Technology Unit.

Bažant, Z. P., 1972. Prediction of Concrete Creep Effects Using Age-Adjusted Effective Modulus Method. *ACI,* 69(20), pp. 212-217.

Bažant, Z. P., Yu, Q. & Li, G.-H., 2012b. Excessive Long-Time Deflections of Prestressed Box Girders. II: Numerical Analysis and Lessons Learned. *Journal of Structural Engineering,* 138(6), pp. 687-696.

Bažant, Z. P., Yu, Q. & Li, G.-H., 2012. Excessive Long-Time Deflections of Prestressed Box Girders. I: Record-Span Bridge in Palau and Other Paradigms. *Journal of Structural Engineering,* 138(6), pp. 676-686.

Beddar, M., 2005. *An experimental study of porosity and premeability characteristics of steel fibre reinforced concrete.* Dundee, Institute of Civil Engineers.

Brown, M., Sellers, G., Folliard, K. J. & Fowler, D. W., 2001. *Restrained shrinkage cracking of concrete bridge decks: state-of-the-art review,* Texas: The University of Texas at Austin.

BSI, 1997. *BS-8110 Structural use of concrete - Part 1: Code of practice for design and construction.* Second ed. London: BSI.

CEN, 2008. *Eurocode 2: Design of concrete structures, Part 1-1: General rules and rules for Structures 2004,* Brussels: European Committee for Standardization.

fib, 2010. *Structural Concrete Textbook on behaviour, design and performance, Second edition Volume 2: Basis of design.* 1st ed. Siegmar Kästl e.K.: Document Competence Center.

Filho, R. D. T., Ghavami, K., Sanjua´n, M. A. & England, G. L., 2005. Free, restrained and drying shrinkage of cement mortar composites reinforced with vegetable fibres. *Cement & Concrete Composites,* 27(5), pp. 537-546.

Flatt, R. J., 2004. Towards a prediction of superplasticized concrete rheology. *Materials and Structures,* 37(5), pp. 289-300.

Forth, J. P. et al., 2014. Verification of cracked section shrinkage curvature models. *Proceedings of the Institution of Civil Engineers - Structures and Buildings,* 167(5), pp. 274-284.

Ghali, A. & Favre, R., 1994. *Concrete Structures: Stresses and Deformations.* Second ed. London: E&FN Spon.

Gilbert, R., 2001. Shrinkage, Cracking and Deflection - the Serviceability of Concrete Structures. *Electronic Journal of Structural Engineering,* 1(1), pp. 15-37.

Graeff, A., 2011. *Long-term performance of recycled steel fibre reinforced concrete for pavement applications,* Sheffield: The University of Sheffield.

Gribniak, V., Kaklauskas, G. & Bacinskas, D., 2007. State-of-art Review of Shrinkage Effect on Cracking and Deformations of Concrete Bridges Elements. *The Baltic Journal of Road and Bridge Engineering,* II(4), pp. 183-193.

Gribniak, V., Kaklauskas, G., Kliukas, R. & Jakubovskis, R., 2013. Shrinkage effect on short-term deformation behavior of reinforced concrete – When it should not be neglected. *Materials and Design,* Volume 51, p. 1060–1070.

Groli, G., 2014. *Crack width control in RC elements with recycled steel fibres and applications to integral structures: theoritical and experimental study,* Madrid: Polytechnic University of Madrid.

Groli, G. & Caldentey, A. P., 2017. Improving cracking behaviour with recycled steel fibres targeting specific applications – analysis according to fib Model Code 2010. *fib Structural Concrete,* Volume 18, pp. 29-39.

Hobbs, D. W., 1974. Influence of Aggregate Restraint on the Shrinkage of Concrete. *ACI Journal*, pp. 445-450.

Hoshino, M., 1989. Relation Between Bleeding, Coarse Aggregate, and Specimen Height of Concrete. *ACI Materials Journal,* 86(2), pp. 185-190.

Huang, H., Garcia, R., Guadagnini, M. & Pilakoutas, K., 2017. Effect of section geometry on development of shrinkage-induced deformations in box girder bridges. *Materials and Structures,* 50(222), pp. 1-14.

Hu, J., 2005. *A study of effects of aggregate on concrete rheology,* Ames: Iowa State University Digital Repository.

Jeong, J.-H., Park, Y.-S. & Lee, Y.-H., 2015. Variation of Shrinkage Strain within the Depth of Concrete Beams. *Materials,* pp. 7780-7794.

Kong, F. K. & Evans, R. H., 1987. *Reinforced and Prestressed Concrete.* 3rd ed. s.l.:Springer-Science+Busines Media, B.V..

Maekawa, K., Chijiwa, N. & Ishida, T., 2011. Long-term deformational simulation of PC bridges based on the thermo-hygro model of micro-pores in cementitious composites. *Cement and Concrete Research,* Issue 41, p. 1310–1319.

Martinelli, E., Caggiano, A. & Xargay, H., 2015. An experimental study on the post-cracking behaviour of Hybrid Industrial/Recycled Steel Fibre-Reinforced Concrete. *Construction and Building Materials,* Volume 94, pp. 290-298.

Neville, A. M., 2004. *Properties of Concrete.* Fourth ed. London: Pearson Education Limited.

Pan, Z., Fu, C. C. & Jiang, Y., 2011. Uncertainty Analysis of Creep and Shrinkage Effects in Long-Span Continuous Rigid Frame of Sutong Bridge. *Journal of Bridge Engineering,* 16(2), pp. 248-258.

Tanimura, M., Sato, R. & Hiramatsu, Y., 2007. Serviceability Performance Evaluation of RC Flexural Members Improved by Using Low-Shrinkage High-Strength Concrete. *Journal of Advanced Concrete Technology*, 5(2), pp. 149-160.

Younis, K. H., 2014. *Restrained shrinkage behaviour of concrete with recycled materials,* Sheffield: The University of Sheffield.

Zdanowicz, K. & Marx, S., 2018. *Shrinkage and Expansion Strains in Self-compacting Concrete Comparison of Methods of Measurements.* Maastricht, Springer International Publishing.

Zhang, W., Hama, Y. & Na, S. H., 2015. Drying shrinkage and microstructure characteristics of mortar incorporating ground granulated blast furnace slag and shrinkage reducing admixture. *Construction and Building Materials*, Issue 93, pp. 267-277.

Chapter 4: Impact of Shrinkage on Crack Width and Deflections of Reinforced Concrete Beams with and without Steel Fibres

Al-Kamyani*, *Z., *Guadagnini, M., Pilakoutas, K., 2018c. Impact of Shrinkage on Crack Width and Deflections of Reinforced Concrete Beams with and without Steel Fibres. Engineering Structures,* ***Submitted for Publication (with reviewers)****.*

Abstract

Current recommendations by *fib* Model Code 2010 only consider the effect of shrinkage strains on long-term crack width calculations of reinforced concrete (RC) elements. However, shrinkage strains develop fairly early and can influence mean strains as well as short-term crack width and deflection calculations. This paper examines the effect of shrinkage strains on short-term deformations using experiments on eight RC beams, with and without steel fibres, at the age of 4-5 months. The results show that due to shrinkage, measured strains, deflections and crack widths are higher than expected for fully cracked sections. The MC-2010 predictive equation is amended to account for shrinkage strains and induced curvatures. This work will lead to better predictive equations and less serviceability problems in RC structures.

This chapter consists of a "stand alone" journal paper and includes a relevant bibliography at the end of the chapter. Additional information and further test results are presented in Appendix C.

4.1 Introduction

Most concrete structures are monolithically cast and are thus restrained either by adjacent structural elements, bracing elements or the ground. The development of shrinkage strains depends on the size of the elements but can significantly affect their overall behaviour both before and after cracking. Prior to cracking, shrinkage of concrete induces compression forces on the reinforcement, which result in additional tensile stresses in concrete. The tensile stresses cause micro-cracking in the cement matrix, in particular around the reinforcement. These cracks can be even large enough to cause visible cracking on the concrete and are expected to develop due to restrained shrinkage within a period of 3-5 days after casting (fib, 2008; Beeby & Scott, 2005; Micallef, et al., 2017). Once cracks develop, compressive strains on the bars are released around the cracks, but as concrete shrinkage continues developing between cracks, it still has a long-term effect on crack width opening (Zanuy, et al., 2010; Groli, 2014). New cracks can reduce crack opening of adjacent cracks, but creep and self-healing also affect crack widths, in particular when the concrete is still immature (fib, 2008; Micallef, 2015; Forth, et al., 2013; Kaklauskas & Ghaboussi, 2001).

The *fib* Model Code 2010 (MC-2010) (fib, 2013) accounts for free shrinkage strains in the calculations for long-term crack widths. However, for short-term crack width calculations shrinkage strains are neglected. This is of significance in laboratory tests that are used to calibrate design equations where structural elements are not subjected to external loads or restraints beyond cracking stresses during their early ages and are tested within few weeks/months of casting. In these tests, unless specifically monitored, shrinkage strains developed prior to testing cannot be directly measured but can affect the prediction of mean reinforcement strain and can result in crack width underestimation. Shrinkage strains can also cause higher deformations, even beyond the deformations expected by a fully cracked section, implying a negative tension stiffening effect (Bischoff, 2001; Gribniak, et al., 2013). For example, in laboratory testing the total measured strain in the tensile reinforcement (or even in deflection) can be higher than expected as it includes a component of apparent tensile strain resulting from the compression induced by shrinkage before loading.

There are several approaches in literature that quantify excessive strains and deflections due to shrinkage in RC elements (Bischoff, 2001; Groli, 2014; Gribniak, et al., 2013; Gribniak, et al., 2012). Basically, all methods add shrinkage and creep strains or curvatures to the expected short-term deformations. Bischoff (2001) added shrinkage strains to the member mean strain by assuming the development of uniform shrinkage strain through the height of the section. Groli (2014) added the contribution of total effective shrinkage strain (by considering the effect of modular ratio and effective ratio of reinforcement) in RC and shrinkage induced curvature together, but then concluded that the effect of shrinkage induced curvature is minor and can be neglected. Kakluaskas (2004) and Kakluaskas et al (2017) presented methods for removing the shrinkage effect in the moment-curvature (M-k) relationship. However, all these approaches adopt uniform shrinkage development through the height of the plain concrete section, whilst there is strong evidence that shrinkage is not necessarily uniform through the section (Al-Kamyani, et al., 2017; Jeong, et al., 2015; Younis, 2014). Shrinkage strains at the top (cast surface) being twice as much as these strains at the bottom of the section.

Vibration of fresh concrete and water bleeding can affect the distribution of concrete constituents and thus can affect the distribution of internal stiffness (Hobbs, 1974; Hoshino, 1989). Variation in section stiffness will result in non-uniform development of shrinkage strains through the height of the section, even in symmetrically reinforced sections.

Therefore, it is expected that variations in section shrinkage strains will increase sectional curvature and have some effect in the prediction of crack width and deflections.

Cracking of reinforced concrete can be controlled by reducing the amount of shrinkage strain, increasing the concrete tensile strength or better dissipating generated tensile strains through skin reinforcement or distributed fibres. However, longitudinal skin reinforcement can cause congestion and construction quality issues, while randomly distributed fibres alone are in general only capable of bridging micro-cracks. The combination of fibres with conventionally reinforced concrete was found to reduce crack spacing, and as a consequence, crack widths (Groli, et al., 2014; Groli & Caldentey, 2017; Tan, et al., 1995; Gribniak, et al., 2012). Recently, it has been shown that recycled tyre steel fibre (RTSF) can also be used in SFRC (Al-Kamyani, et al., 2017; Martinelli, et al., 2015; Groli, 2014), but its use with conventional reinforced concrete is not well investigated, especially with recent developments in fibre classification and cleaning.

This study aims to investigate experimentally the effect of shrinkage strains in the development of crack widths and deflection in RC beams with and without blends of manufactured fibre and RTSF. This paper examines the development of non-uniform shrinkage in symmetrically RC beams and its impact on crack width prediction and modifies the MC-2010 approach for crack width predictions.

The next section presents the experimental details including the parameters examined, experimental setup and basic material characteristics. This is followed by a presentation of the strain results including strain on the flexural reinforcement and a discussion on effective element strains. The results on crack spacing and width are presented next including a discussion on maximum crack width prediction. Finally, deflection results are presented, and the effect of shrinkage and cracking on deflection is discussed.

4.2 Experimental Details

Flexural tests are undertaken on prisms to determine mechanical characteristics and on RC beams to determine the effect of shrinkage strains on the deformation behaviour.

4.2.1 Prisms

A total of eighteen 150x150x550 mm prisms were used to obtain the flexural tensile characteristics and concrete compressive strength of plain concrete and SFRC. Six of the prisms were manufactured using plain concrete (P0000) and the remaining twelve with hybrid SFRC [six with 20 kg/m^3 of fibres (P2000) and six with 30 kg/m^3 of fibres (P3000)].

The prisms were tested in three-point flexure according to BS EN 14561:2005 by controlling crack mouth opening displacement (CMOD). Undamaged portions of these prisms were used to obtain concrete compressive strength (f_{cm}) according to BS EN 1881-119. Indirect concrete tensile strength (f_{ctm}) was obtained according to MC-2010 recommendations by dividing the flexure strength (f_{LOP}) by the correction factor shown in Equation (4.1), from *fib* bulletin 42 (fib, 2008).

$$k_{fl} = \frac{1 + \alpha_{fl}\left(\frac{h_b}{h_o}\right)^{0.7}}{\left(\frac{h_b}{h_o}\right)^{0.7}} \qquad (4.1)$$

where k_{fl} is an empirical correction factor for results obtained from flexure tests, h_b is the beam depth in mm, h_o is 100 mm, α_{fl} is a coefficient which depends on the characteristic length (recommended value 1.5).

4.2.2 Beams

The experimental programme examined eight RC beams (150x250x2500 mm) that were symmetrically reinforced with four longitudinal steel bars (10 mm and 16 mm) as shown in

Figure 4.1. All beams had a concrete clear cover of 20 mm except the two beams labelled with letter “C” in Table 4.1, which had a clear cover of 40 mm.

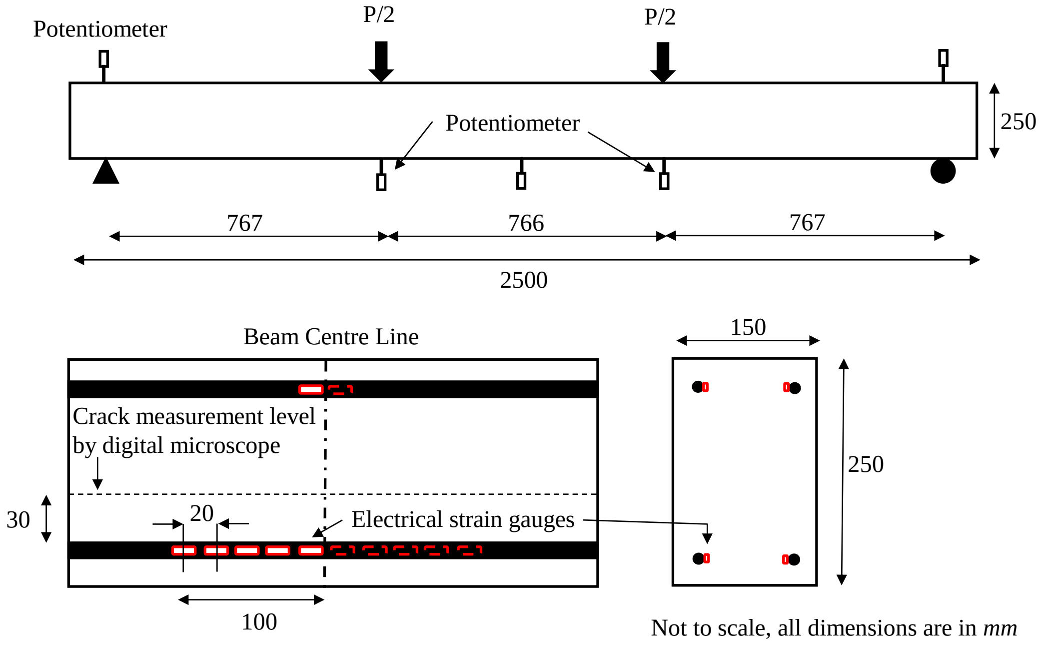

Figure 4.1 Beam typical cross section details, loading layout and distribution of instrumentations.

Each beam was instrumented with twelve 10-mm long electrical bar strain gauges in the middle span; 5 strain gauges were fixed on the two bottom bars and one on the two top bars, as shown in Figure 4.1. The beams were kept under laboratory conditions after 7 days of wet hessian curing. Shrinkage strains were measured on the concrete surface along the beams using a DEMEC gauge with a gauge length of 300 mm at the level of the top and bottom reinforcement for a period of 4 months. The beams were tested in four-point bending (see Figure 4.1) using load control according to BS EN 12390-5:2009 until yielding of the steel reinforcement. Potentiometers were used to measure support settlement and central deflections. Cracks were marked at regular load steps and spacing was measured by a ruler to the nearest 1 mm at the level of reinforcement and after crack stabilisation, whilst crack widths were measured using a digital microscope with a magnification power of x275. Crack measurements were taken at 30 mm above the reinforcement as illustrated in Figure 4.1.

Table 4.1 Beams and materials physical and mechanical characteristics.

Beam	**Age (days)**	**Fibres (kg/m^3)**	**$Ø_s$ (mm)**	**f_{cm} (SD) (MPa)**	**f_{ctm} (SD) (MPa)**	**$\varepsilon_{cs,top}$ (με)**	**$\varepsilon_{cs,bot}$ (με)**	**k_{cs} (km^{-1})**
B0010	132	-	10	45.7 (0.9)	3.0 (0.2)	441	331	0.44
B2010	154	20	10	49.9 (1.3)	3.0 (0.2)	439	279	0.64
B3010	147	30	10	41.1 (1.1)	2.8 (0.2)	448	348	0.40
C3010	161	30	10	41.1 (1.1)	2.8 (0.2)	473	330	0.57
B0016	136	-	16	45.7 (0.9)	3.0 (0.2)	309	245	0.26
B2016	156	20	16	49.9 (1.3)	3.0 (0.2)	328	230	0.39
B3016	163	30	16	41.1 (1.1)	2.8 (0.2)	336	248	0.35
C3016	162	30	16	41.1 (1.1)	2.8 (0.2)	391	226	0.66

$Ø_s$: diameter of steel reinforcement; f_{cm} and f_{ctm}: concrete mean compressive and tensile strength; $\varepsilon_{cs,top}$ and $\varepsilon_{cs,bot}$: shrinkage strains at extreme top and bottom fibres of beam at day of testing; k_{cs}: shrinkage induced curvature before testing; Fibres: total quantity of MUSF and RTSF (50% each).

4.3 Materials Characteristics

4.3.1 Reinforcement

Four coupons of steel reinforcing bars were tested for each bar diameter (10-mm and 16-mm) according to ASTM A370. The mean yield strength of reinforcement was 520 MPa and 500 MPa for 10-mm and 16-mm steel bars, respectively. The elastic moduli were 207 GPa and 194 GPa for 10-mm and 16-mm steel bars, respectively.

Six beams (R/FRC) were reinforced with two different dosages of blended steel fibres (see Table 4.1). Two types of steel fibres were used in equal proportions, manufactured undulated steel fibres (MUSF) with length/diameter 55/0.8 mm (nominal strength of 1450 MPa), and RTSF with average length/diameter 20/0.2 mm (nominal strength of 2000 MPa).

4.3.2 Concrete

All specimens were cast from the same batch of concrete (ready mix) with water-to-cement ratio of 0.6. Fibres were integrated in the concrete manually in a drum mixer. The quantities of cement (CEM I 52.5R), river gravel (20/4 mm) and river sand (4/0 mm) were

310, 947 and 947 kg/m^3, respectively. Retarder (Rheomix 500R) and superplasticiser (Master Polyheed 410) were used in doses of 1.2 and 1.5 Lt/m^3, respectively.

The compressive strength of each mix is shown in Table 4.1. The tensile properties were determined indirectly, using flexural tests. Figure 4.2 shows the flexural stress versus CMOD for plain concrete and SFRC prisms. All mixes experienced softening after first crack. The flexural strength of plain concrete (P0000) and mix P2000 were similar. However, mix P3000 had lower average strength by about 8%, even though it exhibited similar post peak behaviour to mix P2000. Residual flexural strength values (f_{Rs}) at different crack widths are shown in Table 4.2. f_{Fstm} is derived from f_{R1} and is used in the calculation for crack spacing and width according to MC-2010 [i.e. f_{Fstm}=0.45(f_{R1}-1.64SD)/0.7, where SD is the standard deviation].

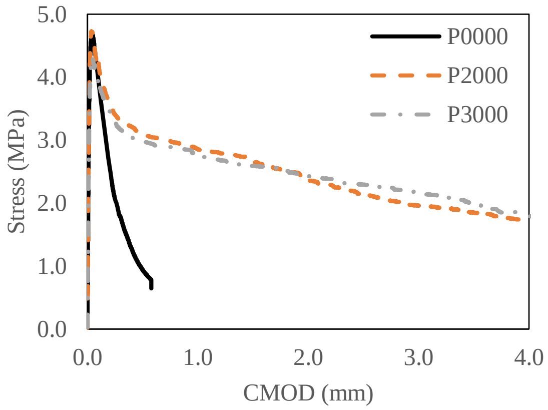

Figure 4.2 Flexural stress versus CMOD.

Table 4.2 Residual flexural tensile strength values with standard deviation (SD).

f_R	CMOD (mm)	P0000 (MPa)	P2000 (MPa)	P3000 (MPa)
f_{LOP}*	0.05	4.7 (0.1)	4.7 (0.3)	4.3 (0.4)
f_{R1}	0.5	0.9 (0.1)	3.1 (0.4)	3.0 (0.5)
f_{R2}	1.5	-	2.7 (0.5)	2.6 (0.5)
f_{R3}	2.5	-	2.1 (0.5)	2.3 (0.4)
f_{R4}	3.5	-	1.9 (0.5)	2.0 (0.4)
f_{Fstm}	*0.5*	-	*1.6*	*1.4*

*Maximum recorded stress up to CMOD of 0.05 mm.

4.4 Strain Results and Discussion

4.4.1 Beam mean strain

Figure 4.3 (a and b) shows the mean strain in R/FRC beams reinforced with 10-mm and 16-mm bars, respectively. Measured mean strains on the reinforcing bars are higher than those predicted by MC-2010, possibly due to shrinkage strains (negative tension stiffening). This is also supported by the fact that apparent measured strains at steel yield load (load level at which the load versus strain or deflection curves soften) were around 3000 micro-strain, well exceeding the reinforcement yielding strain of about 2500 micro-strain. Hence, shrinkage strain need to be considered in greater details.

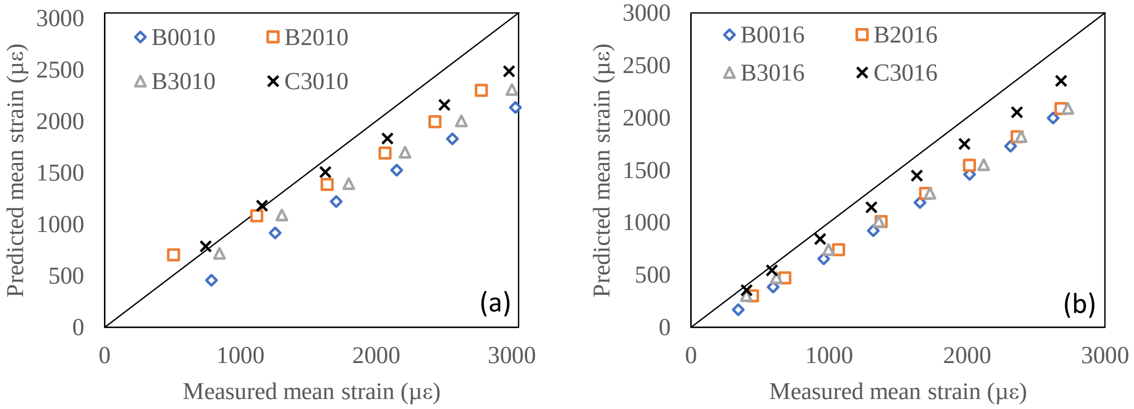

Figure 4.3 Predicted strain by MC-2010 and measured strain in R/FRC beams reinforced with 10-mm (a) and 16-mm (b) bars.

4.4.2 Effect of shrinkage strains

Although the beams were symmetrically reinforced, shrinkage strains at the top of the section of the RC beams were found to be always larger than the bottom. This can be attributed to the uneven distribution of concrete constituents through section height (Al-Kamyani, et al., 2017). Differential section strains lead to the shrinkage curvatures (k_{cs}) reported in Table 4.1. Such curvatures are expected to affect the depth of the neutral axis (NA) and thus, the calculated stresses at the top and bottom fibres of the beam. The effective shrinkage strain at any level i ($\varepsilon_{cs,i}$) of an RC section accounting for the effect of shrinkage curvature can be calculated using Equation (4.2).

$$\varepsilon_{cs,i} = k_{cs}(y_i - y_{RC}) + \varepsilon_{csRC} \qquad (4.2)$$

where k_{cs} is the shrinkage induced curvature (obtained either from design codes or from a new method proposed by the authors - under publication), y_i is the level at which strain is considered (y is equal to zero at the bottom fibre), y_{RC} is the geometrical centroid of the RC element, ε_{csRC} is the average shrinkage strain in an RC element.

The average shrinkage strain can be obtained using Equation (4.3), derived by assuming a fictitious compression force acting on the element due to free shrinkage strains.

$$\varepsilon_{csRC} = \frac{\varepsilon_{cs}}{1 + \alpha_e \rho_{s,eff}} \qquad (4.3)$$

where ε_{cs} is the free shrinkage strains, α_e is the effective modular ratio and $\rho_{s,eff}$ is the effective ratio of reinforcement.

As shrinkage strain affects crack widths, it is proposed that the effective shrinkage strain ($\varepsilon_{cs,i}$) is used instead of ($\eta\varepsilon_{cs}$), used by MC-2010 in calculating the mean strain (ε_m), as shown in Equations (4.4).

$$\varepsilon_m = \left(\varepsilon_{sm} + \varepsilon_{cs,i} - \varepsilon_{cm}\right) \qquad (4.4)$$

The maximum crack width can therefore be predicted more accurately by Equation (4.5).

$$w_{c,max} = s_{max}\, \varepsilon_m \qquad (4.5)$$

where $w_{c,max}$ and s_{max} are the maximum cracking width and spacing, ε_{sm} and ε_{cm} are the mean strains in reinforcement and concrete, respectively.

4.4.3 Predicted mean strain

Figure 4.4 (a and b) shows the predicted mean strain (ε_m) versus the measured strains for R/FRC beams reinforced with 10-mm and 16-mm bars, respectively. The predicted mean strains are slightly higher at early load levels and lower at higher load levels than the measured strains, but on average they are better than predicted by MC-2010.

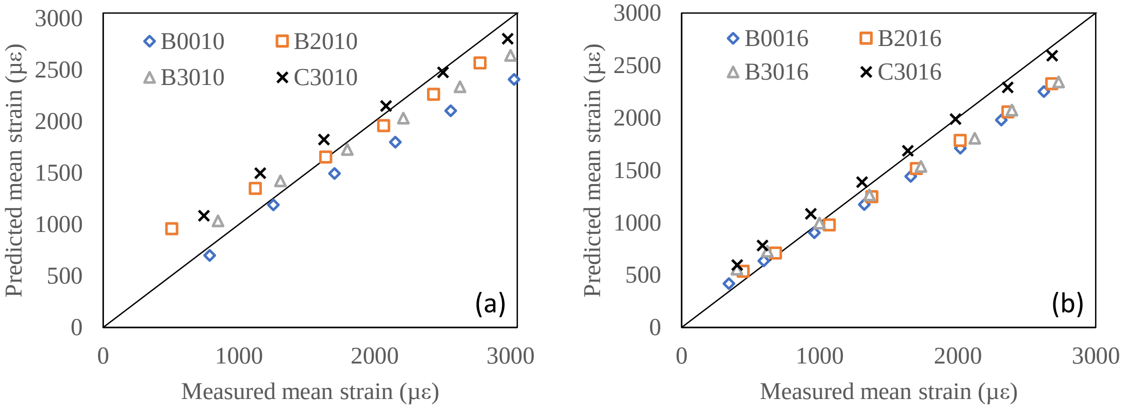

Figure 4.4 Predicted mean strain in cracked R/FRC beams reinforced with 10-mm (a) and 16-mm (b) bars.

4.4.4 Strain profiles

Figure 4.5 (a and b) shows the measured mid-span strain profiles in R/FRC beams reinforced with 10-mm and 16-mm bars, respectively. Measurements were obtained from electrical strain gauges records at the serviceability loads of 25 kN and 50 kN (about 60% of steel yielding strain) for beams reinforced with 10-mm and 16-mm bars, respectively. Nearly all strain values along the examined span of 200 mm were higher than the expected strain at SLS of about 1500 με and about 1300 με in beams reinforced with 10-mm and 16-mm bars, respectively (including the shrinkage strains presented in Table 4.1). Since concrete cannot withstand such strains in tension, these measurements indicate that some internal cracking should exist around the ribs of the deformed bars, evidence of which was provided experimentally by Goto (1971), as will be discussed later.

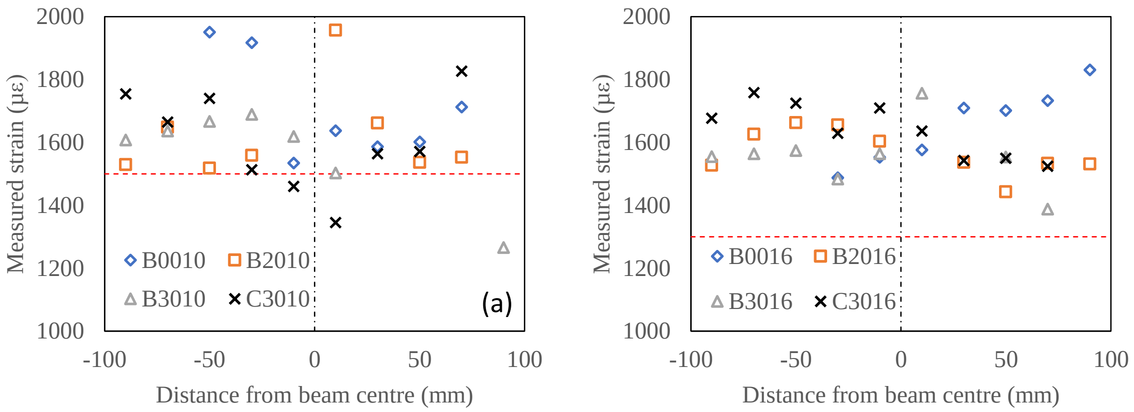

Figure 4.5 Measured strain profiles at service loads in R/FRC beams reinforced with (a) 10-mm and (b) 16-mm bars.

4.5 Cracking Results and Discussion

4.5.1 Crack spacing

Figure 4.6 (a and b) shows the measured maximum crack spacing and MC-2010 predictions for R/FRC beams reinforced with 10-mm and 16-mm bars, respectively. In most beams, the measured maximum crack spacing was slightly lower than predicted by MC-2010. The overestimation was on average about 12% and 4% for beams reinforced with 10-mm and 16-mm bars, respectively. As expected, the maximum crack spacing decreases by increasing steel fibre dosage, whilst it increases by increasing concrete cover. The difference in maximum crack spacing in beams reinforced with 20 kg/m^3 and 30 kg/m^3 of total fibres was relatively small, due to the similarity in concrete tensile strength and other associated characteristics (e.g. residual flexural tensile stresses and bond strength) of these mixes.

Figure 4.7 (a and b) shows the average measured crack spacing and MC-2010 predictions. The average measured crack spacing was obtained by dividing the total span length under pure bending with the observed number of cracks, whilst in MC-2010, the maximum predicted crack spacing is divided by 1.7. Despite some variability in the results, the difference between MC-2010 prediction and experimental measurements was on average only about 8% and 13% for beams reinforced with 10-mm and 16-mm bars, respectively. These results show that MC-2010 makes fairly good predictions of crack spacing.

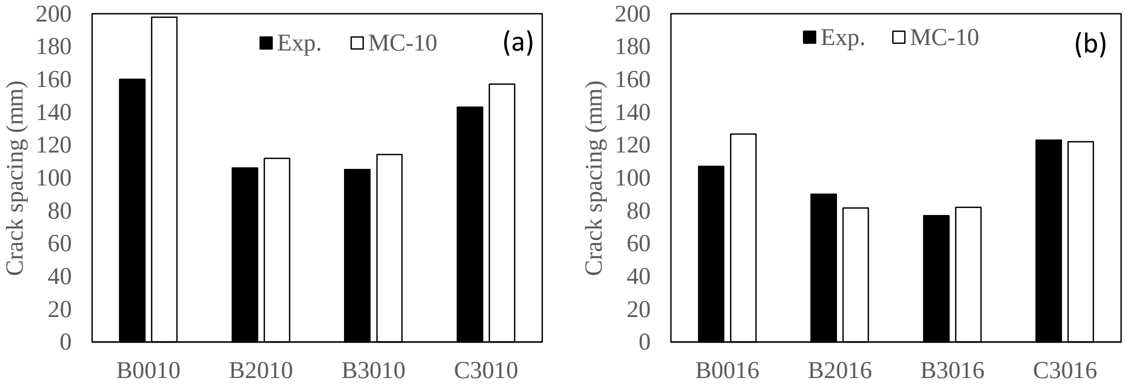

Figure 4.6 Maximum crack spacing in R/FRC beams reinforced with 10-mm (a) and 16-mm (b) bars.

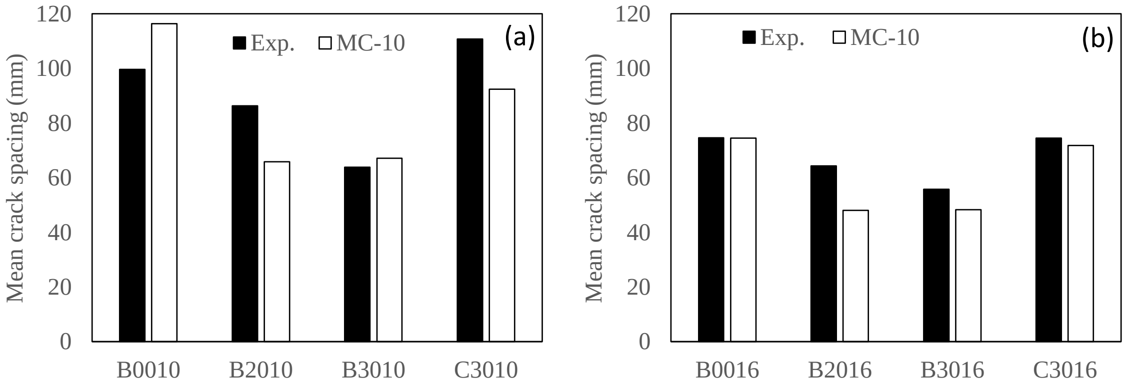

Figure 4.7 Average crack spacing in R/FRC beams reinforced with 10-mm (a) and 16-mm (b) bars.

4.5.2 Crack width

In MC-2010, the maximum crack width at the level of reinforcement is calculated by multiplying the mean strain in the reinforcement with the maximum crack spacing. However, to obtain the maximum crack width at the extreme tensile fibre, the crack width at the level of reinforcement is extrapolated linearly (see Figure 4.8 left). As a result, this approach naturally tends to reduce the crack width towards the neutral axis. However, it has been shown by several researchers (Nazmul & Matsumoto, 2008a; Nazmul & Matsumoto, 2008b; Deng & Matsumoto, 2017) that several minor cracks develop internally along the surface of the bars, and that the visible major crack width increases up to a certain distance away from the reinforcement level (due to internal cracking near the reinforcement) and only then starts closing (as shown in Figure 4.8 right). To address this issue, a distance of 30-mm above the centre of the bars was selected in this study to measure the maximum crack widths, using a digital microscope. Measured crack widths for beams B0010 and B0016 are not reported, as the captured photos were corrupted by light reflection.

The sub-sections below present and compare measured crack widths using the digital microscope versus calculated crack widths from measured strains, strains predicted by MC-2010 and those modified to account for shrinkage. A tension stiffening factor (β) of 0.6 and a creep factor (φ) of 1.72 were used to predict crack widths.

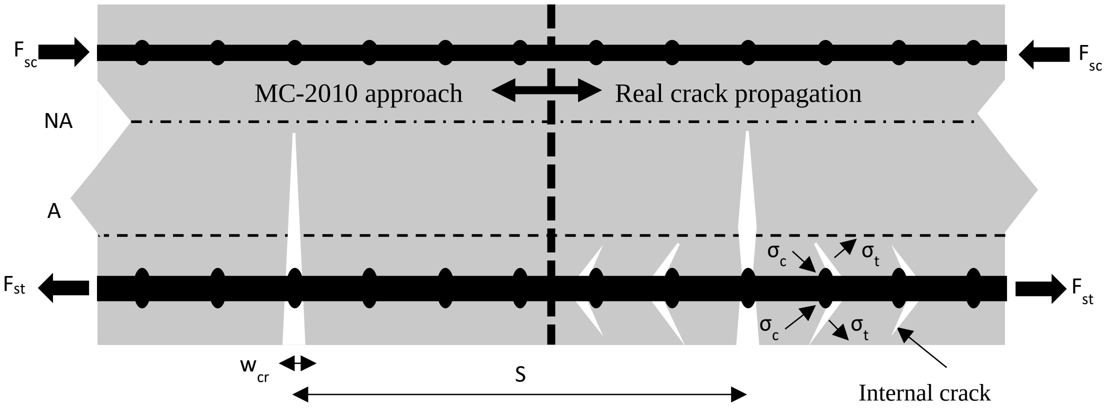

Figure 4.8 Crack width propagation according to MC-2010 approach (left) and with considering internal cracking (right).

4.5.2.1 Calculated crack widths using strain measurements

Figure 4.9 (a and b) shows the calculated crack widths versus measured crack widths for R/FRC beams reinforced with 10-mm and 16-mm bars, respectively. Calculated maximum crack widths are obtained by multiplying the measured maximum crack spacing (Figure 4.6) with the measured mean strain (Section 3).

In beams reinforced with 10-mm bars, calculated crack widths were wider than those measured, possibly due to the development of fine cracks beside the primary cracks (see Figure 4.8) or the crack tendency to close at the level of measurement. This is expected to be a general trend as the calculated crack width assumes that the concrete in-between cracks remains below the cracking strain. However, the measured crack widths in beams reinforced with 16-mm bars were closer to the calculated, possibly due the higher restraint offered by the bigger ribs of the 16-mm bars, which led to fewer internal minor cracks developing as fine cracks on the surface. In fact, fewer fine cracks were observed beside the primary cracks on the R/FRC beams reinforced with 16-mm bars than for the beams reinforced with 10-mm bars.

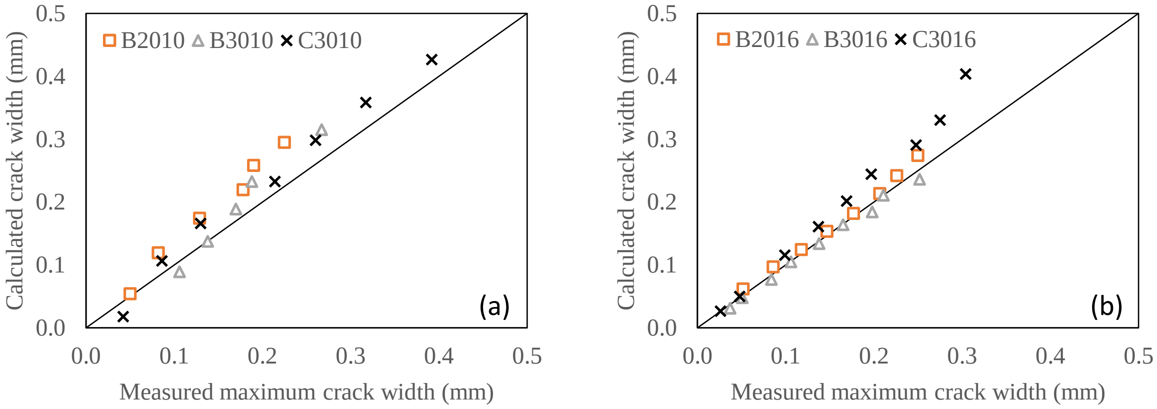

Figure 4.9 Maximum crack widths calculated from strain gauges versus microscope measurements in R/FRC beams reinforced with 10-mm (a) and 16-mm (b) bars.

4.5.2.2 Predicted crack width using MC-2010 approach

Figure 4.10 shows the MC-2010 predicted crack widths at the level of reinforcement and the measured maximum crack widths, at the level of 30 mm above the reinforcing bars. The predicted maximum crack widths were slightly wider than measured in beams reinforced with 10-mm bars and slightly narrower in beams reinforced with 16-mm bars. The MC-2010 predictions are also lower when compared against calculated crack widths using the strain values (both at the level of reinforcement, see Figure 4.11). Although this discrepancy is acceptable and only a limited number of beams have been examined in this study, the underestimation in crack width may be due to the fact that shrinkage strains are not considered in MC-2010. By adding shrinkage strains to the predictions of MC-2010, calculated crack widths come closer to the predicted crack widths (see Figure 4.12). This confirms that accounting for the pre-loading shrinkage strains lead to better estimations of crack widths.

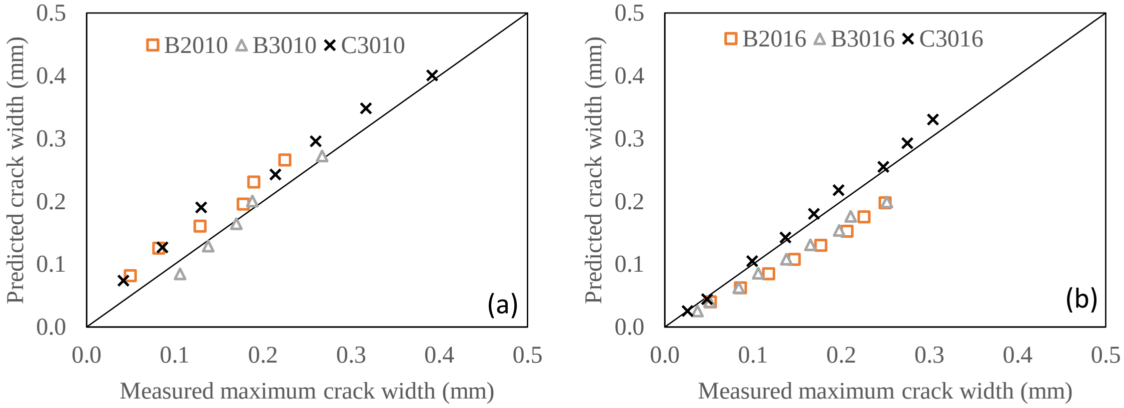

Figure 4.10 Predicted (MC-2010) versus measured crack widths in R/FRC beams reinforced with 10-mm (a) and 16-mm (b) bars.

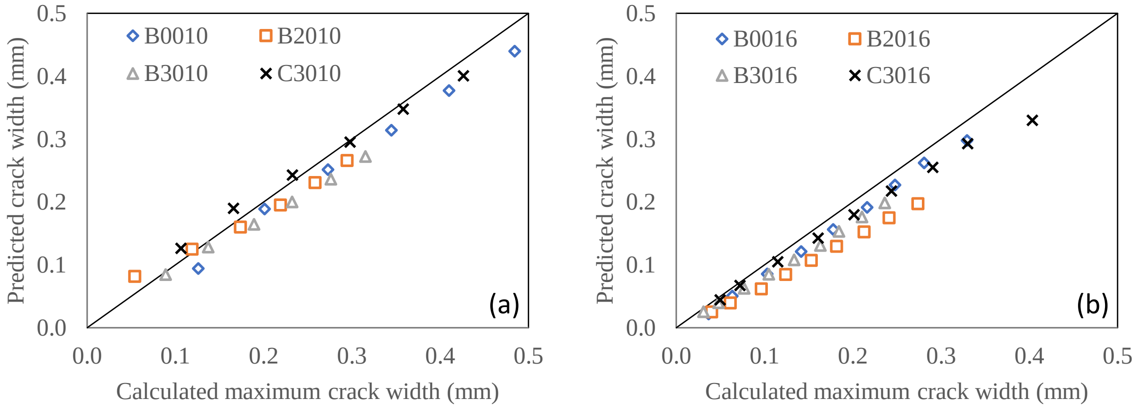

Figure 4.11 Maximum crack width predictions using MC-2010 and calculated from experimental strain values in R/FRC beams reinforced with 10-mm (a) and 16-mm (b) bars.

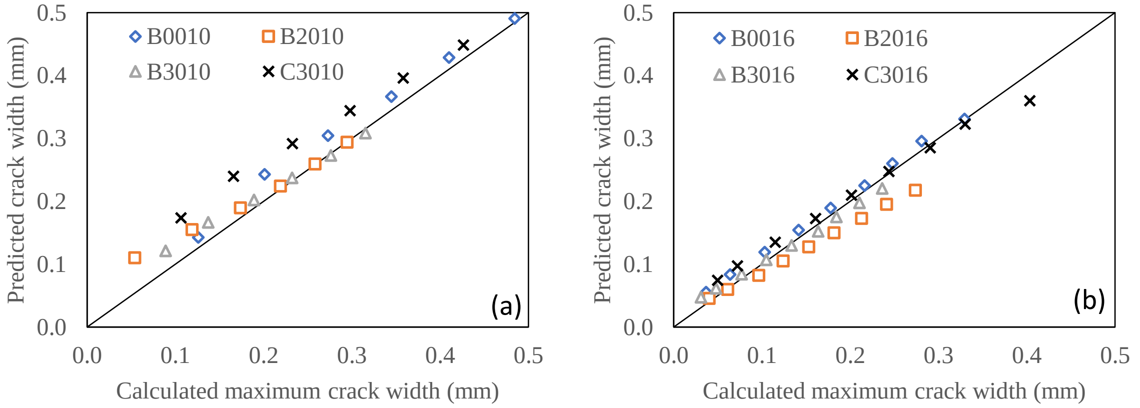

Figure 4.12 Maximum crack width predictions using the proposed approach and calculated from experimental strain values in R/FRC beams reinforced with 10-mm (a) and 16-mm (b) bars.

4.5.3 Effect of steel fibres

Figure 4.13 (a and b) shows the development of maximum crack width in R/FRC beams reinforced with 10-mm and 16-mm bars, respectively. As expected, fibres helped reduce the crack widths by up to 35% in beams reinforced with 10-mm diameter bars (ρ_s of 0.42%) and up to 30% in beams reinforced with 16-mm diameter bars (ρ_s of 1.1%). The larger amount of fibres, 30 kg/m^3, had more effect than 20 kg/m^3 in controlling crack widths in the beams reinforced with 16-mm diameter bars. This was not the case for the beams reinforced with 10-mm diameter bars, possibly due to the lower concrete strength in the beams with 30 kg/m^3. However, overall the fibres were relatively more effective at controlling cracks for the beams reinforced with 10-mm diameter bars, which had a lower reinforcement ratio (ρ_s of 0.42%). The reduction in crack width at service load was around 34% for the beams with ρ_s of 0.42%, whilst this was only 19% for the beams with ρ_s of 1.1%.

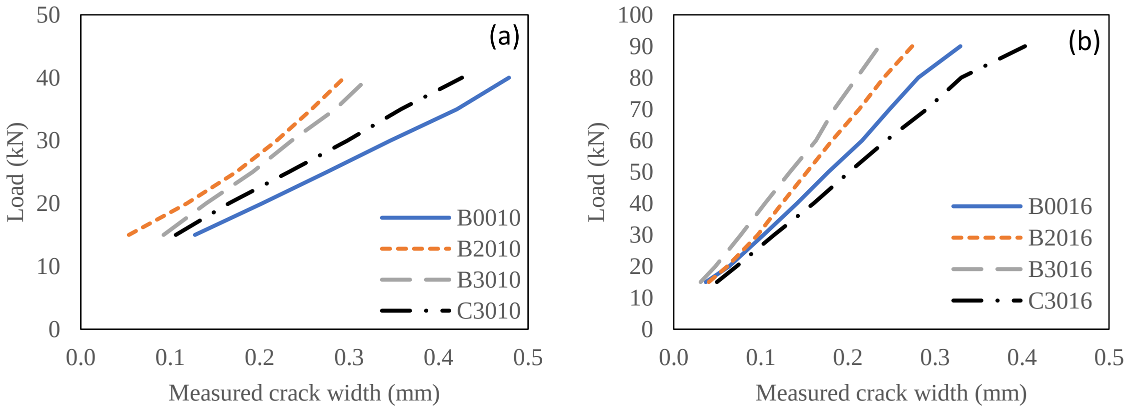

Figure 4.13 Effect of steel fibres in crack width propagation in R/FRC beams reinforced with 10-mm (a) and 16-mm (b) bars.

Increasing the cover from 20-mm to 40-mm, at a fixed dosage of fibre, increased the crack widths at service loads by about 23% and 51% for the beams with 10-mm and 16-mm diameter bar beams, respectively. In the beams with 40-mm cover, crack widths were 15% less in beams reinforced with 10-mm bars and 13% more in beams reinforced with 16-mm bars than the plain beams with 20-mm cover. It should be noted that the MC-2010 approach for predicting crack widths including fibres accounts well for the concrete cover once shrinkage is taken into account.

4.5.4 Influence of $\phi_s/\rho_{s,eff}$ and fibre

Figure 4.14 (a and b) shows the theoretical and experimental values of crack widths versus tensile stress in reinforcement. Beam B0010 with $\phi_s/\rho_{s,eff}$ value of 589 experienced wider cracks compared to beam B0016 with $\phi_s/\rho_{s,eff}$ value of 333 as normally the higher $\phi_s/\rho_{s,eff}$ value lead to higher transfer length and thus wider cracks. However, the addition of steel fibres increased tension stiffening and consequently reduced transfer length. The effect of fibre on tension stiffening and transfer length can be clearly seen in Figure 4.14a, where at SLS beam B2010 experienced a reduction in crack widths by about 49% compared to B2016 which experienced a reduction in crack widths by only 19%. The effect of fibres on transfer length and tension stiffening can be calculated from crack spacing in Figure 4.6. The addition of 20 kg/m^3 of steel fibre resulted in crack spacing reduction by 34% and 16% in beams with $\phi_s/\rho_{s,eff}$ value of 589 and 333, respectively. This indicates that the influence of 20 kg/m^3 of steel fibre on transfer length was greater than the influence of $\phi_s/\rho_{s,eff}$ value, similar influence can also be seen in Figure 4.14b. At $\phi_s/\rho_{s,eff}$ value of 589 (see Figure 4.15a), addition of 30 kg/m^3 of steel fibre resulted in crack width reduction at SLS by 33% and 48% in beams made with clear concrete cover of 20 mm and 40 mm, respectively. The same ratios were reduced to 24% and 39% when 30 kg/m^3 of steel fibre were added to beams made with $\phi_s/\rho_{s,eff}$ value of 333 (see Figure 4.15b). This indicates that the effect of fibres on transfer length and tension stiffening is more pronounced in beams made with higher $\phi_s/\rho_{s,eff}$ values and in beams made with bigger concrete covers.

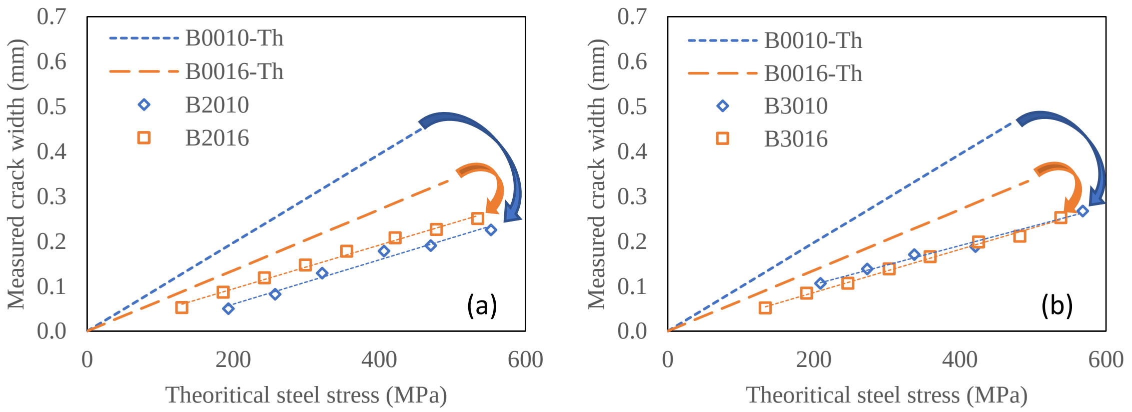

Figure 4.14 Effect of $\phi_s/\rho_{s,eff}$ values and fibres on maximum crack widths in beams made with 20 kg/m^3 (a) and 30 kg/m^3 (b) of steel fibre.

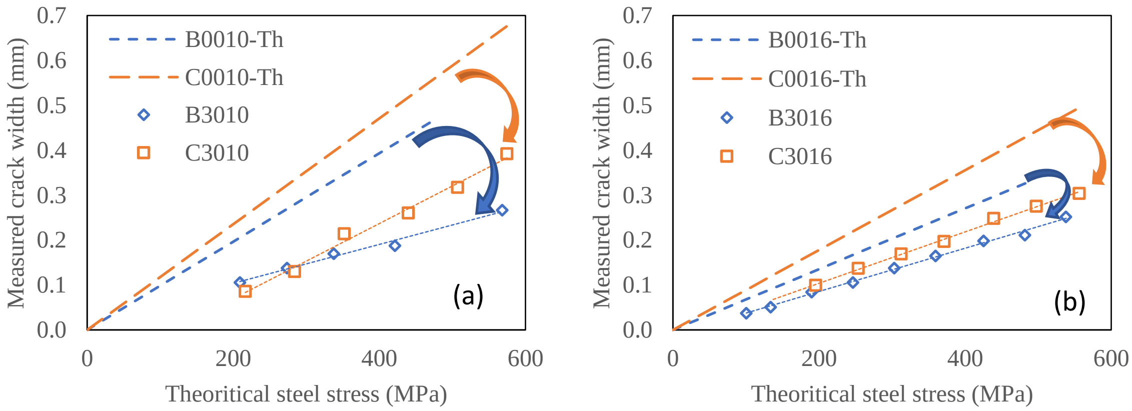

Figure 4.15 Effect of concrete cover and fibres on maximum crack widths in beams made with $\phi_s/\rho_{s,eff}$ values of 589 (a) and 333 (b).

4.6 Beam Deflections

Figure 4.16 and Figure 4.17 show the moment-deflection curves at mid span, up to yielding of reinforcement, in R/FRC beams reinforced with 10-mm and 16-mm bars, respectively. It is clear from both figures that the deflections exceed the response of the fully cracked beams. This can be attributed to shrinkage induced strains on the reinforcing bars before testing. The measured pre-loading shrinkage strains were removed by using the hybrid approach proposed by Kaklauskas et al (2017). The corrected deflections are in general lower than the expected deflections of the fully cracked sections in beams reinforced with 10-mm bars (Figure 4.16). However, this is not the case near the end of the test in beams reinforced with 16-mm bars (Figure 4.17), possibly due to additional non-flexural deformations. At service loads, the increase in deflections due to shrinkage strains was up to 32% and 22% in beams reinforced with 10-mm and 16-mm bars, respectively.

The additional non-flexural deformations (Figure 4.17) are most likely due to the observed development of the diagonal shear cracks beyond the bending moment of about 25 kN.m, which are normally ignored in the calculation of total deflection (Debernardi & Taliano, 2006). Such deformations are reported and quantified by Imjai et al (2016) who concluded that inclined cracks can increase the deflection by more than 1 mm. Beam B0016 had much higher deflections compared to the other beams due to the development of large shear cracks.

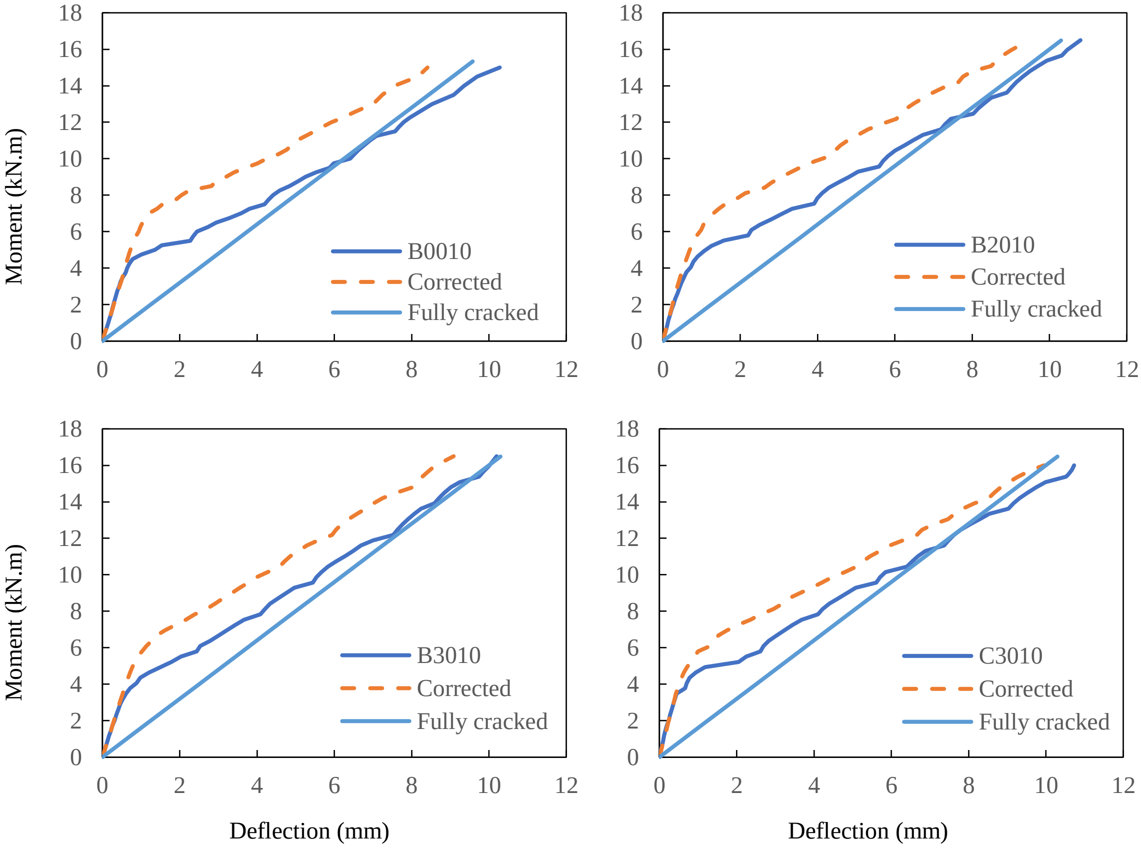

Figure 4.16 Deflection in R/FRC beams reinforced with 10-mm bars before and after shrinkage removal.

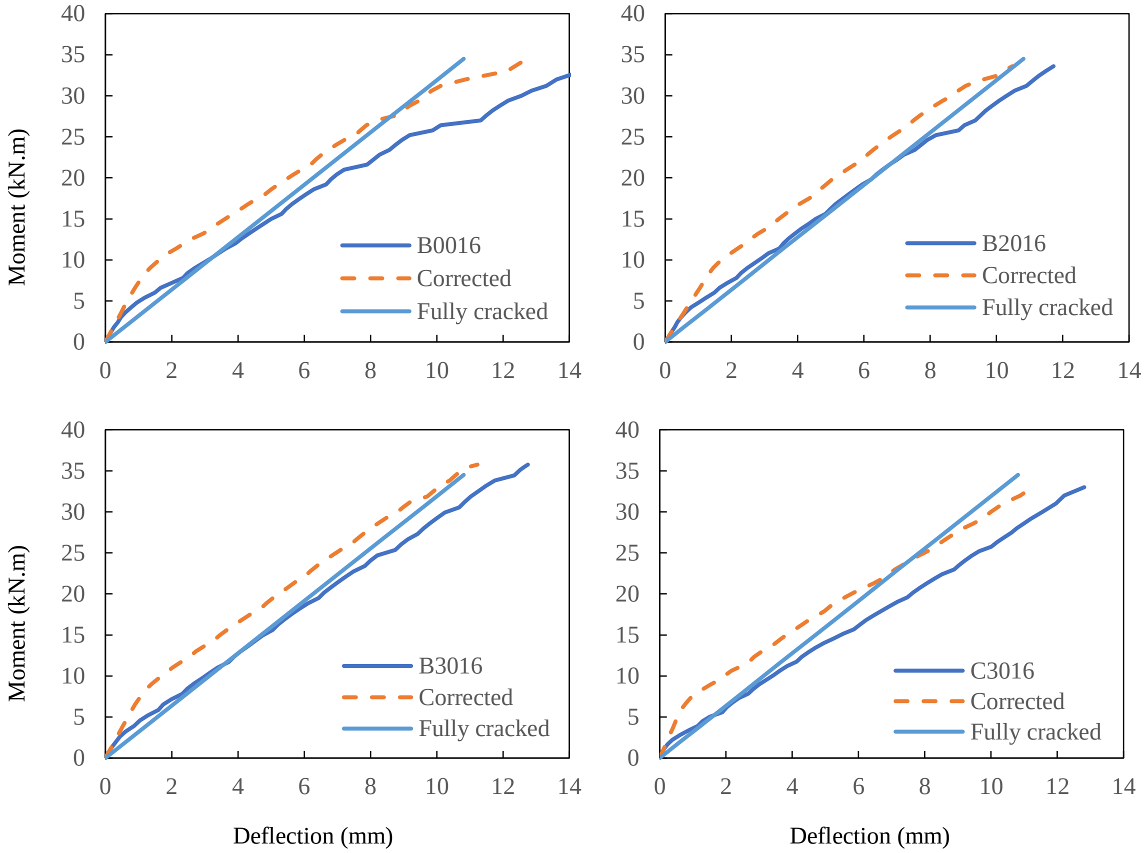

Figure 4.17 Deflection in R/FRC beams reinforced with 16-mm bars before and after shrinkage removal.

4.7 Conclusions

Crack width development is time dependent and therefore affected by several time dependent parameters. This study examined R/FRC beams reinforced with 10-mm and 16-mm bars and discussed the effect of shrinkage in crack widths predictions, using the approach by *fib* Model Code 2010, and deflection, using the hybrid approach developed by Kaklauskas et al (2017). Based on the findings, the following points can be summarized:

- Shrinkage strains are inevitable in RC elements and should be accounted for in short-term crack width and deflection calculations, including laboratory testing. In the examined medium scale elements, shrinkage strains can account for up to 20% of total strain at SLS in beams reinforced with steel ratio of 0.42%.

- A method is proposed to account for non-uniform shrinkage strains and curvatures in deflection and crack width calculations.
- The effect of fibres on reducing transfer length and increasing tension stiffening is more pronounced in beams made with higher $\phi_s/\rho_{s,eff}$ values and in beams made with bigger concrete covers.
- Steel fibres were found to be effective in reducing service load crack widths up to 34% in beams reinforced with steel ratio of 0.42%.
- Shrinkage strains and curvature can account for up to 32% of the deflections at service loads.

References

Al-Kamyani, Z., Guadagnini, M. & Pilakoutas, K., 2017. *Non-uniform drying shrinkage of RC elements with steel fibres.* Muscat, Whittles Publishing.

Beeby, A. W. & Scott, R. H., 2005. Cracking and deformation of axially reinforced members subjected to pure tension. *Magazine of Concrete Research,* 57(10), p. 611–621.

Bischoff, P. H., 2001. Effects of shrinkage on tension stiffening and cracking in reinforced concrete. *Can. J. Civ. Eng.,* 28(3), p. 363–374.

Debernardi, P. G. & Taliano, M., 2006. Shear deformation in reinforced concrete beams with thin web. *Magazine of Concrete Research,* 58(3), pp. 157-171.

Deng, P. & Matsumoto, T., 2017. Estimation of the Rebar Force in RC Members from the Analysis of the Crack Mouth Opening Displacement Based on Fracture Mechanics. *Advanced Concrete Technology,* Volume 15, pp. 81-93.

fib, 2008. *Bulletin 42 - Constitutive modelling of high strength/high performance concrete,* Lausanne, Switzerland: International Federation for Structural Concrete.

fib, 2013. *fib Model Code for Concrete Structures 2010,* Berlin, Germany: Wilhelm Ernst & Sohn.

Forth, J. P. et al., 2013. Verification of cracked section shrinkage curvature models. *ICE Structures and Buildings,* 167(5), pp. 274-284.

Goto, Y., 1971. Cracks Formed in Concrete Around Deformed Tension Bars. *ACI Journal,* 68(4), pp. 244-251.

Gribniak, V., Kaklauskas, G., Kliukas, R. & Jakubovskis, R., 2013. Shrinkage effect on short-term deformation behavior of reinforced concrete – When it should not be neglected. *Materials and Design,* Volume 51, pp. 1060-1070.

Gribniak, V. et al., 2012. Deriving stress–strain relationships for steel fibre concrete in tension from tests of beams with ordinary reinforcement. *Engineering Structures,* Volume 42, p. 387–395.

Groli, G., 2014. *Crack width control in RC elements with recycled steel fibres and applications to integral structures: theoritical and experimental study,* Madrid: Polytechnic University of Madrid.

Groli, G. & Caldentey, A. P., 2017. Improving cracking behaviour with recycled steel fibres targeting specific applications – analysis according to fib Model Code 2010. *fib Structural Concrete,* Volume 18, pp. 29-39.

Groli, G., Caldentey, A. P. & Soto, A. G., 2014. Cracking performance of SCC reinforced with recycled fibres – an experimental study. *fib Structural Concrete,* 15(2), pp. 136-153.

Hobbs, D. W., 1974. Influence of Aggregate Restraint on the Shrinkage of Concrete. *ACI Journal*, pp. 445-450.

Hoshino, M., 1989. Relation Between Bleeding, Coarse Aggregate, and Specimen Height of Concrete. *ACI Materials Journal,* 86(2), pp. 185-190.

Imjai, T., Guadagnini, M., Garcia, R. & Pilakoutas, K., 2016. A practical method for determining shear crack induced deformation in FRP RC beams. *Engineering Structures,* Volume 126, pp. 353-364.

Jeong, J.-H., Park, Y.-S. & Lee, Y.-H., 2015. Variation of Shrinkage Strain within the Depth of Concrete Beams. *Materials,* pp. 7780-7794.

Kaklauskas, G. & Ghaboussi, J., 2001. Stress-strain relations for cracked tensile concrete from RC beam tests. *Structural Engineering,* 127(1), pp. 64-73.

Kaklauskas, G., Ng, P. & Gribniak, V., 2017. *Eliminating shrinkage in tension stiffening model of concrete beams by the hybrid approach.* Perth, Taylor & Francis Group, London.

Martinelli, E., Caggiano, A. & Xargay, H., 2015. An experimental study on the post-cracking behaviour of Hybrid Industrial/Recycled Steel Fibre-Reinforced Concrete. *Construction and Building Materials,* Volume 94, pp. 290-298.

Micallef, M., 2015. *Crack control in base-restrained reinforced concrete walls,* London: Imperial College London.

Micallef, M., Vollum, R. L. & Izzuddin, B. A., 2017. Crack development in transverse loaded base-restrained reinforced concrete walls. *Engineering Structures,* Volume 143, pp. 522-539.

Nazmul, I. & Matsumoto, T., 2008a. High resolution COD image analysis for health monitoring of reinforced concrete structures through inverse analysis. *International Journal of Solids and Structures,* 45(1), p. 159–174.

Nazmul, I. M. & Matsumoto, T., 2008b. Regularization of inverse problems in reinforced concrete fracture. *Journal of Engineering Mechanics,* 134(10), pp. 811-819.

Tan, K.-H., Paramasivam, P. & Tan, K.-C., 1995. Cracking characteristics of reinforced steel fibre concrete beams under short- and long-term loadings. *Advanced Cement Based Materials,* 2(4), pp. 127-137.

Younis, K. H., 2014. *Restrained shrinkage behaviour of concrete with recycled materials,* Sheffield: The University of Sheffield.

Zanuy, C., Fuente, P. d. l. & Albajar, L., 2010. Estimation of parameters defining negative tension stiffening. *Engineering Structures,* Volume 32, pp. 3355-3362.

Chapter 5: Conclusions and Recommendations for Future Work

This chapter summarises the outcomes from all chapters and discusses the contribution of this study towards sustainability of urban cities and recommends some works for future research in the field.

5.1 Conclusions

The aim of this study was to contribute to the understanding of how shrinkage and fibres impact short- and long-term deflections and crack widths in RC structures so as to lead to better predictions that can enhance the durability and sustainability of urban infrastructure. In particular, the effect of steel fibre blends on shrinkage strain development and cracking behaviour was investigated in both free and restrained elements with different sizes and reinforcement configurations. The study utilised two recycled materials, GGBS and RTSF, to control drying shrinkage and crack widths. The following findings can be summarised.

5.1.1 Effect of fibre blends on shrinkage and mechanical performance

- The addition of GGBS can reduce the amount and rate of shrinkage by up to 35% compared to conventional Portland cement.
- The use of single type of fibres or blends of manufactured fibres and RTSF has similar impact on the development of shrinkage strain with no evidence of cracking for ten months under end restrained conditions.
- The flexural performance of mixes made with fibre blends is similar to that of mixes made with only manufactured fibres, even though the study may have some problems with alignments of manufactured fibre. This indicates that RTSF can replace manufactured fibres in part (up to 1/3). The stress-CMOD curves obtained from specimens (section of 100x100 mm) made with different blends of MUSF and RTSF are characterised by f_{Rk} ratios that satisfy the *fib* MC 2010 recommendations. Thus, based on the examined specimens, fibre blends can replace a percentage of the main reinforcement in concrete structures.

5.1.2 Non-uniform shrinkage and section curvature

- Shrinkage strains develop non-uniformly through the height of concrete section due to the non-uniform distribution of concrete constituents. Coarse aggregate tends to settle towards the bottom of the section due to their relative high density and vibration of fresh concrete and the centroid of section stiffness moves accordingly by about 3% to 5% of the total height.
- A new model has been developed to predict shrinkage induced curvature that accounts for the change in section stiffness due to the distribution of reinforcement and concrete constituents. The model predictions are in good agreement with experimental results, including curvatures of plain and symmetrically reinforced sections. The model has limitations when applied to asymmetric reinforced sections and to sections reinforced with both fibres and longitudinal bars. Unfortunately, this could not be justified due to the lake of experimental data in literature. The application of the model may remain limited to sections that are designed not to crack, like prestressed concrete.

5.1.3 Effect of fibre blends on crack widths

- Shrinkage strains were found to cause reduction in apparent measured tension stiffening and increase apparent curvatures.
  - The *fib* MC 2010 approach was used to predict crack spacing and width as it accounts for the contribution of fibres and long-term shrinkage. From a comparison with results of short-term laboratory tests, it is concluded that the effect of shrinkage should also be included in the calculations for short-term crack width prediction. In examined medium scale beams, shrinkage strains can account for up to 20% of total strain at SLS in beams reinforced with steel ratio of 0.42%.

- Non-uniform shrinkage was used to account for shrinkage strains in crack width predictions and a more accurate design equation, based on a modification of the *fib* Model Code 2010, is proposed.
- The addition of about 1% of blended steel fibres can reduce crack widths by more than 30% in RC elements with steel ratio of about 0.42%. It also found to reduce transfer length and increase tension stiffening, resulting in a crack width reduction by about 34%. Such reduction in crack width is expected to reduce: the amount of skin reinforcement; congestion of longitudinal bars in heavily reinforced sections; the potential of plastic cracking. It will also increase the quality of concrete cover and enhance self-healing, leading to more durable infrastructure.

5.2 Service Life Span Enhancement

The enhancement of service life span is an effective way of increasing the sustainability of critical infrastructure which is an important consideration for most governments around the world. Sustainability driven studies started a few decades ago and still maintain a high priority level due to the global concerns on the contribution of cement and concrete to global warming and the use of virgin materials. Thus, the need for reducing, reusing and recycling materials in construction is seen as paramount by all parties (governments, investors, engineers and end users) as it secures a more sustainable world.

This study in particular investigated several aspects that could help increase durability of reinforced concrete, which will help the sustainability of urban societies by direct and indirect approaches such as:

- Using ground granulated blast-furnace slag (GGBS) in concrete as a replacement for conventional cement (e.g. Portland cement) to reduce the emission of carbon dioxide (CO_2), utilising the waste itself in concrete instead of dumping it in the environment, reducing the rate and ultimate value of shrinkage strains that will decrease the potential of early age cracking and eventually, long-term crack widths. Similar benefits may have been obtained from the use of other by-products waste materials like fly ash, silica fume, etc with special care needs to be considered in autogenous shrinkage.

- Using fibre reinforced concrete (FRC) in controlling crack widths and spalling of concrete cover. It has been shown that randomly distributed fibres with dosage of about 1% are able to reduce crack widths by more than 30% compared to conventional reinforced concrete. This is expected to enhance self-healing of cracked concrete, reduce the potential of corrosion and protect the reinforcement from direct exposure to the environment. Such amounts of steel fibres were found to increase tension stiffening and reduce transfer length effectively, which will help in maintaining better control for deflections and will allow construction of long spans. FRC will also help in reducing the needed quantities of skin reinforcement, which normally cause congestion during the construction and can lead to quality control issues (i.e. minimum concrete cover, honeycomb, plastic shrinkage cracking).
- The use of recycled tyre steel fibres (RTSF) will help utilising the generated waste from post-consumer tyres and reduce the used energy in manufacturing and transporting new fibres. RTSF can also control crack widths and enhance self-healing.
- The development of the new model that calculates the shrinkage strains through the section more accurately. The model will help make better predictions for long-term deflections, especially in structures with long-span where excessive

deformations were reported in several parts of the world and were related to the underestimation of the effect of creep and shrinkage strains.

- Accounting for shrinkage strains in crack width prediction leads to more accurate predictions of both short- and long-term cracking and deflection and will help increase performance and reduce the maintenance costs of reinforced concrete structures.

There are several applications where such findings can be used such as retaining walls, elevator shafts, bridge decks, ducts, prestressed elements, precast elements, etc. Figure 5.1 shows a schematic representation of the main findings of this study and their impact on creating more sustainable societies.

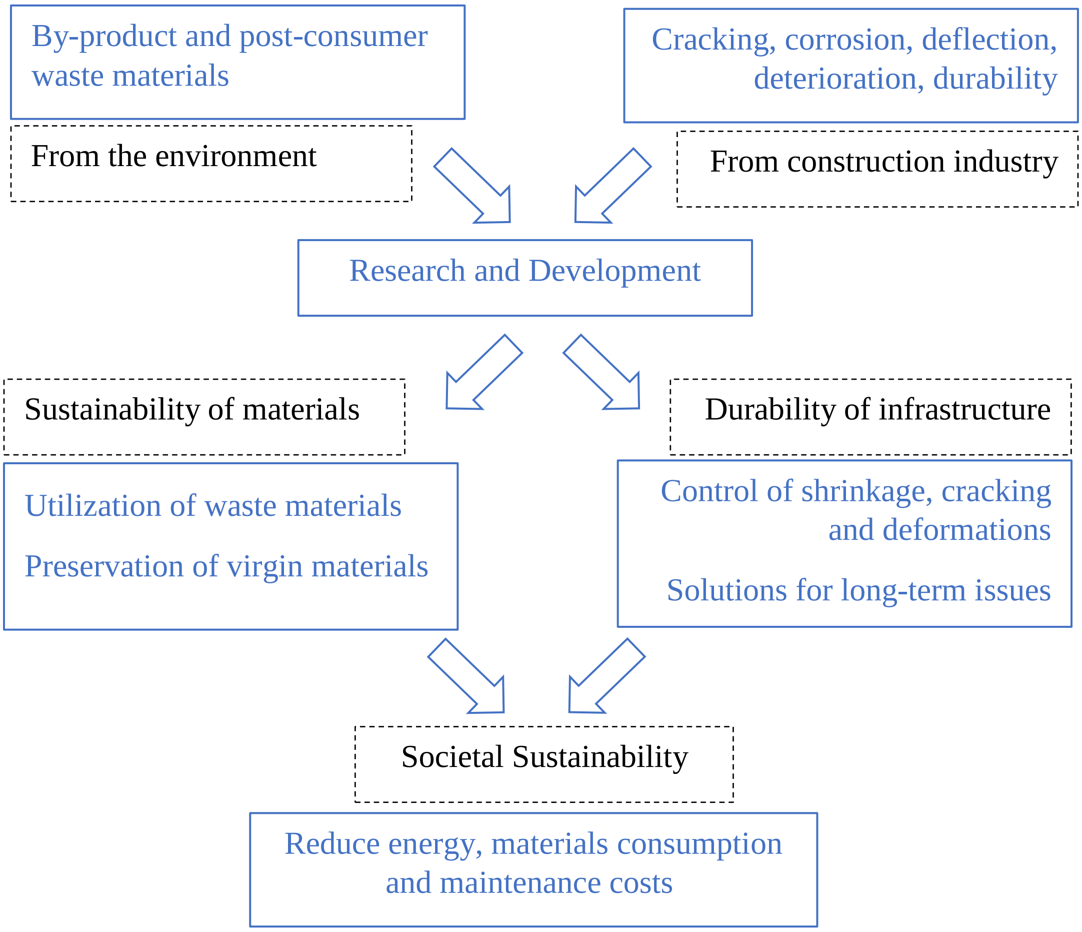

Figure 5.1 Schematic representation of the main findings of this study and their impact on creating more sustainable societies.

5.3 Recommendations for Future Work

Based on the investigation and findings of this study, the following issues should be further investigated:

- Quantification of the effect of supplementary cementitious materials (e.g. GGBS, fly ash and silica fume) on autogenous and drying shrinkage of concrete. Development of coefficients, guidelines or recommendations for design codes.
- Investigate and quantify the effect of fibres on self-healing.
- Effect of aggregate distribution on shrinkage induced curvature in beams with different dimensions (> 300 mm high) and cross-sectional shapes (T-beams, box sections). It would be also worth to investigate this effect when using different sizes and types of aggregates as well as of self-compacting concrete.
- Effect of different fibre dosages on the amount and distribution of coarse aggregates.
- Effect of fibres in the development of internal cracks around the reinforcement.

Appendix: A

This appendix presents more detailed photos and raw data for the experimental work described in Chapter 2 of the thesis.

Figure A.1 Restraining frame before casting.

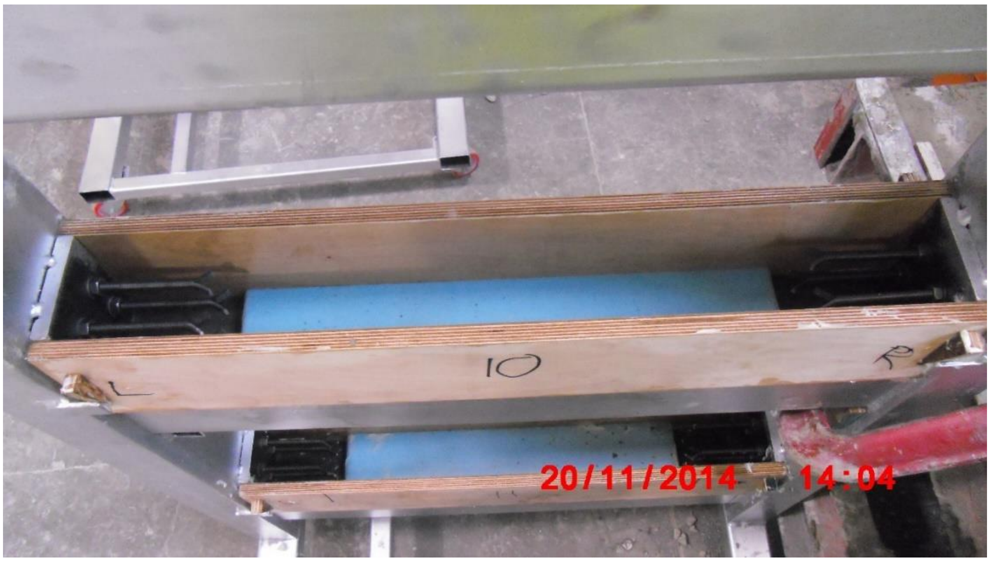

Figure A.2 Restraining frame before casting (inside mould).

Figure A.3 Free and restrained concrete elements after casting.

Figure A.4 Detailed locations of DEMEC discs in free and restrained concrete elements.

Table A.1 Free shrinkage records at top of prisms.

Age (days)	P13T	P18T	P20T	M30T	M20R10T	M20R10P1T	R30T	M35T	M45T	M35R10T
2	28	31	29	18	36	21	-5	4	28	55
3	56	74	58	50	82	48	39	36	43	82
4	123	103	76	75	114	96	70	86	99	120
5	190	153	119	124	137	151	105	118	123	168
6	234	175	127	189	176	184	149	192	185	185
8	316	197	170	218	201	251	187	222	226	209
10	385	213	212	261	244	293	236	271	259	261
14	406	291	237	287	292	336	267	302	297	286
28	549	376	309	364	366	410	367	379	374	376
42	586	405	360	369	423	464	400	411	387	413
56	607	431	378	409	432	501	425	436	413	443
70	662	444	391	449	458	512	442	466	444	475
84	634	465	419	436	469	542	468	473	443	480
98	680	476	414	456	480	545	473	492	464	483
112	705	498	421	478	494	555	483	513	489	497
154	734	515	440	492	517	584	516	529	503	524
182	731	531	454	496	529	592	521	518	501	541
208	739	521	454	490	519	593	514	530	513	538
266	735	514	447	491	520	580	512	531	494	530
300	748	518	448	504	516	565	499	525	500	516

Table A.2 Free shrinkage records at bottom of prisms.

Age (days)	P13B	P18B	P20B	M30B	M20R10B	M20R10P1B	R30B	M35B	M45B	M35R10B
2	14	19	-3	14	21	11	-14	8	10	24
3	28	21	-9	33	41	11	5	22	13	30
4	15	21	-3	52	68	51	23	53	67	83
5	17	31	13	102	91	76	40	76	84	141
6	24	33	9	159	143	98	73	141	141	166
8	74	39	31	186	168	151	105	168	186	198
10	86	38	69	223	214	180	142	207	212	263
14	58	82	74	252	271	208	163	230	248	305
28	133	124	126	322	338	249	230	275	310	396
42	133	127	154	319	391	292	253	302	317	436
56	141	143	161	355	397	317	261	320	335	465
70	170	159	171	397	427	322	284	343	358	500
84	125	167	187	375	434	350	302	342	363	505
98	172	173	185	393	446	358	304	358	385	512
112	197	184	190	412	455	360	310	378	404	525
154	206	213	211	425	478	389	336	390	398	548
182	204	208	214	428	485	391	340	379	404	571
208	214	210	212	425	475	385	331	395	417	569
266	187	190	199	416	470	363	315	375	402	554
300	195	184	193	426	463	349	304	377	402	538

Table A.3 Restrained shrinkage records at top of prisms.

Age (days)	M30T	M20R10T	M20R10P1T	R30T	M35T	M45T	M35R10T
2	15	23	17	13	8	19	35
3	40	45	29	50	23	39	38
4	47	66	73	77	65	78	71
5	84	78	97	100	74	89	113
6	144	113	109	132	132	138	123
8	159	130	155	155	151	171	135
10	183	158	176	193	165	189	177
14	203	189	196	212	194	201	188
28	251	231	212	266	209	249	234
42	237	267	241	288	220	233	245
56	251	256	255	290	225	239	252
70	276	278	242	302	237	252	268
84	255	275	258	322	227	243	266
98	258	280	261	314	233	260	266
112	273	282	264	323	251	276	268
154	285	299	275	348	247	262	283
182	283	298	279	336	236	264	293
208	268	292	271	328	245	269	293
266	257	272	248	312	220	246	261
300	243	266	241	305	204	232	247

Table A.4 Restrained shrinkage records at bottom of prisms.

Age (days)	M30B	M20R10B	M20R10P1B	R30B	M35B	M45B	M35R10B
2	2	24	15	11	-5	6	29
3	8	29	13	34	-7	14	18
4	4	34	50	46	13	44	38
5	32	30	65	67	3	50	62
6	85	56	74	93	54	92	61
8	93	71	110	109	71	123	68
10	106	92	129	140	77	129	95
14	127	106	135	153	95	133	94
28	159	135	142	199	92	165	126
42	134	162	161	213	100	151	130
56	145	151	171	214	104	157	137
70	177	169	162	226	112	168	154
84	149	165	180	241	104	151	143
98	156	165	183	242	114	176	140
112	181	171	181	243	133	193	140
154	185	184	191	262	124	176	160
182	187	184	194	255	112	182	165
208	168	177	189	249	126	184	166
266	154	156	159	229	89	158	132
300	142	147	153	222	77	145	116

Table A.5 Deformation records at the boundaries between concrete and restraining frame at top and bottom of prisms.

Age (days)	M20R10T	M20R10B	M20R10P1T	M20R10P1B	R30T	R30B	M35R10T	M35R10B
2	-	-	-22	-11	-27	-24	-	-
3	-	-	-124	-83	-144	-117	-	-
4	-164	-139	-221	-163	-266	-194	-179	-120
5	-228	-158	-323	-251	-378	-299	-250	-162
6	-334	-259	-394	-304	-450	-378	-322	-198
8	-402	-323	-448	-344	-550	-470	-397	-270
10	-479	-364	-509	-382	-619	-535	-492	-319
14	-606	-462	-613	-458	-709	-606	-603	-431
28	-717	-532	-697	-530	-822	-710	-701	-486
42	-786	-598	-748	-565	-910	-776	-746	-508
56	-815	-626	-781	-577	-941	-795	-761	-537
70	-814	-618	-782	-581	-967	-830	-784	-545
84	-846	-647	-788	-579	-964	-829	-797	-557
98	-839	-636	-786	-572	-971	-819	-805	-538
112	-860	-662	-811	-603	-1015	-869	-833	-579
154	-863	-659	-808	-603	-1015	-868	-826	-569
182	-852	-649	-777	-581	-1008	-850	-796	-556
208	-857	-647	-795	-583	-1002	-860	-807	-541
266	-895	-682	-854	-628	-1088	-926	-867	-598
300	-911	-686	-826	-611	-1068	-910	-850	-587

Table A.6 Average autogenous shrinkage strains in plain FRC prisms.

Age (days)	M30	M35	M45	M20R10	M35R10	R30	M20R10P1	P
2				16	25	0	0	15
3				16	25	4	2	6
4				-49	-10	8	1	1
5				-5	5	-8	-15	-3
6				-13	-2	2	-30	-1
8				-8	-2	-63	-65	-20
10				-60	-35	-60	-64	-28
14	-43	-42	-35	-53	-51	-79	-82	-45
28	-37	-27	-31	-53	-59	-49	-53	-30
42	-63	-57	-68	-73	-72	-70	-83	-40
56	-82	-71	-79	-95	-96	-41	-47	-38
70	-72	-66	-71	-69	-69	-37	-56	-36
84	-64	-41	-59	-70	-72	-53	-48	-35
112	-59	-50	-45	-80	-79	-50	-47	-46
154	-53	-43	-50	-73	-77	-47	-61	-37
208	-80	-60	-80	-57	-73	-64	-63	-51
266	-72	-59	-63	-84	-89	-81	-80	-64
322	-73	-70	-82	-94	-99	-81	-79	-72

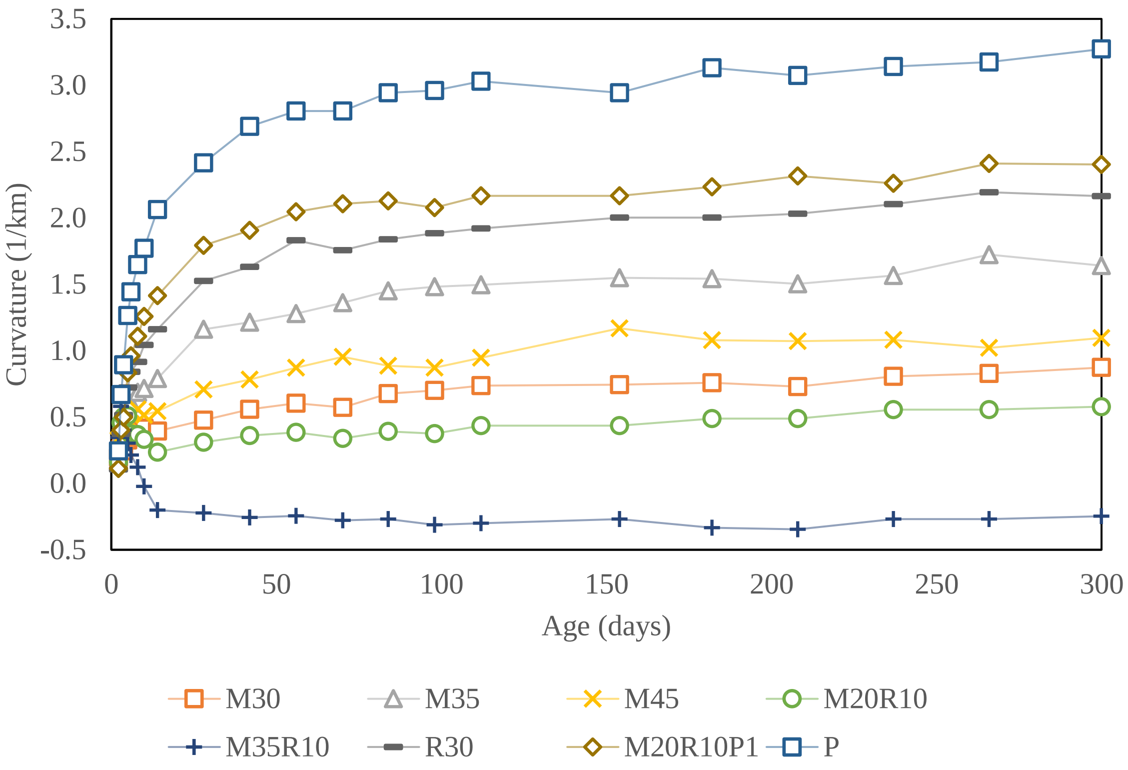

Figure A.5 Free shrinkage induced curvature in plain and SFRC prisms.

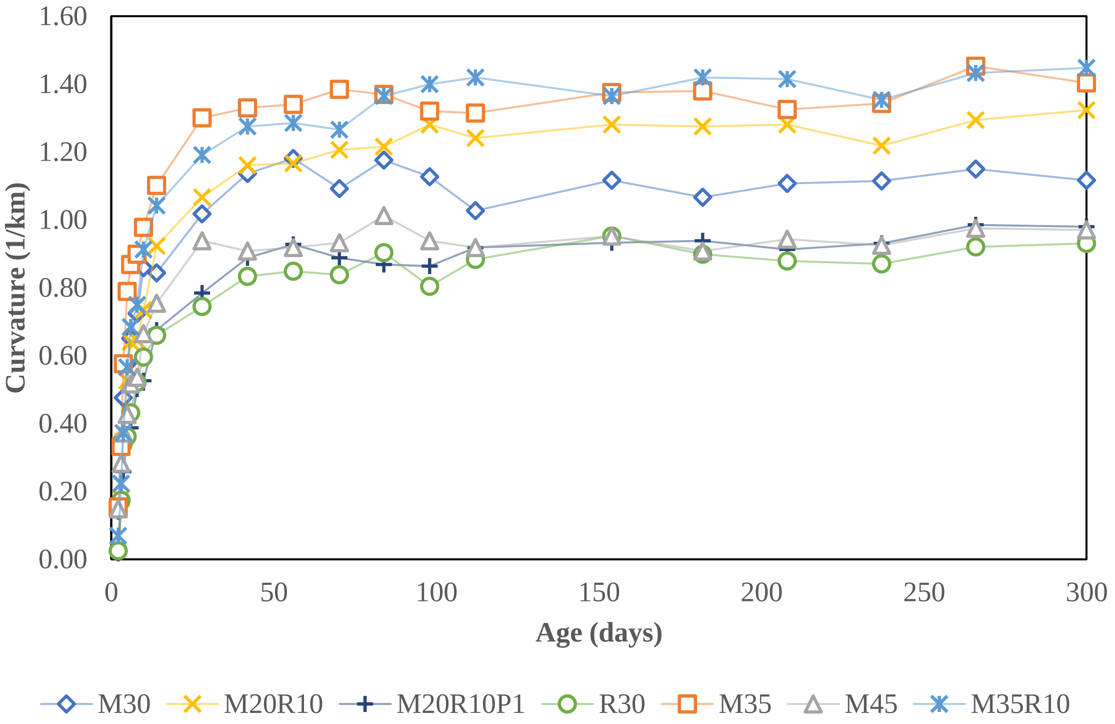

Figure A.6 Restrained shrinkage induced curvature in SFRC prisms.

Forces on Restraining Frame

An example of calculations used to assess shrinkage induced forces on the restraining frame is shown below. The experimental shrinkage values obtained for specimen M20R10P1 are used to estimate the relative fictitious forces at age of 300 days. At this age, the specimens have reached hygral stabilisation and the relative deformation between concrete and frame can be considered to be approximately stabilised. Therefore, the shrinkage induced force can be assumed to be 100% resisted by the anchors.

At age of 300 days:

Average shrinkage on Top prism: 246 με

Average shrinkage on Middle prism: 192 με

Average shrinkage on Bottom prism: 204 με

The concrete elastic modulus was obtained from compressive strength using Eurocode 2, average compressive strength was 26.3 MPa and the corresponding average E_c was 29400 MPa.

Cross sectional area of concrete: 100x100 mm

Corresponding fictitious shrinkage induced forces were calculated using elastic principle ($\varepsilon_{sh}E_cA_c$). Since each force will be resisted by the two sides of steel frame, each side of the steel frame will be subjected to half of this force that results in the following forces:

Average force applied to anchors holding Top prism: 36.1 MPa

Average force applied to anchors holding Middle prism: 28.2 MPa

Average force applied to anchors holding Bottom prism: 30.0 MPa

These forces were then applied to the anchors in FEA.

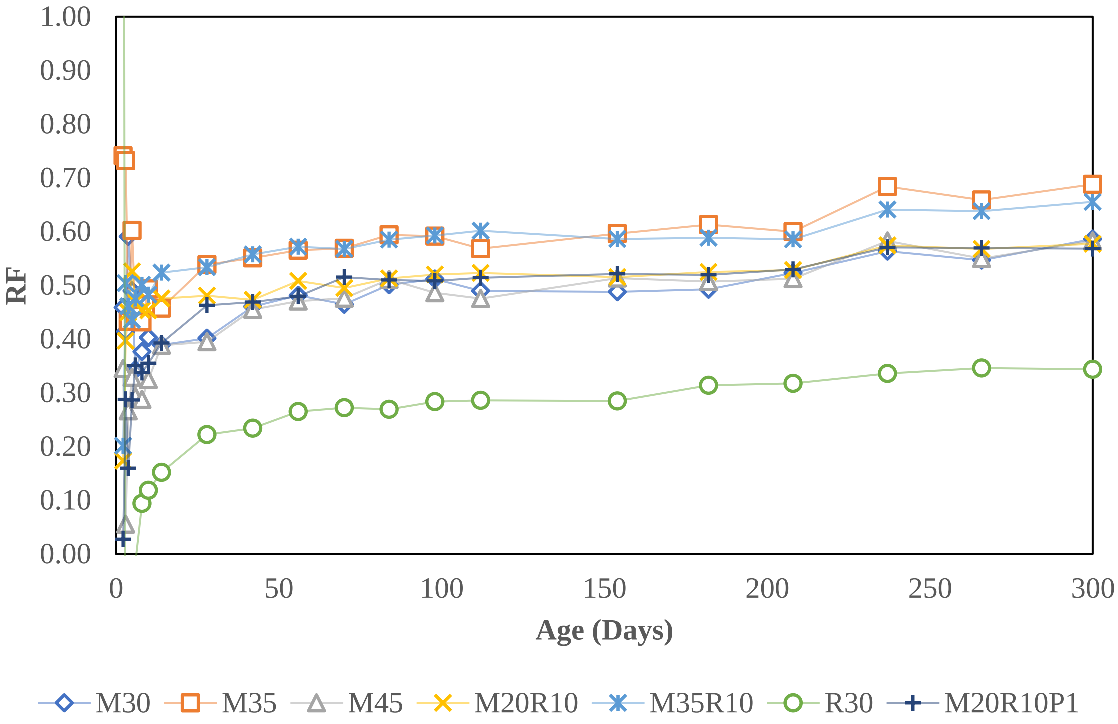

Figure A.7 Restraining factor for the used rigid steel frame.

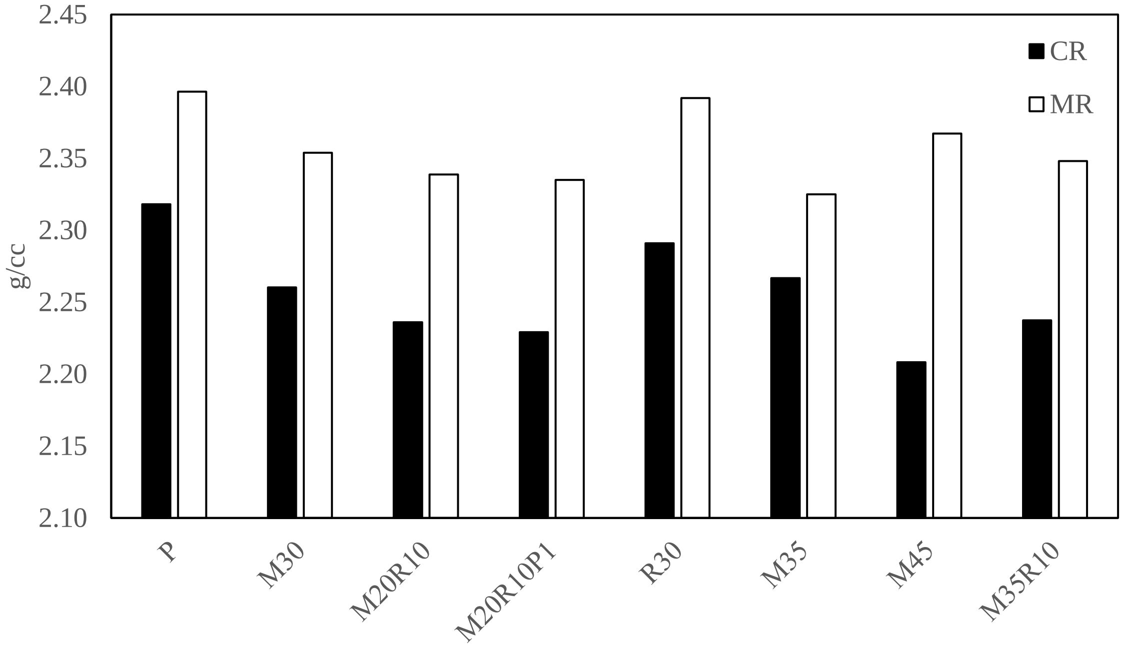

Figure A.8 Density of plain concrete and SFRC mixes cured in control and mist room.

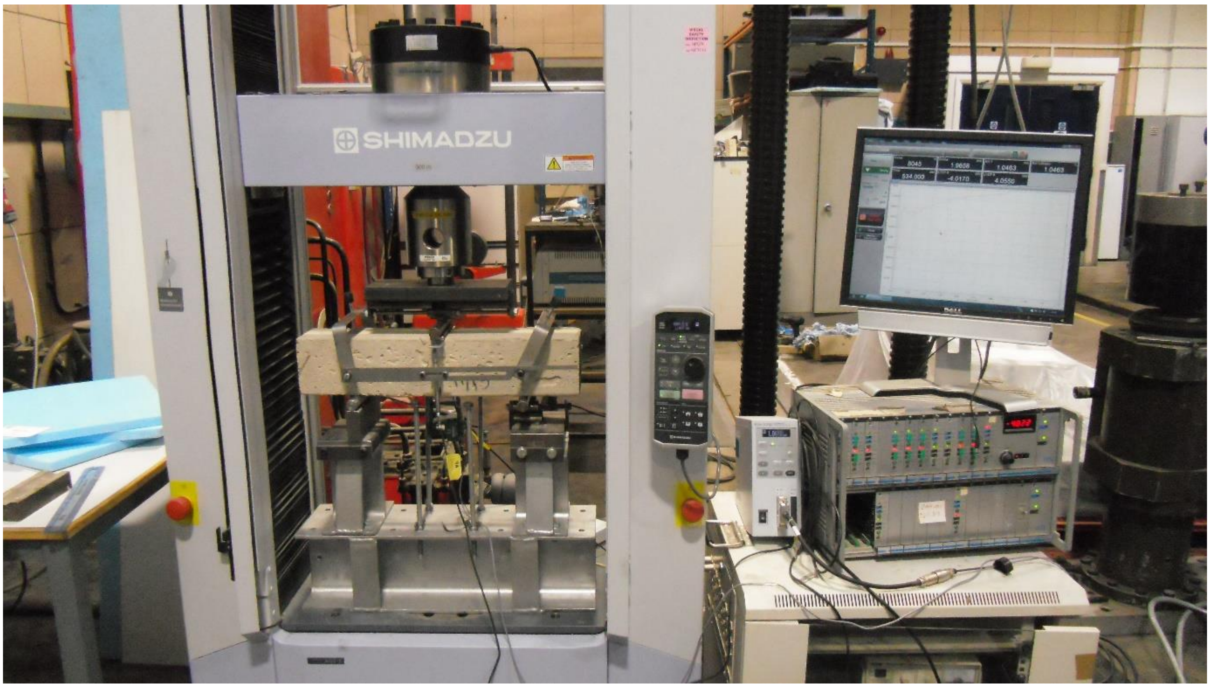

Figure A.9 Testing of SFRC prisms under three-point bending.

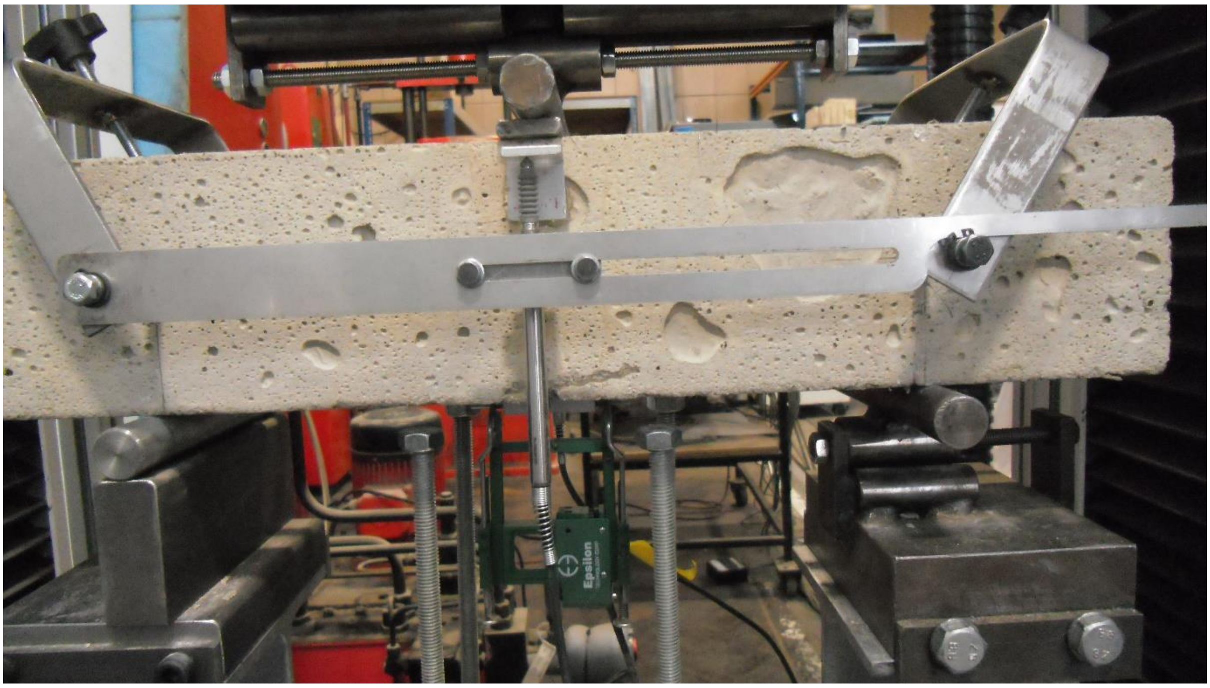

Figure A.10 Testing of SFRC prisms under three-point bending (closer view).

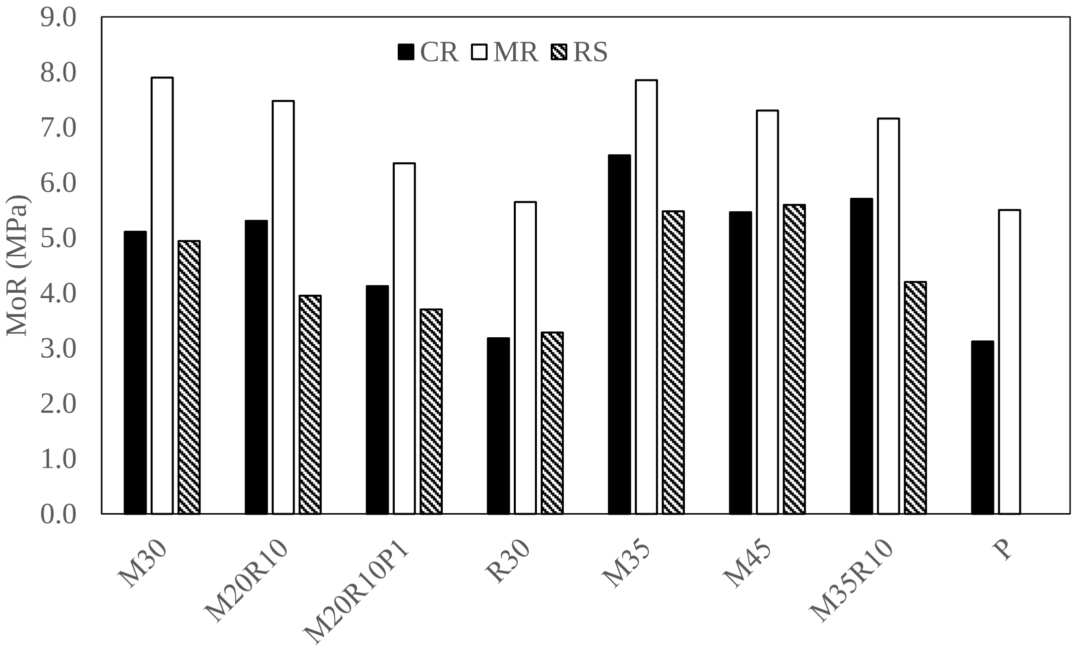

Figure A.11 Modulus of rupture for SFRC made with different blends of MUSF and RTSF conditioned under control room, mist room and restrained frame.

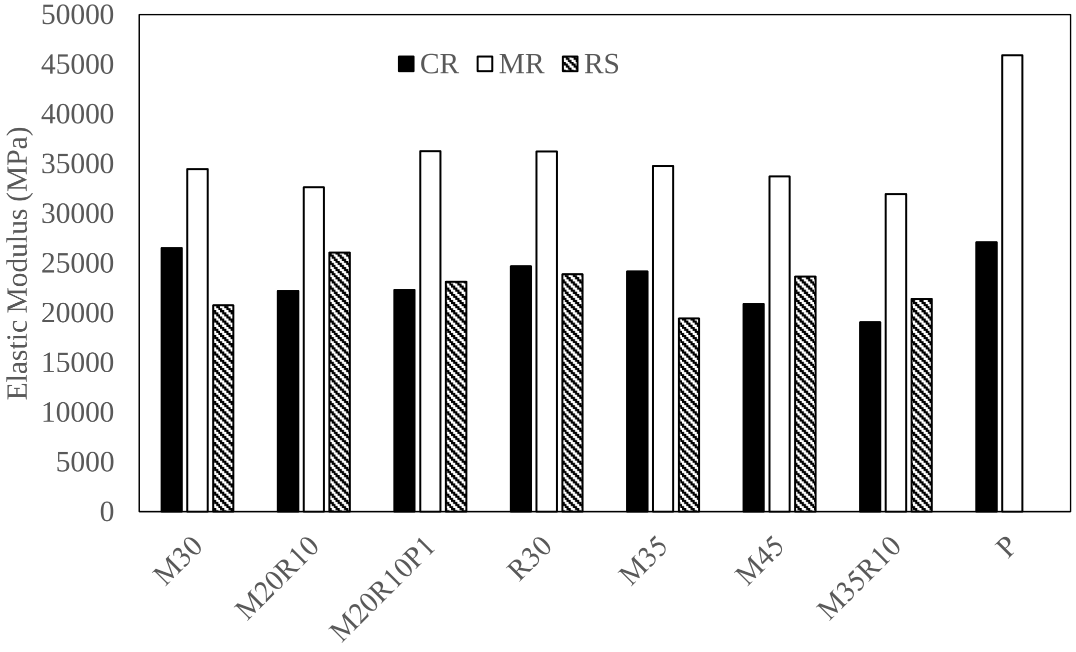

Figure A.12 Elastic modulus for SFRC made with different blends of MUSF and RTSF conditioned under control room, mist room and restrained frame.

Appendix: B

This appendix presents more detailed photos and raw data for the experimental work described in Chapter 3 of the thesis.

Figure B.1 moulds before casting.

Figure B.2 Moulds after casting.

Figure B.3 Plain and reinforced concrete specimens after demoulding.

Figure B.4 Distribution of DEMEC discs on beams and prisms.

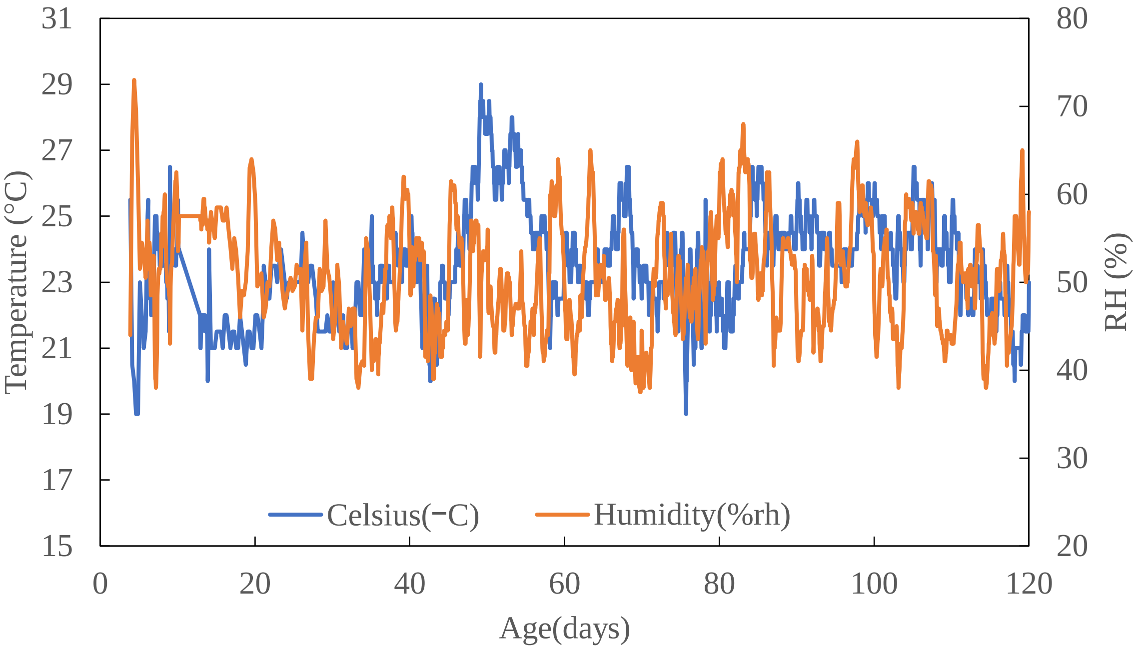

Figure B.5 Records of ambient temperature and relative humidity during shrinkage measurement period.

Figure B.6 Used USB device to record ambient temperature and relative humidity during shrinkage measurement period.

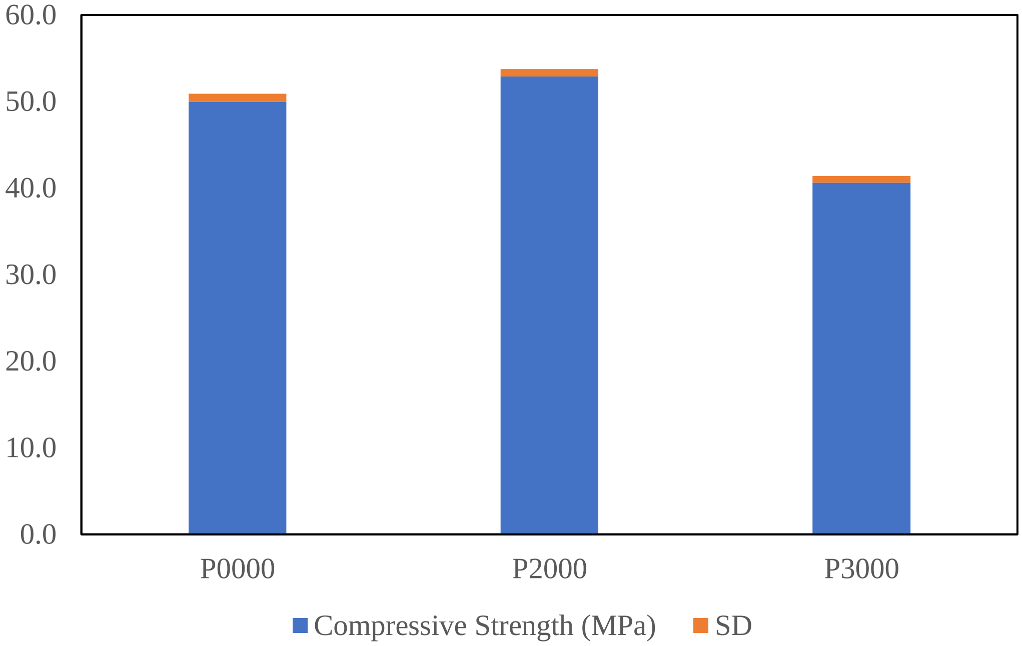

Figure B.7 Average compressive strength of plain and SFRC tested at 28 days.

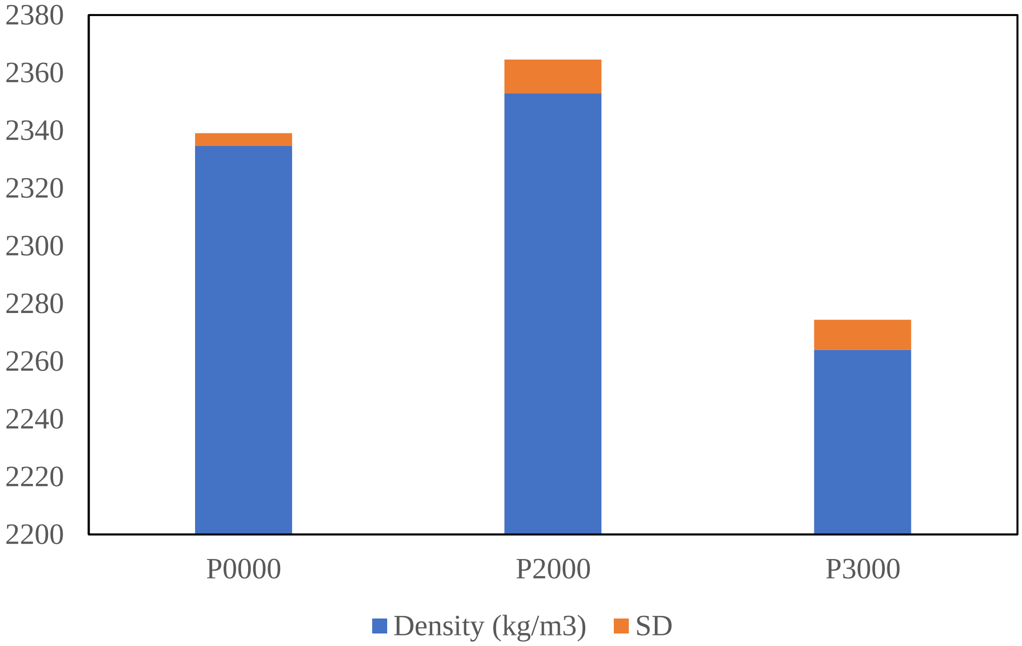

Figure B.8 Average density of plain and SFRC tested at 28 days.

Table B.1 Free shrinkage records at top (-T) and bottom (-B) of plain and SFRC prisms along with predictions of Model Code 2010 (MC).

Age	P0000-T	P0000-B	P2000-T	P2000-B	P3000-T	P3000-B	MC
6	-7	0	-14	18	-27	27	61
8	49	56	19	52	1	62	102
10	114	93	103	103	89	112	143
14	171	125	149	134	156	158	179
21	222	160	193	171	197	197	220
35	320	235	282	245	301	289	286
50	385	288	337	294	365	342	340
63	425	314	381	332	411	384	372
78	463	351	413	362	430	398	403
92	474	357	426	373	451	421	428
106	493	376	448	393	484	451	442
120	516	396	464	408	487	456	465

Table B.2 Shrinkage records at top (-T), bar level (-Bb) and bottom (-B) of plain and SFRC prisms reinforced with 10-mm bars.

Age	P0010-T	P0010-Bb	P0010-B	P2010-T	P2010-Bb	P2010-B	P3010-T	P3010-Bb	P3010-B
6	20	5	-1	-17	2	11	40	23	21
8	86	54	46	30	49	50	84	55	48
10	129	87	81	98	103	96	140	104	89
14	177	119	106	144	136	125	194	145	120
21	224	155	142	184	160	149	244	174	142
35	321	220	197	270	226	211	346	240	194
50	384	267	237	328	269	249	405	282	224
63	423	283	249	371	301	277	457	309	243
78	470	311	276	399	321	297	487	329	263
92	473	314	277	418	332	306	496	329	262
106	502	332	289	440	349	324	516	345	276
120	517	341	297	456	358	334	536	360	288

Table B.3 Shrinkage records at top (-T), bar level (-Bb) and bottom (-B) of plain and SFRC prisms reinforced with 16-mm bars.

Age	P0016-T	P0016-Bb	P0016-B	P2016-T	P2016-Bb	P2016-B	P3016-T	P3016-Bb	P3016-B
6	-8	-6	-10	13	16	14	40	19	10
8	48	42	41	63	45	32	97	62	48
10	104	78	73	116	84	70	146	99	87
14	157	102	91	154	106	86	191	119	100
21	217	129	107	194	125	101	246	145	115
35	328	167	128	281	169	134	347	178	131
50	398	197	148	336	208	159	412	207	151
63	440	203	140	381	223	172	442	205	139
78	482	218	152	408	234	177	474	216	147
92	494	216	146	421	236	178	484	216	142
106	515	226	154	441	250	188	503	231	153
120	536	231	157	460	257	192	520	233	154

Table B.4 Shrinkage records at level of top bar (-Tb), bottom bar (-Bb), and top (-T) and bottom (-B) for beam C3010, of plain and SFRC beams reinforced with 10-mm bars.

Age	B0010-Tb	B0010-Bb	B2010-Tb	B2010-Bb	B3010-Tb	B3010-Bb	C3010-T	C3010-B	C3010-Tb	C3010-Bb
6	-19	12	14	-3	14	3	18	4	15	6
8	25	65	46	23	63	47	70	48	63	48
10	88	85	91	57	95	74	107	74	100	78
14	119	97	118	66	133	102	132	80	122	90
21	156	123	156	88	171	125	175	114	163	121
35	244	192	236	152	260	205	259	182	245	193
50	300	240	292	197	315	253	328	235	316	245
63	335	262	321	211	348	275	359	253	344	266
78	360	282	345	230	371	295	386	271	371	284
92	381	300	355	230	377	294	394	272	377	287
106	414	330	385	266	413	331	425	301	409	318
120	421	333	390	262	404	324	431	299	413	317

Table B.5 Shrinkage records at level of top bar (-Tb), bottom bar (-Bb), and top (-T) and bottom (-B) for beam C3010, of plain and SFRC beams reinforced with 16-mm bars.

Age	B0016-Tb	B0016-Bb	B2016-Tb	B2016-Bb	B3016-Tb	B3016-Bb	C3016-T	C3016-B	C3016-Tb	C3016-Bb
6	4	-5	-29	-5	5	-7	-27	8	-25	-1
8	52	36	-3	30	40	21	13	51	16	41
10	83	62	67	56	77	50	81	75	79	68
14	97	71	95	62	99	66	110	71	106	75
21	117	86	125	79	128	87	147	90	138	89
35	184	144	194	133	196	139	214	135	204	139
50	224	180	240	175	241	180	274	165	263	171
63	244	197	255	182	254	187	306	178	295	186
78	258	209	266	190	261	191	317	179	304	189
92	267	218	267	188	260	190	319	176	305	183
106	289	241	292	217	285	216	344	200	331	206
120	285	233	289	212	280	210	344	192	328	201

Table B.6 Shrinkage induced curvature in plain and SFRC prisms reinforced with 10-mm and 16-mm rebars.

Age	P0000	P0010	P0016	P2000	P2010	P2016	P3000	P3010	P3016
6	-0.06	0.17	0.01	-0.24	-0.21	-0.01	-0.42	0.15	0.23
8	-0.05	0.31	0.05	-0.25	-0.16	0.24	-0.47	0.28	0.38
10	0.17	0.37	0.24	0.00	0.02	0.36	-0.18	0.40	0.45
14	0.36	0.54	0.51	0.11	0.15	0.52	-0.01	0.57	0.69
21	0.48	0.63	0.85	0.17	0.27	0.71	0.00	0.78	1.01
35	0.65	0.96	1.53	0.28	0.46	1.12	0.09	1.17	1.66
50	0.74	1.13	1.92	0.33	0.60	1.36	0.18	1.40	2.00
63	0.86	1.34	2.31	0.38	0.73	1.61	0.21	1.64	2.33
78	0.87	1.49	2.54	0.39	0.78	1.78	0.24	1.72	2.51
92	0.90	1.50	2.67	0.41	0.86	1.88	0.23	1.80	2.63
106	0.90	1.64	2.77	0.42	0.89	1.95	0.25	1.84	2.70
120	0.92	1.69	2.92	0.43	0.94	2.06	0.24	1.91	2.82

Table B.7 Shrinkage induced curvature in plain and SFRC beams reinforced with 10-mm and 16-mm rebars.

Age	B0010	B0016	B2010	B2016	B3010	B3016	C3010	C3016
6	-0.15	0.06	0.09	-0.15	0.04	0.05	0.09	-0.15
8	-0.20	0.10	0.10	-0.18	0.05	0.09	0.11	-0.17
10	0.00	0.11	0.15	0.00	0.06	0.12	0.17	0.02
14	0.10	0.14	0.23	0.10	0.11	0.14	0.24	0.15
21	0.14	0.16	0.28	0.16	0.16	0.18	0.28	0.22
35	0.23	0.21	0.34	0.21	0.20	0.24	0.36	0.30
50	0.27	0.24	0.38	0.22	0.21	0.26	0.42	0.44
63	0.33	0.27	0.44	0.26	0.25	0.29	0.46	0.52
78	0.35	0.27	0.46	0.27	0.28	0.29	0.51	0.56
92	0.36	0.27	0.51	0.28	0.32	0.30	0.54	0.57
106	0.38	0.26	0.46	0.26	0.31	0.29	0.54	0.59
120	0.40	0.29	0.51	0.27	0.29	0.30	0.59	0.61

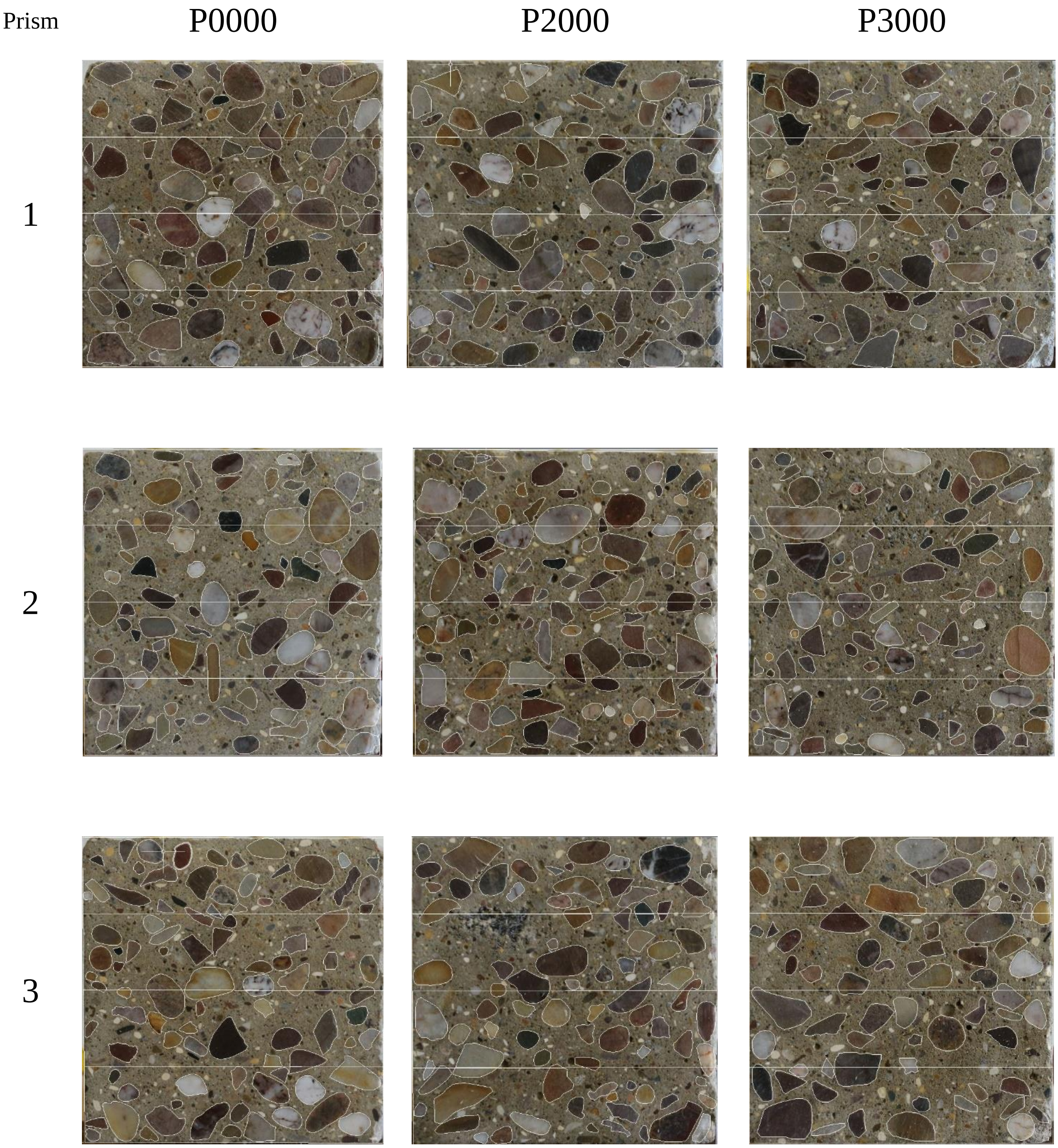

Figure B.9 Aggregates distribution in plain and SFRC prisms.

Table B.8 Raw data of aggregates distribution in plain and SFRC prisms.

Prism	P0000-1	P0000-2	P0000-3	P2000-1	P2000-2	P2000-3	P3000-1	P3000-2	P3000-3
Total Aggregate (mm^2)	9589	8578	8465	8292	8542	8070	7567	7231	8484
Total Section Area (mm^2)	23180	23191	23285	22174	22697	22750	22754	22931	22825
Top Aggregate %	46.1	47.0	47.8	47.6	50.5	50.3	52.5	50.5	50.5
Bottom Aggregate %	53.9	53.0	52.2	52.4	49.5	49.7	47.5	49.5	49.5
Total Aggregate %	41.4	37.0	36.4	37.4	37.6	35.5	33.3	31.5	37.2
Q1%	35.5	35.0	36.1	32.5	35.7	42.6	32.5	30.5	39.5
Q2%	40.9	34.4	33.1	38.5	40.5	28.7	37.2	33.2	35.6
Q3%	44.8	41.6	32.6	40.3	38.9	34.7	30.6	33.5	39.7
Q4%	44.2	36.9	43.6	38.4	35.4	35.9	32.8	29.0	33.9

Appendix: C

This appendix presents more detailed photos and raw data for the experimental work described in Chapter 4 of the thesis.

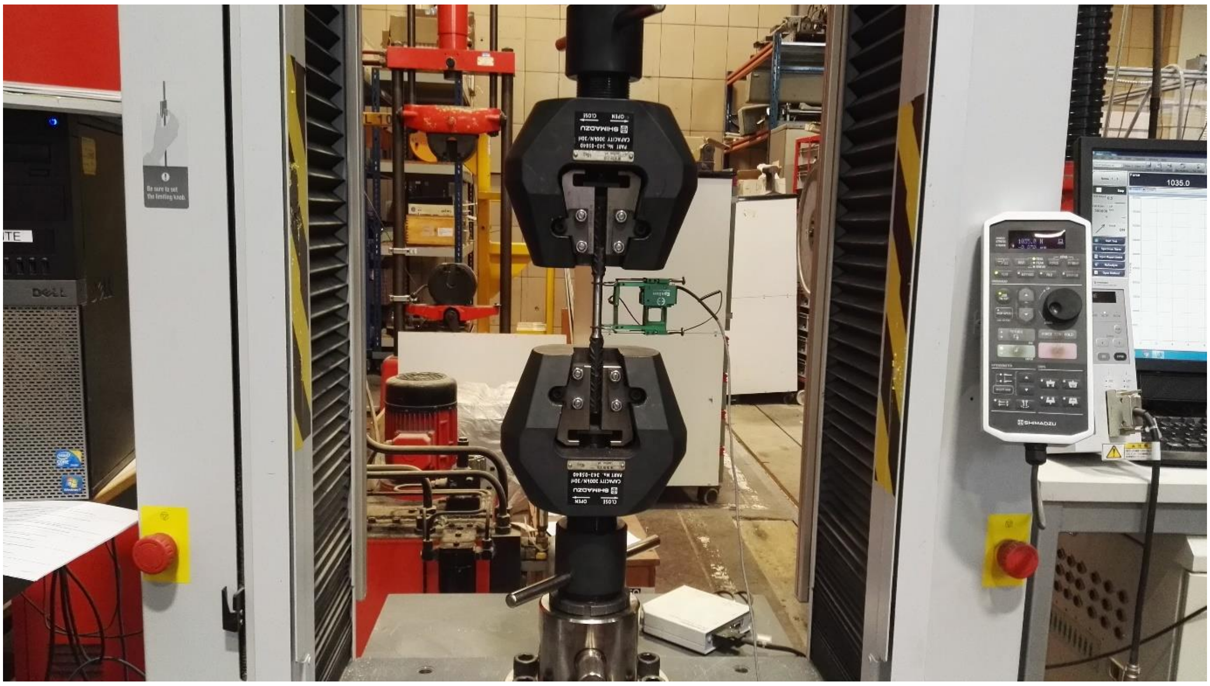

Figure C.1 Testing of steel bars.

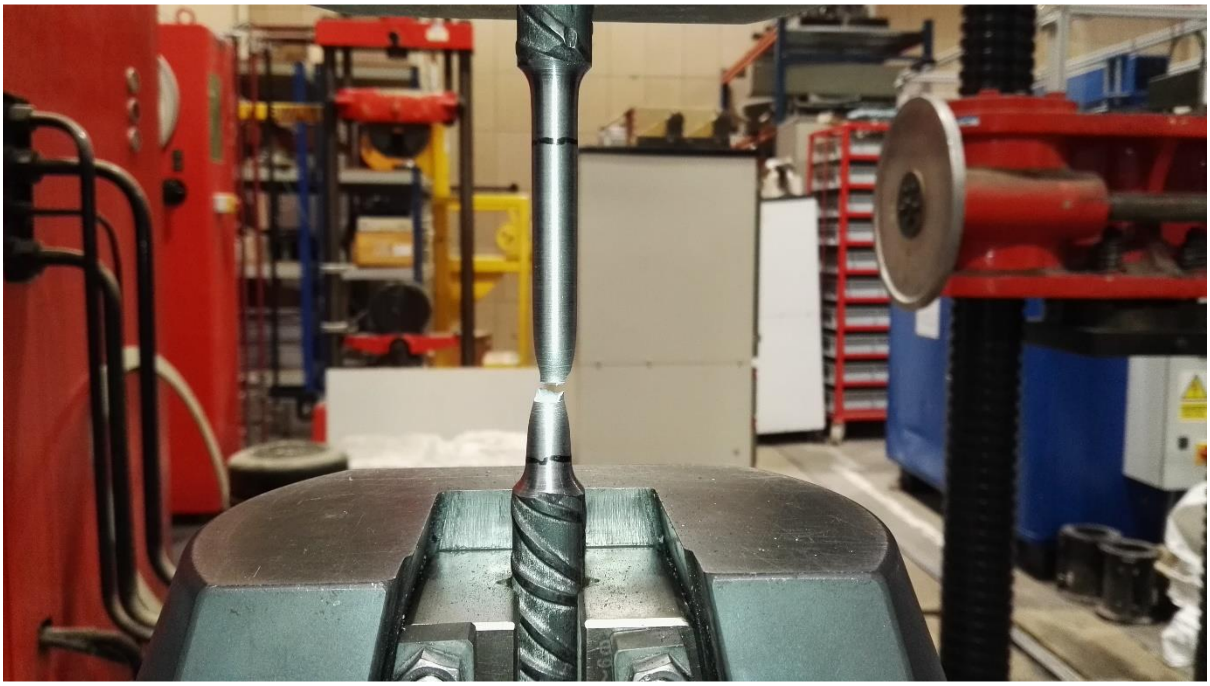

Figure C.2 Typical fracture of steel bars.

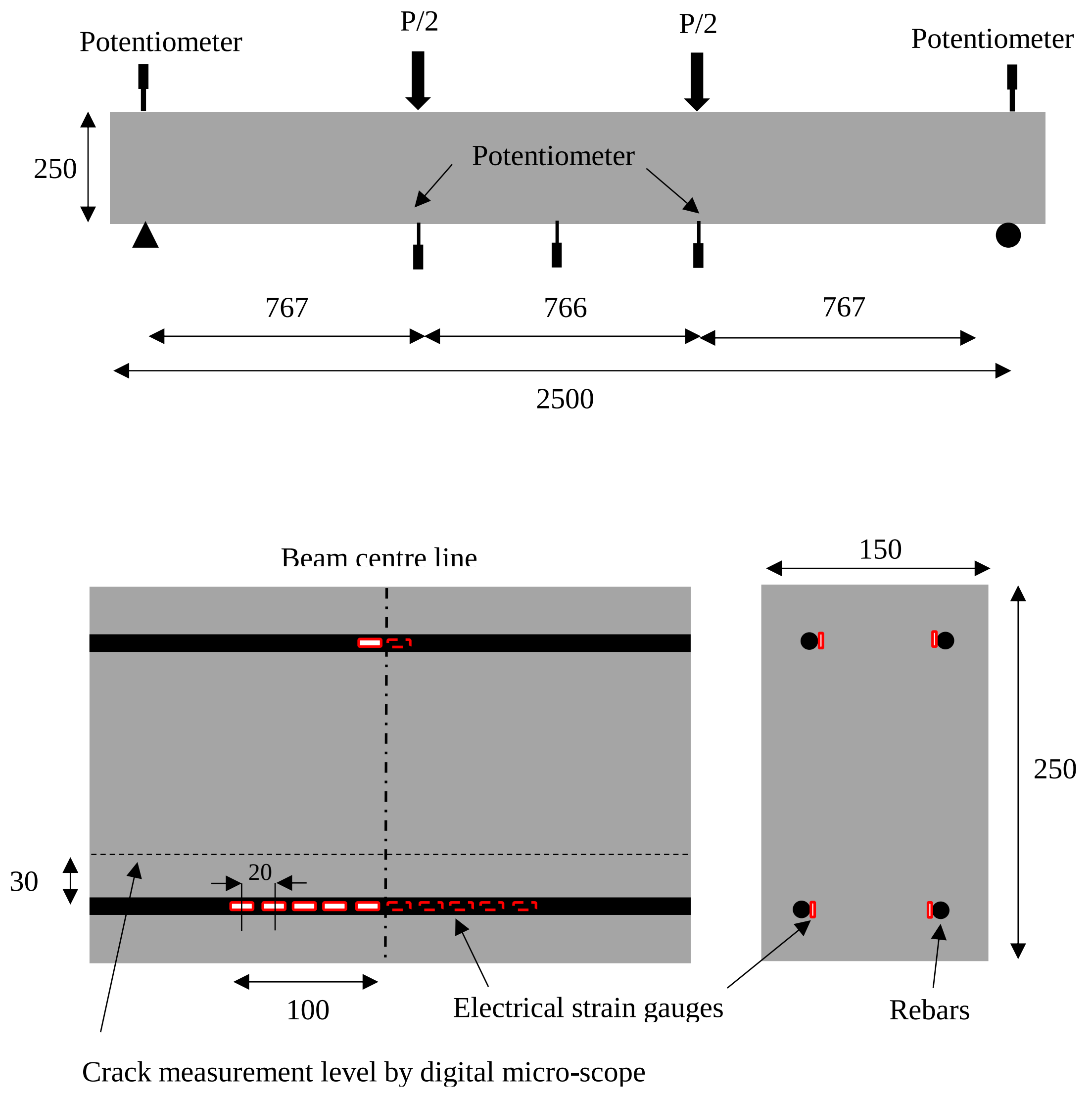

Not to scale, all dimensions are in *mm*

Figure C.3 Beam typical loading layout, cross section details and distribution of strain gauges and potentiometers.

Figure C.4 Testing and metal straps arrangements for all beams reinforced with 10-mm rebars.

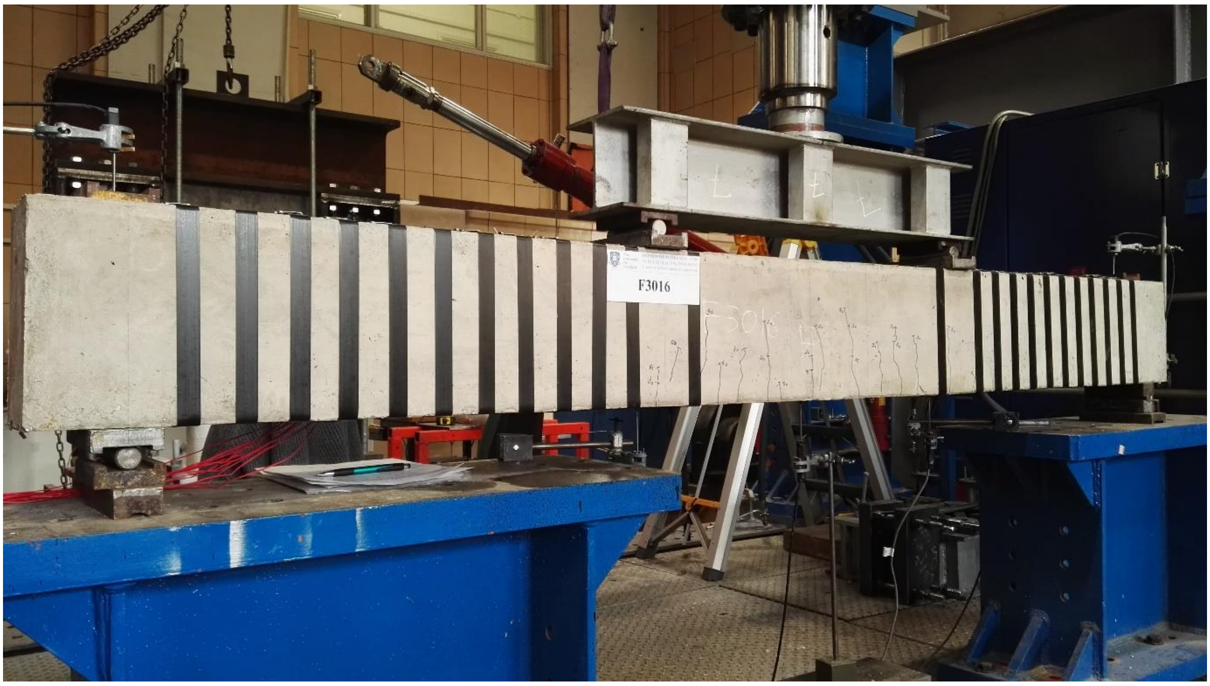

Figure C.5 Testing and metal straps arrangements for all beams reinforced with 16-mm rebars.

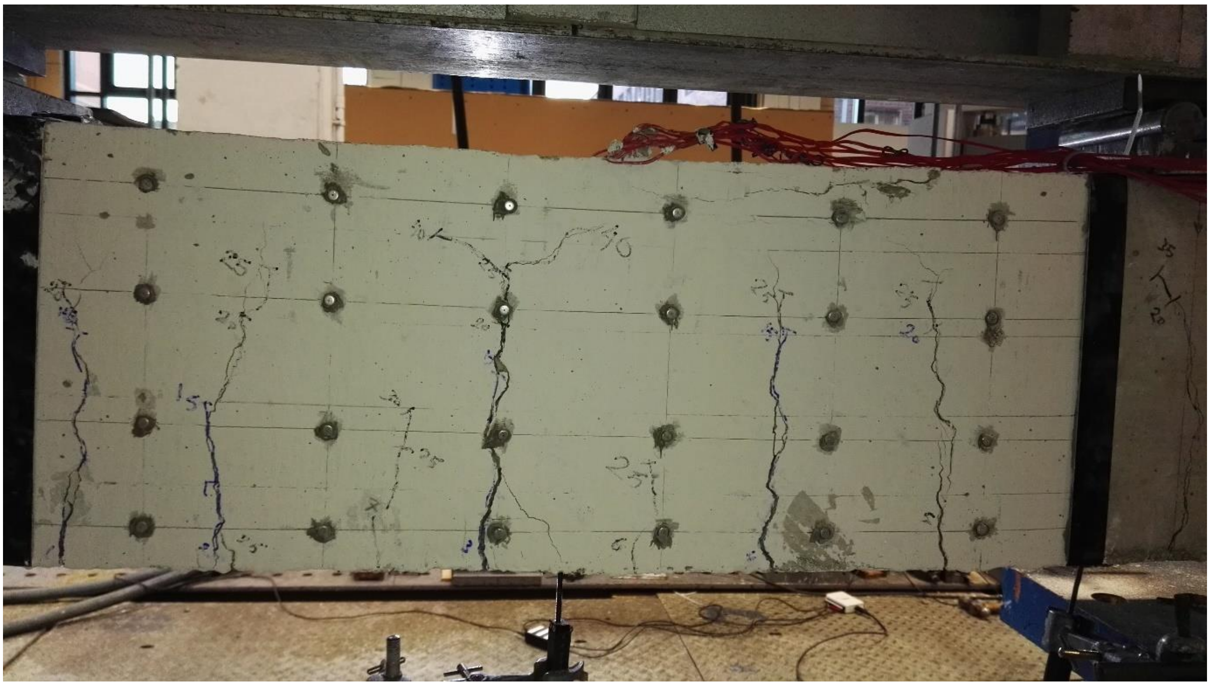

Figure C.6 Final cracking pattern in constant moment zone in beam B0010.

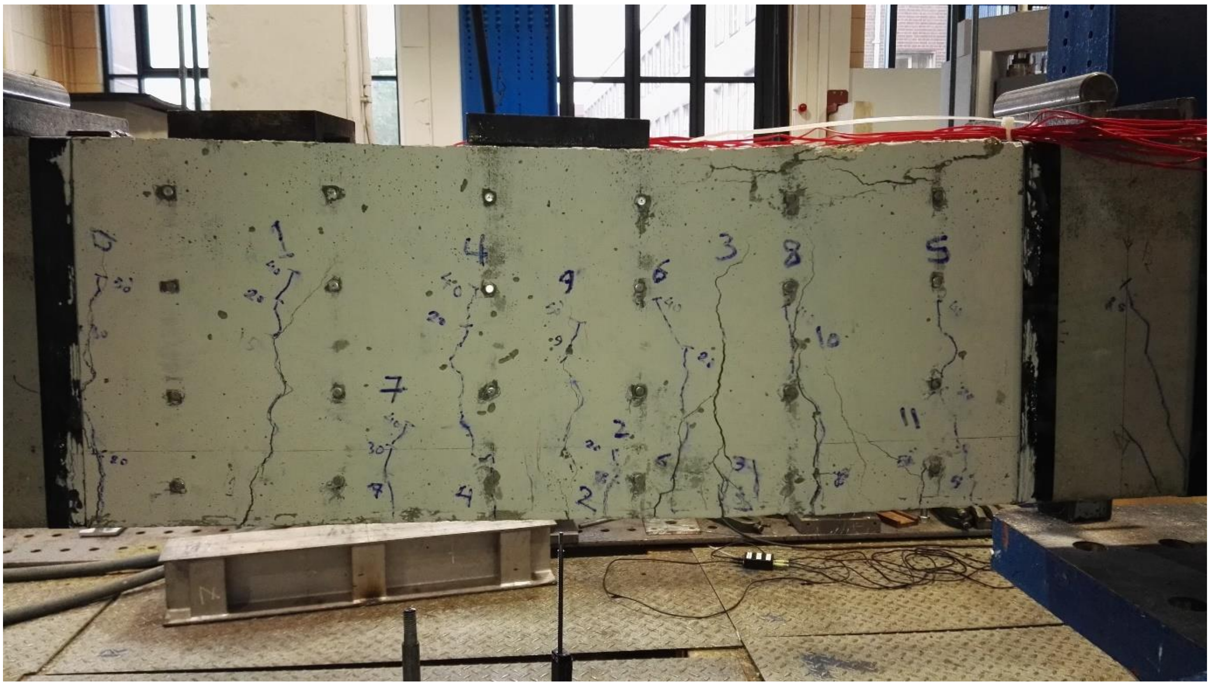

Figure C.7 Final cracking pattern in constant moment zone in beam B0016.

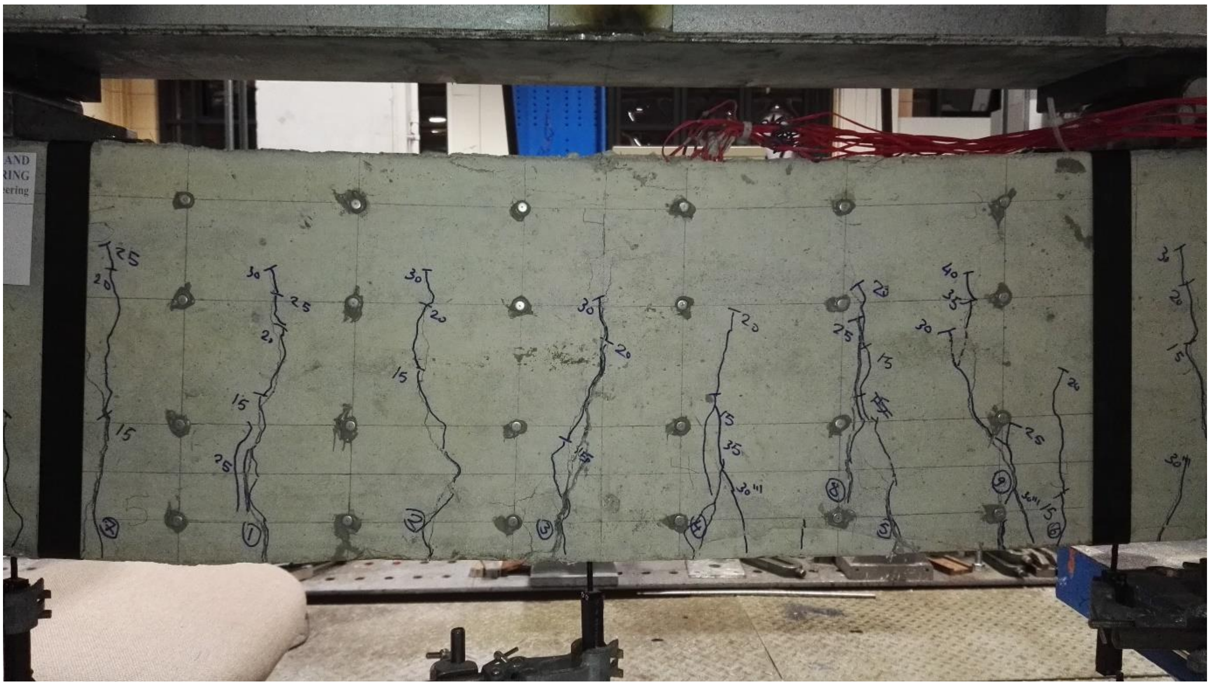

Figure C.8 Final cracking pattern in constant moment zone in beam B2010.

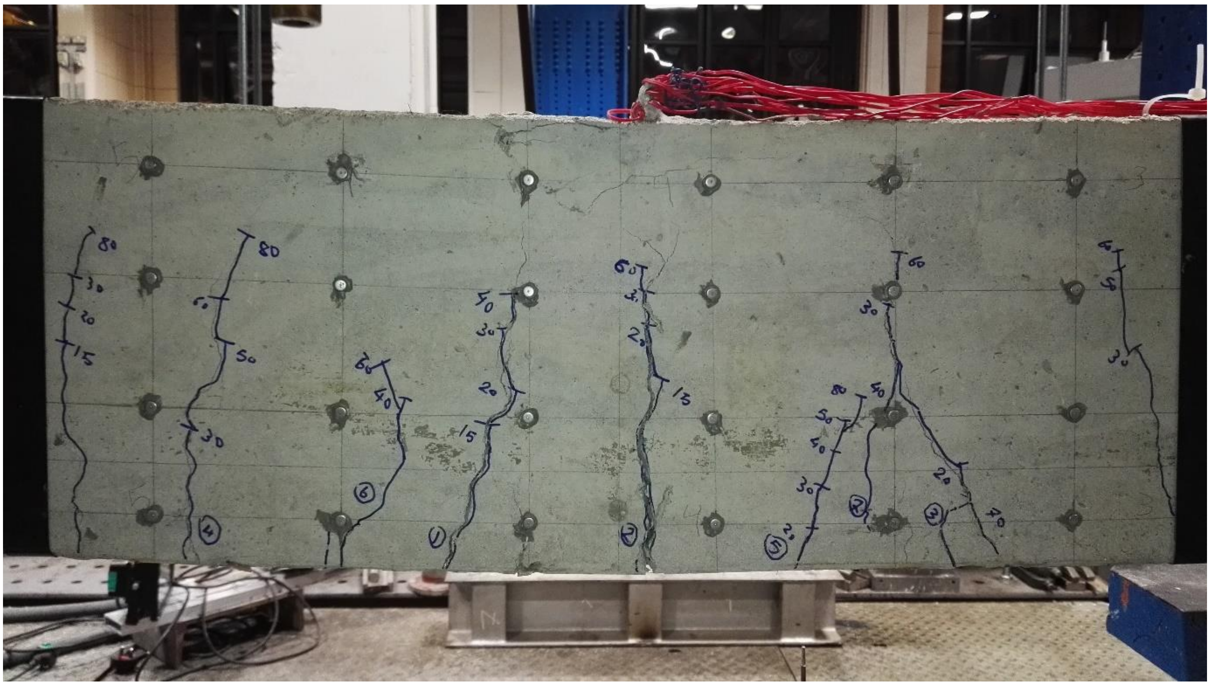

Figure C.9 Final cracking pattern in constant moment zone in beam B2016.

Figure C.10 Final cracking pattern in constant moment zone in beam B3010.

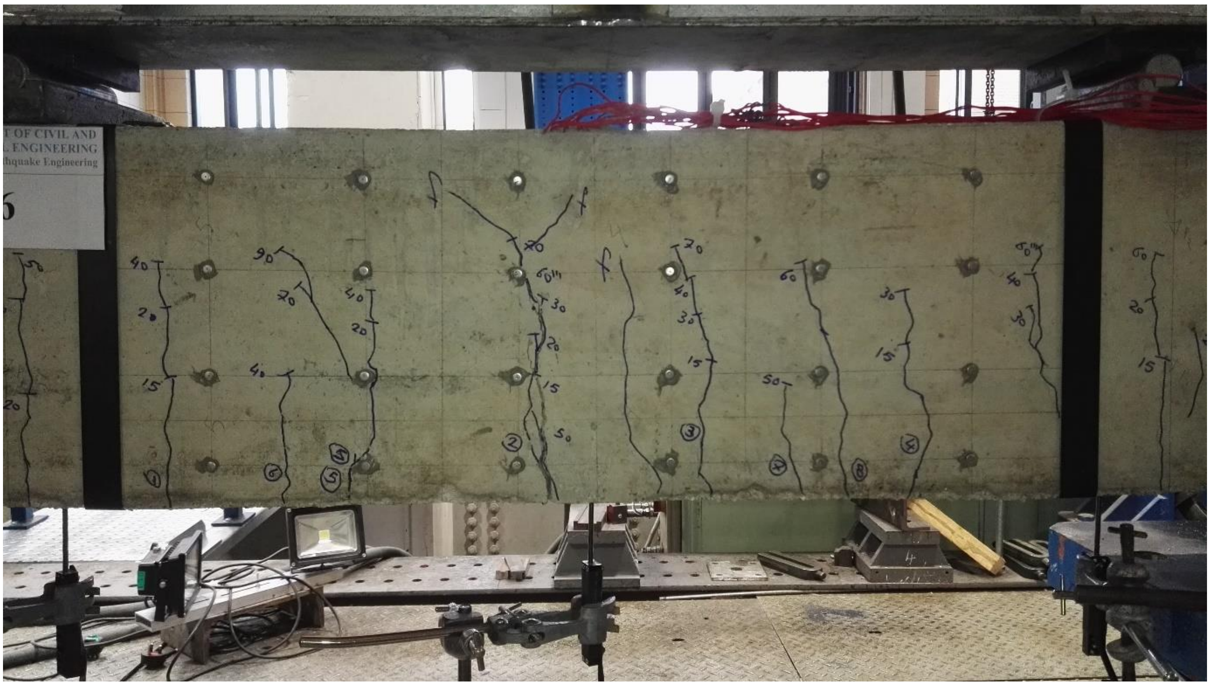

Figure C.11 Final cracking pattern in constant moment zone in beam B3016.

Figure C.12 Final cracking pattern in constant moment zone in beam C3010.

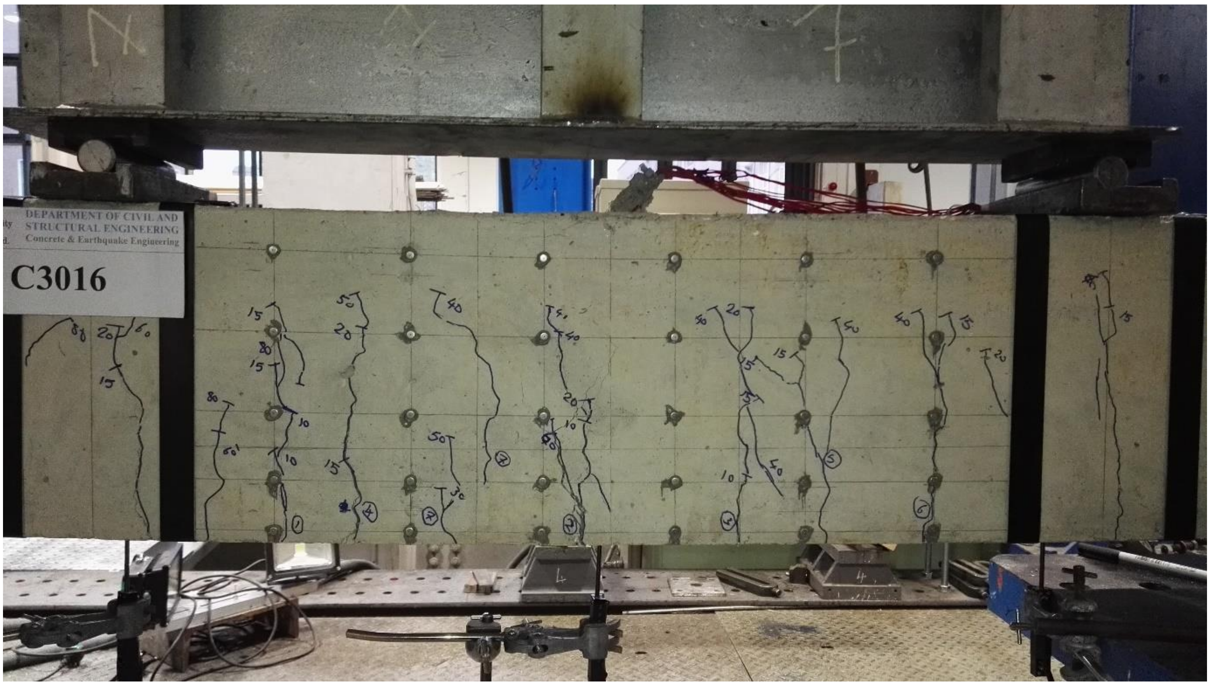

Figure C.13 Final cracking pattern in constant moment zone in beam C3016.

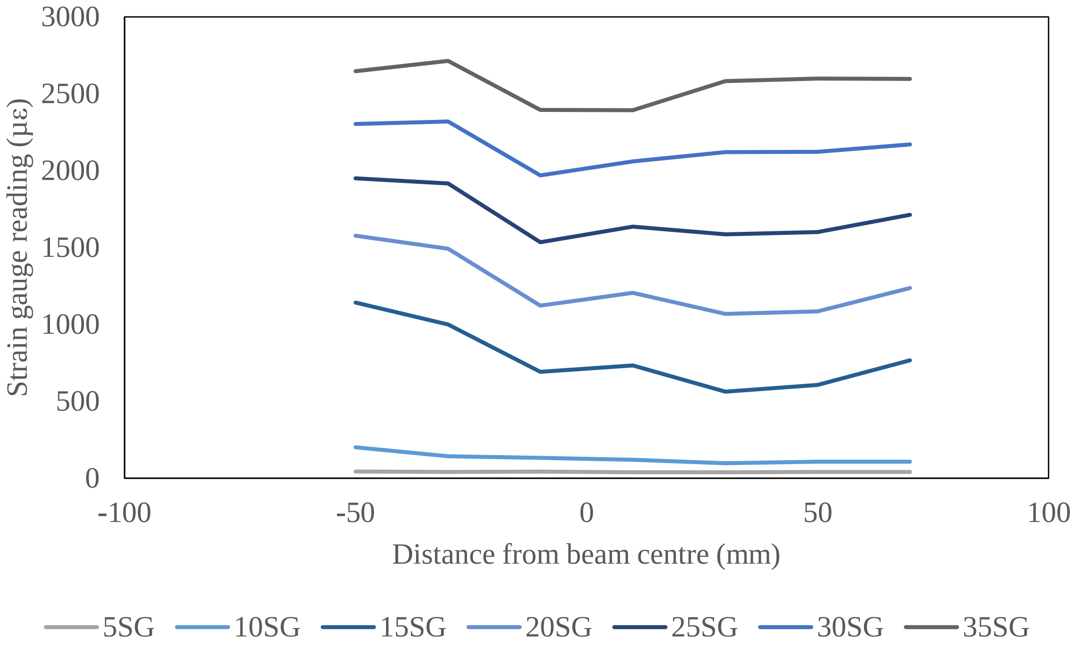

Figure C.14 Strain development profiles as recorded by strain gauges (SG) in beam B0010.

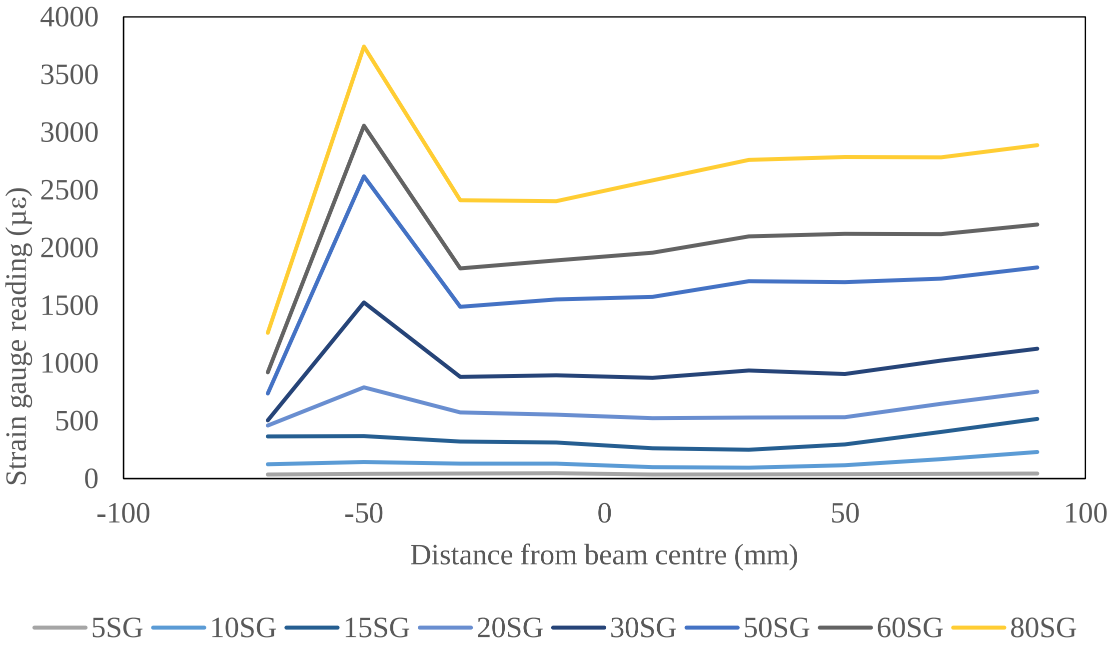

Figure C.15 Strain development profiles as recorded by strain gauges (SG) in beam B0016.

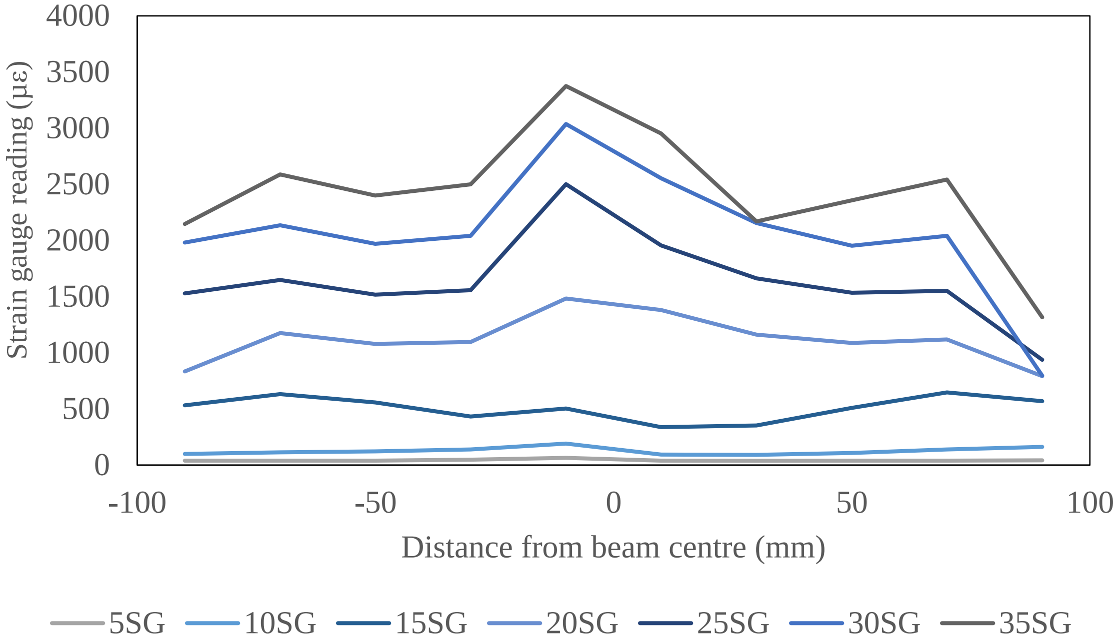

Figure C.16 Strain development profiles as recorded by strain gauges (SG) in beam B2010.

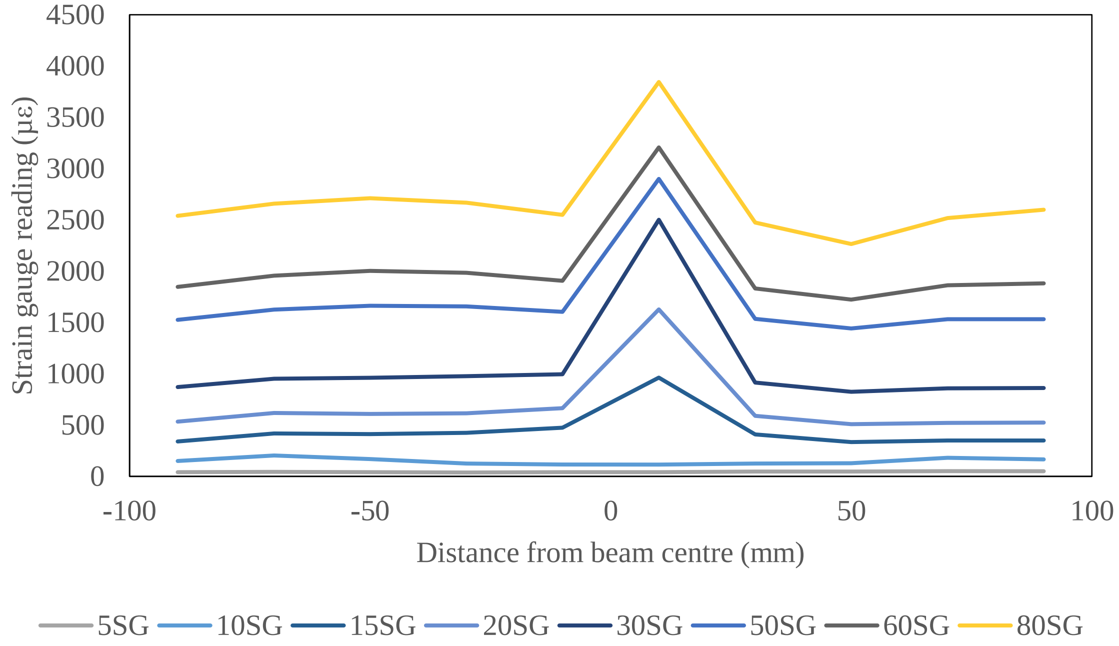

Figure C.17 Strain development profiles as recorded by strain gauges (SG) in beam B2016.

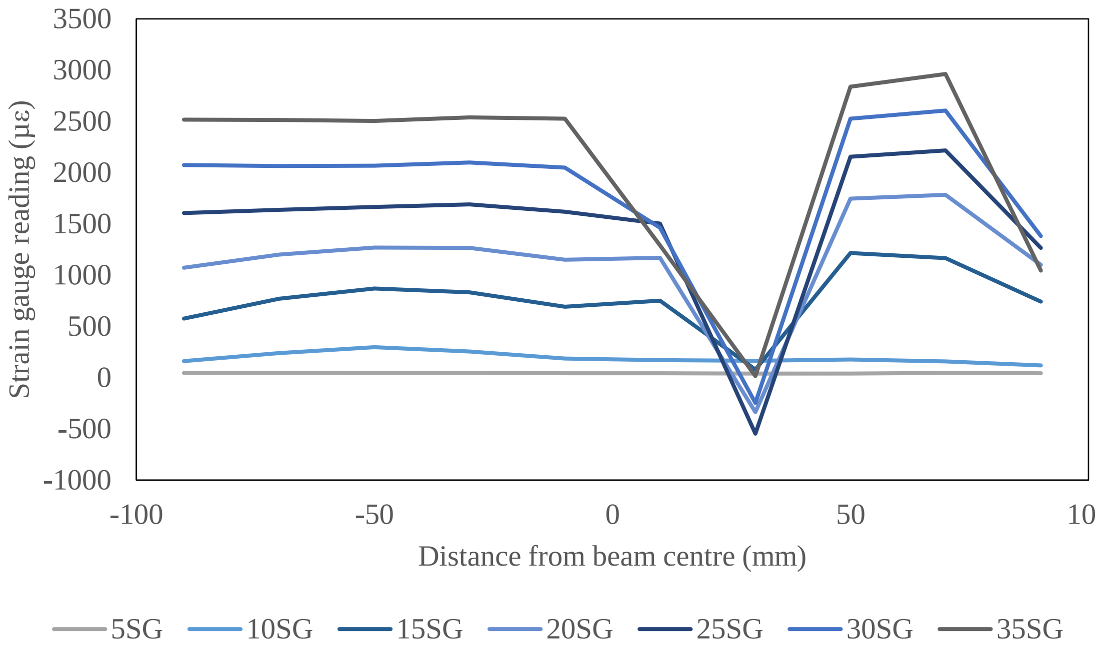

Figure C.18 Strain development profiles as recorded by strain gauges (SG) in beam B3010.

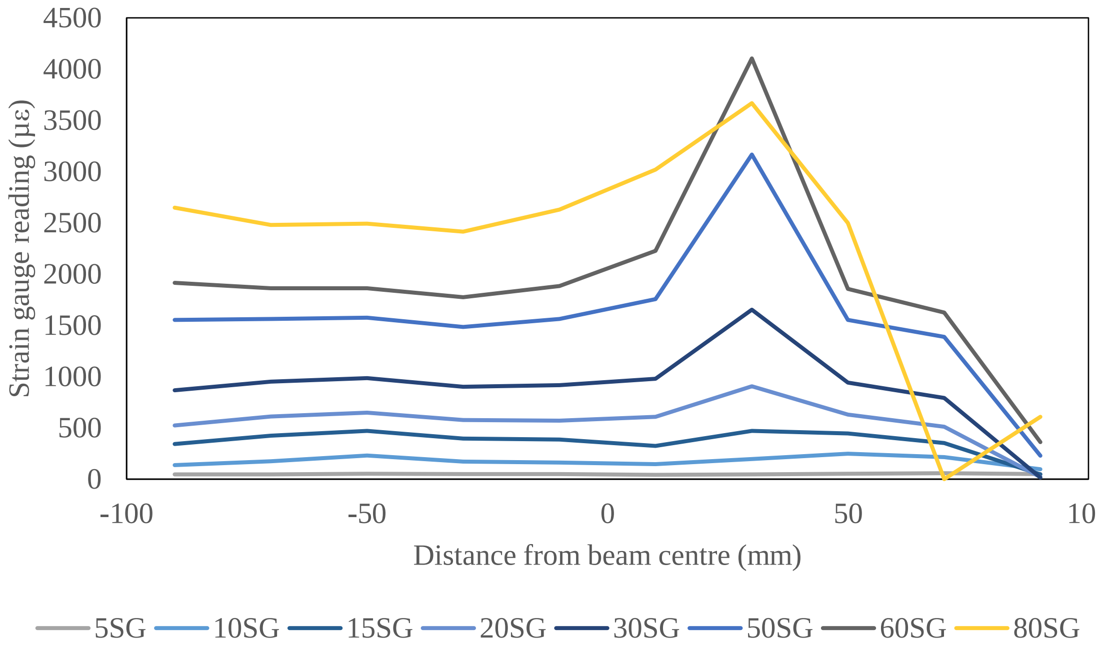

Figure C.19 Strain development profiles as recorded by strain gauges (SG) in beam B3016.

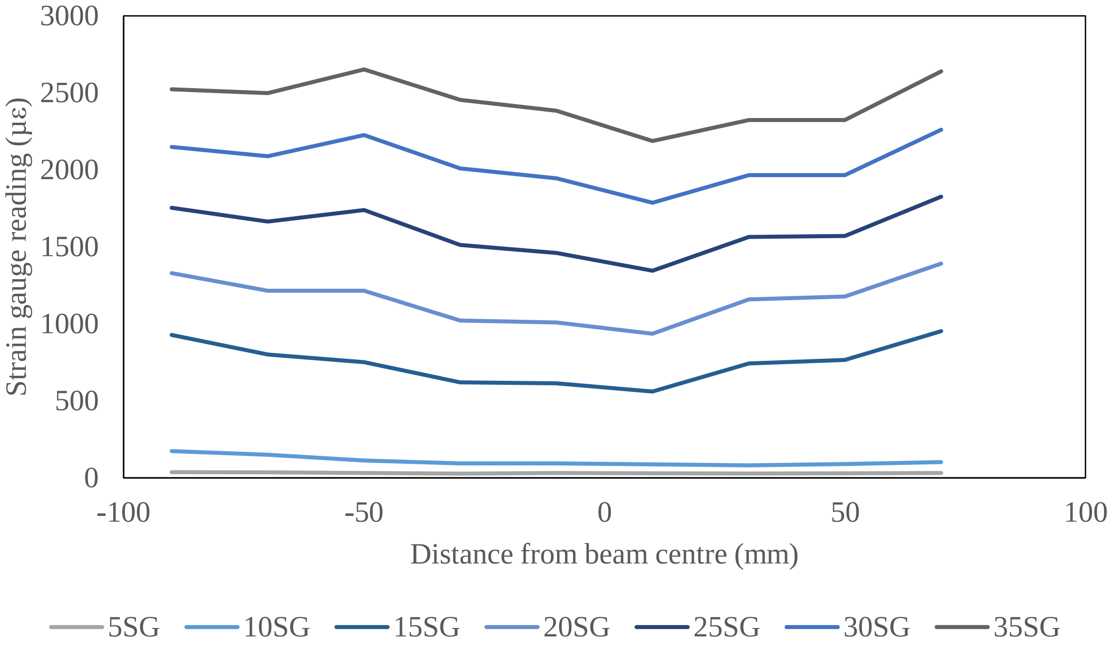

Figure C.20 Strain development profiles as recorded by strain gauges (SG) in beam C3010.

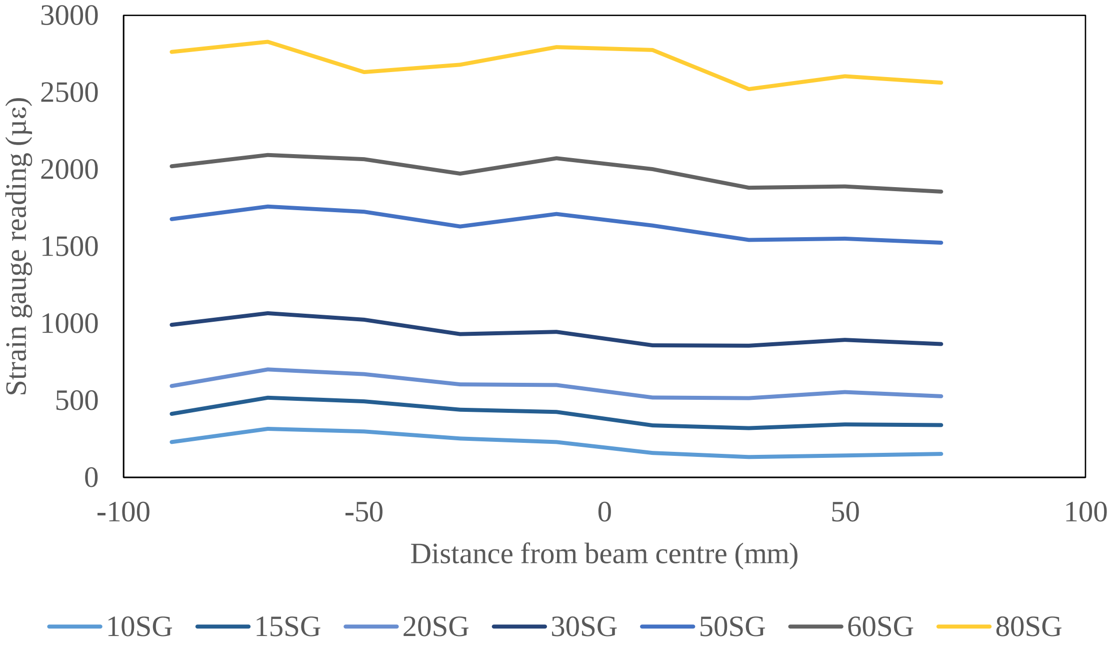

Figure C.21 Strain development profiles as recorded by strain gauges (SG) in beam C3016.

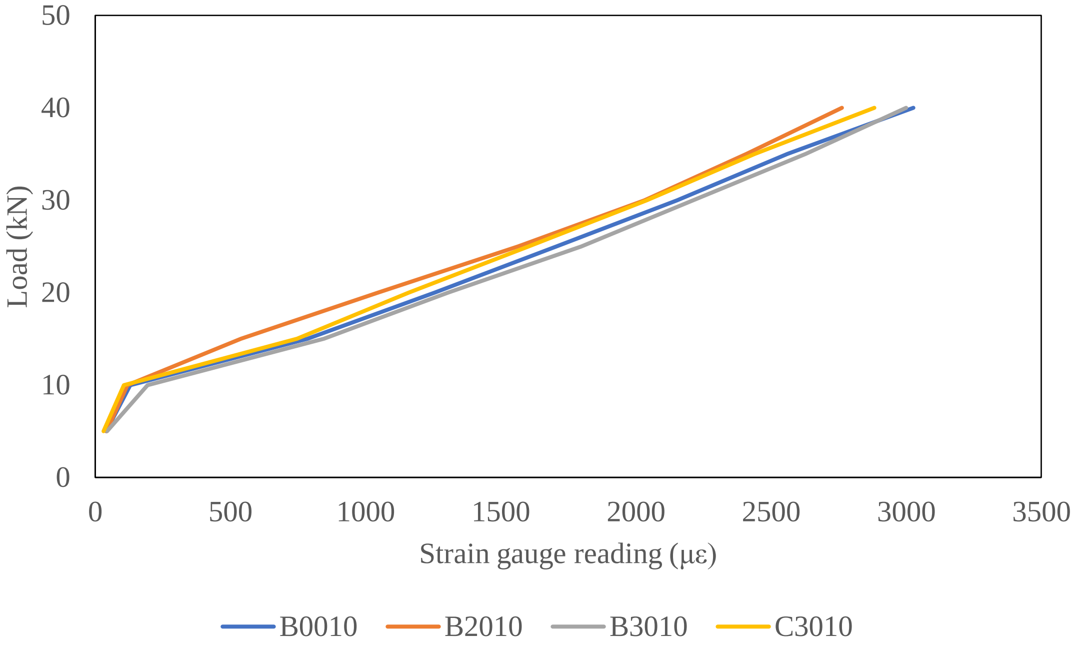

Figure C.22 Average strain gauge readings in beams reinforced with 10-mm rebars.

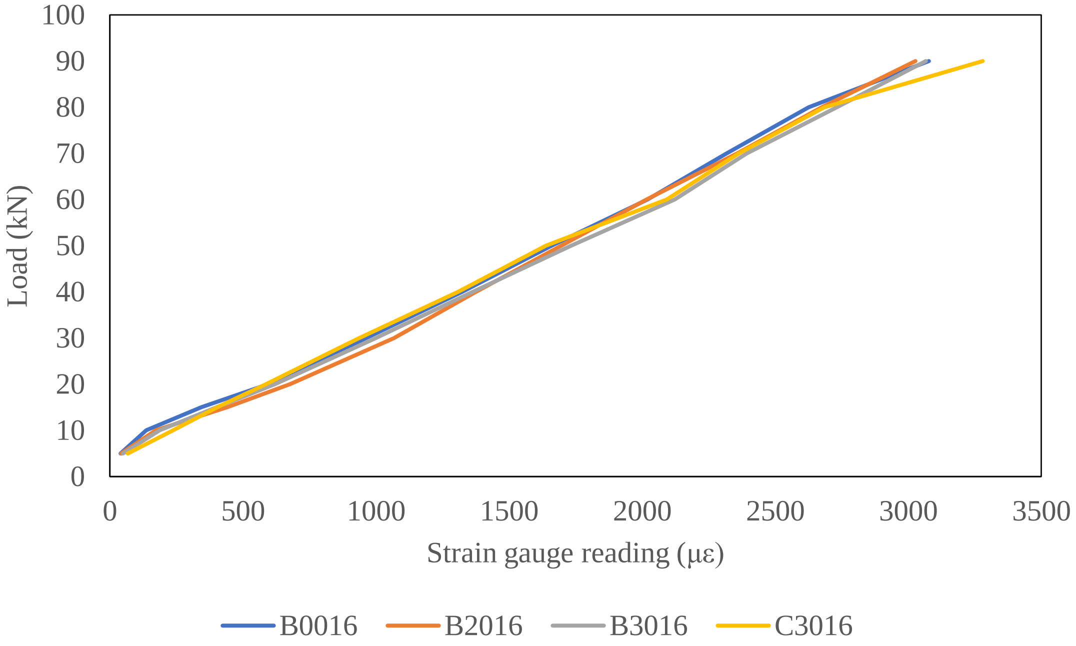

Figure C.23 Average strain gauge readings in beams reinforced with 16-mm rebars.

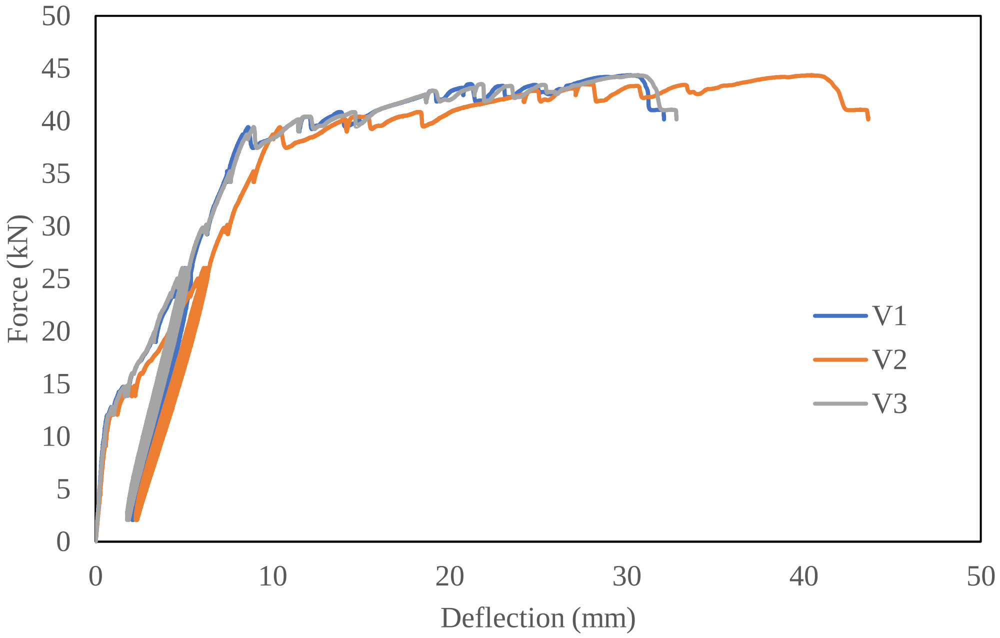

Figure C.24 Deflection at mid span (V2) and under loading points (V1 & V3) in beam B0010.

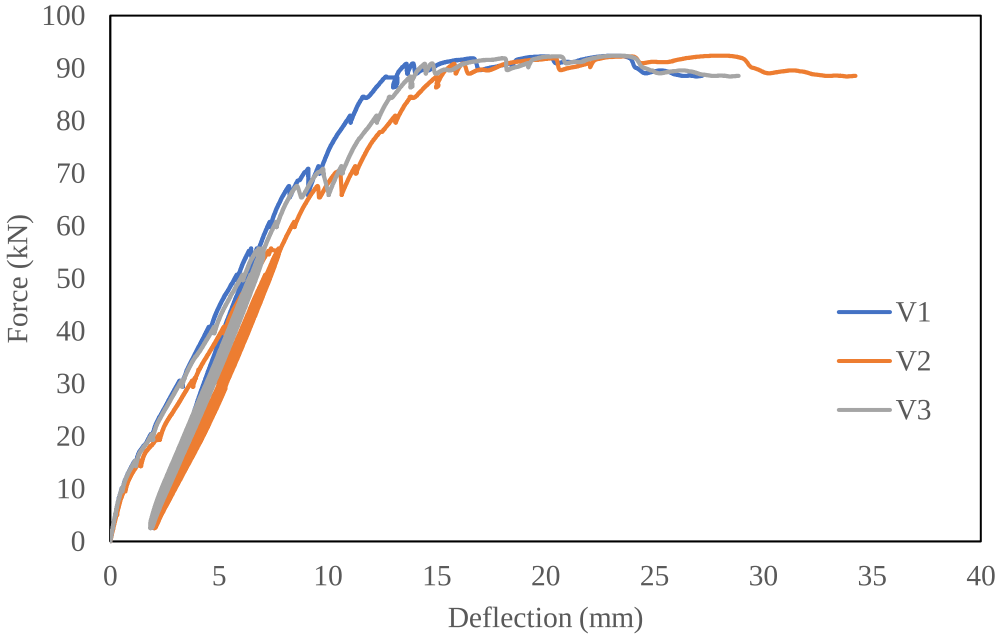

Figure C.25 Deflection at mid span (V2) and under loading points (V1 & V3) in beam B0016.

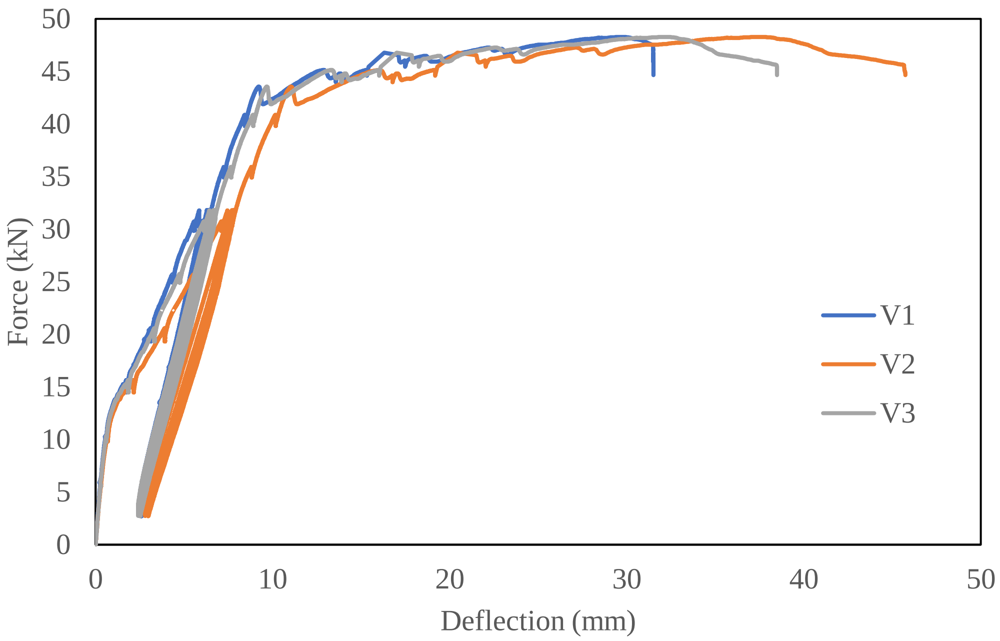

Figure C.26 Deflection at mid span (V2) and under loading points (V1 & V3) in beam B2010.

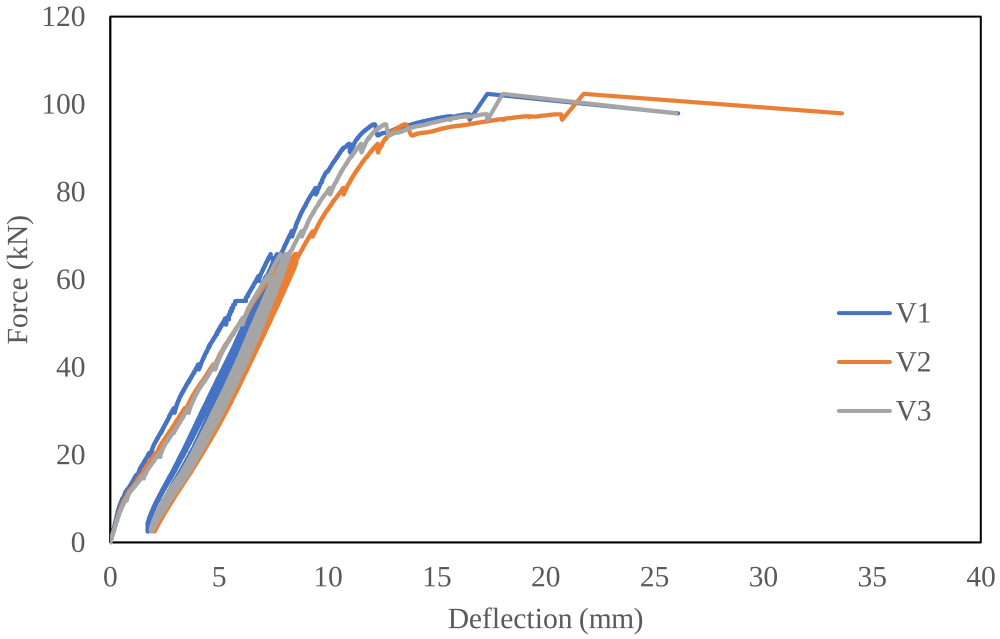

Figure C.27 Deflection at mid span (V2) and under loading points (V1 & V3) in beam B2016.

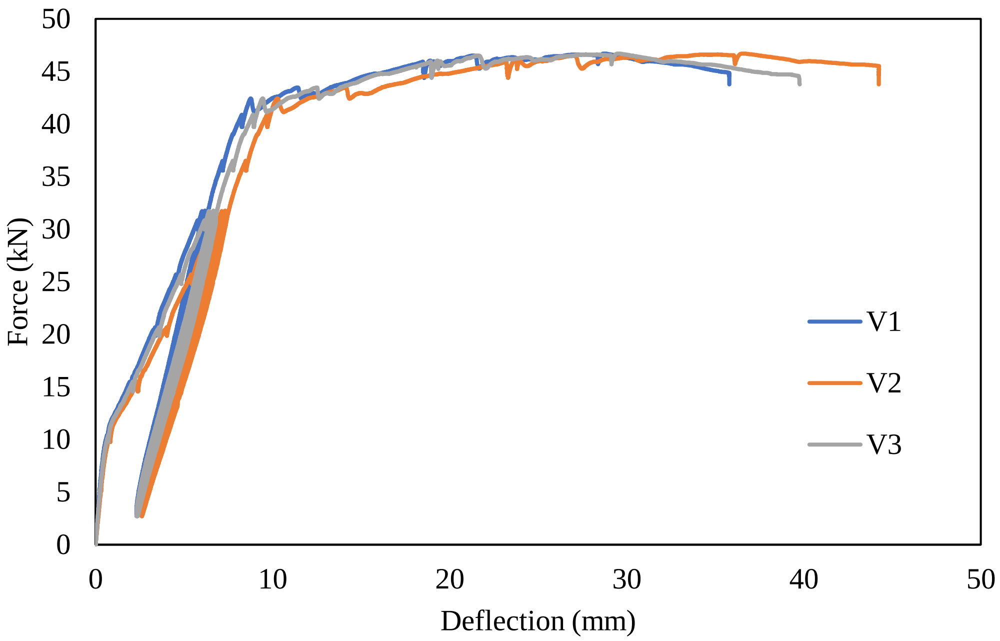

Figure C.28 Deflection at mid span (V2) and under loading points (V1 & V3) in beam B3010.

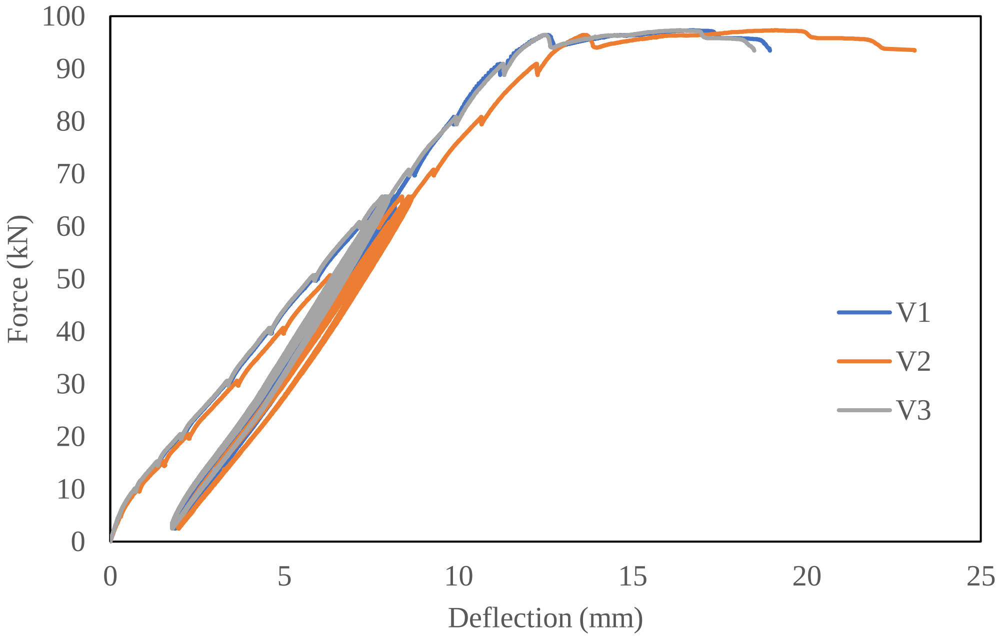

Figure C.29 Deflection at mid span (V2) and under loading points (V1 & V3) in beam B3016.

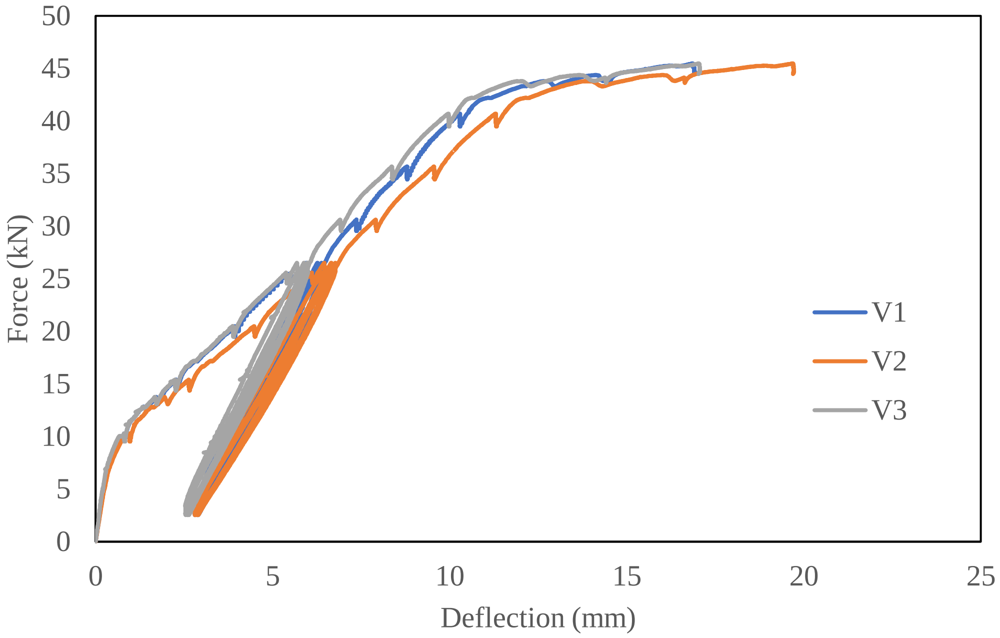

Figure C.30 Deflection at mid span (V2) and under loading points (V1 & V3) in beam C3010.

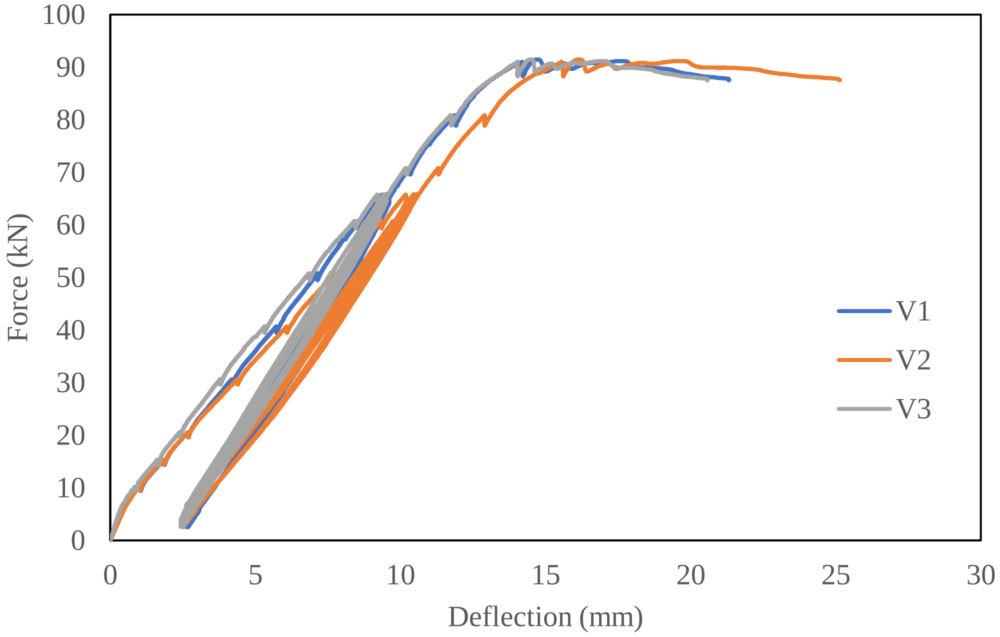

Figure C.31 Deflection at mid span (V2) and under loading points (V1 & V3) in beam C3016.